İZMİR KÂTİP ÇELEBİ ÜNİVERSİTESİ
2010
GRADUATE SCHOOL OF NATURAL AND APPLIED SCIENCES

Simulation of Three-Dimensional Slender Droplet Motion with Adaptive Mesh Refinement

Submitted to the Graduate School of Natural and Applied Sciences in partial fulfillment of the requirements for the degree of

Master of Science

in Mechanical Engineering

by

Mert ÖZDOĞAN

ORCID 0000-0001-8229-0563

July, 2022

This is to certify that we have read the thesis **Simulation of Three-Dimensional Slender Droplet Motion with Adaptive Mesh Refinement** submitted by **Mert Özdoğan**, and it has been judged to be successful, in scope and in quality, at the defense exam and accepted by our jury as a MASTER'S THESIS.

APPROVED BY:

Advisor: **Asst. Prof. Dr. Umut Ceyhan** ……..
İzmir Kâtip Çelebi University

Committee Members:

Assoc. Prof. Dr. Utku Şentürk ……..
Ege University

Assoc. Prof. Dr. Mehmet Akif Ezan ……..
Dokuz Eylül University

Date of Defense: July 26, 2022

Declaration of Authorship

I, **Mert Özdoğan**, declare that this thesis titled **Simulation of Three-Dimensional Slender Droplet Motion with Adaptive Mesh Refinement** and the work presented in it are my own. I confirm that:

- This work was done wholly or mainly while in candidature for the Master's degree at this university.
- Where any part of this thesis has previously been submitted for a degree or any other qualification at this university or any other institution, this has been clearly stated.
- Where I have consulted the published work of others, this is always clearly attributed.
- Where I have quoted from the work of others, the source is always given. This thesis is entirely my own work, with the exception of such quotations.
- I have acknowledged all major sources of assistance.
- Where the thesis is based on work done by myself jointly with others, I have made clear exactly what was done by others and what I have contributed myself.

Signature:

_____

Date: 26.07.2022

_____

Simulation of Three-Dimensional Slender Droplet Motion with Adaptive Mesh Refinement

Abstract

While droplet moves over surfaces, various structures are observed; cusp and corner formation, pearling, pinning/depinning, to name a few. We develop a finite element method (FEM) based solver to analyze three-dimensional motion of slender droplets over several substrates. To get accurate results within a feasible computation time, an adaptive mesh refinement (AMR) based on non-conformal, balanced and preload quadtree mesh structure is embedded within our quadratic FEM solver to focus our computational power on specific regions like contact lines. We validate our solver with the power-law of Tanner and Cox-Voinov law which is the linear relation between cube of dynamic contact angle and capillary number (*Ca*). We analyze various problems including flat substrates where complex formations such as cusps, pearls and rivulets are observed depending on the dimensionless bond number (*Bo*), which is the measure of prepotency between gravitational and surface tension forces. Addition of roughness to surface can expedite such droplet formations. To investigate that we place a droplet on chemically homogeneous inclined substrate with a sinusoidal cell, and we observed trapped residual droplets at the receding contact line for a various topography configuration and Bond number. We conclude that either entrapment frequency or the volume of residual droplet is decreasing for small Bond numbers and middling slope topographies. We observe that steep and frequent cells are required to trap and pin a droplet to surface even for high Bond numbers.

Keywords: Adaptive Mesh Refinement, Lubrication Theory, Interfaces, Finite Element Method, Contact Angle Hysteresis, Wetting

Uyarlanabilir Ağ Yapısı ile Üç Boyutlu İnce Damla Hareketi Simülasyonu

Öz

Damlacıklar bir yüzey üzerinde hareket ederken değişken yapılar gözlenir; çıkıntı, köşe oluşumu, incilenme, tutunma/serbest kalma gibi oluşumlar bunlara örnektir. Üç boyutlu ince damla yapılarının çeşitli yüzeylerde analizini yapmak için sonlu elemanlar metodu (SEM) temelli bir çözücü geliştirildi. Doğru sonuçları makul hesaplama zamanında elde edebilmek için dengelenmiş, yüzeyleri uyumsuz ve ön yüklemeli dördün ağaç veri yapılı uyarlanabilir ağ yapısı, hesaplama gücümüzü temas hattı gibi beliri bölgelerde odaklamak için SEM çözücümüz içerisine gömüldü. Bulunan sonuçlar Tanner ve capillary katsayısı ile dinamik değme açısının kübü arasındaki doğrusallığı belirten Cox-Voinov yasası ile doğrulandı. Çıkıntı, köşe oluşumu ve incilenme gibi karmaşık oluşumların gözlemlendiği düz yüzeyler dahil çeşitli problemler yerçekimsel ve yüzey gerilimi kuvvetlerinin baskınlığını ölçen boyutsuz Bond sayısına (*Bo*) bağlı olarak incelendi. Yüzeye topografya eklenmesi bu tür damla oluşumlarını hızlandırabilir. Bunun incelenmesi için kimyasal olarak homojen eğimli sinusoidal bir yüzeye damlacık yerleştirildi ve çeşitli topografya biçimi ve Bond sayısı için gerileyen temas hattındaki hapsedilmiş kalıntı damlacıklar gözlemlendi. Hapsedilme miktarı ya da kalıntı damlacıkların hacminin küçük Bond sayıları ve kısmen eğimli topografya için azaldığı sonucuna varıldı. Bir damlacığı büyük Bond sayılarında bile yüzeye hapsedip tutunmasını sağlamak için sarp ve sık basamakların olması gerektiği gözlemlendi.

Anahtar Kelimeler: Uyarlanabilir Ağ Yapısı, Yağlama Teorisi, Arayüzey, Sonlu Elemanlar Metodu, Değme Açısı Histerezi, Islanma

To my beloved ones.

Acknowledgment

This thesis is the product of long and compelling study. In this process, I've faced countless challenges that developed me both educationally and personally. But in the end, I've learned numerous invaluable knowledge in several fields. For all of these, I would like to thanks to my advisor Dr. Umut Ceyhan for his teachings and support. Academic year of 2019-2022 has been especially hard due to Covid-19 pandemic. But even in these dire times, I always found a guidance from him. For that I feel privileged to be his student.

I would like to thank my committee members Dr. Utku Şentürk and Dr. Mehmet Akif Ezan for their interests and valuable contributions.

I also would like to thank all of my friends and special person who always encourage and help me throughout this time. Last but not least, I would like to thank to my dear parents for their endless support.

Table of Contents

Declaration of Authorship ... ii

Abstract ... iii

Öz ... iv

Acknowledgment ... vi

List of Figures ... ix

List of Tables ... xii

List of Symbols ... xiii

1 Introduction ... 1

1.1 Wetting ... 1

1.2 Lubrication Approximation ... 4

1.3 Literature Survey ... 9

1.4 Motivation of the Study ... 11

2 Model Problem ... 12

2.1 Unsteady Film-Evolution Equation ... 17

2.2 Non-Dimensional Film-Evolution Equation ... 19

3 Numerical Method ... 22

3.1 Weak Formulation and Shape Functions ... 22

3.1.1 Weak Formulation ... 22

3.1.2 Shape Functions ... 24

3.2 Finite Element Approximations and Time Integrations ... 26

3.3 Mapping of the Derivative Terms ... 30

3.4 Symmetric Boundary Condition ... 31

4 Adaptive Mesh Refinement and Derefinement 35
4.1 Quadtree Data Structures 37
4.1.1 Consecutive Requirement 39
4.1.2 Hanging Points 40
4.2 Element Marking Mechanism 41
4.2.1 Geometrical Marking 41
4.2.2 Pressure Marking 42
4.2.3 Mesh Balancing 43
5 Motion of Droplets Over Homogeneous Substrates: Validation 47
5.1 Mesh Independence 47
5.2 Equilibrium Angle 49
5.2.1 Effect of Precursor Film Thickness 49
5.2.2 Effect of Equilibrium Angle 52
5.3 Tanner's Law 54
5.4 Droplet Sliding Over Inclined Flat Substrates 55
5.4.1 Cox-Voinov Law 59
6 Effect of Surface Topography on Pearling 61
6.1 Factors that Effect Droplet Deposition 62
6.2 Trapping Droplets on Sinusoidal Substrates 70
7 Conclusion 75
References 77
Appendices 86
Appendix A Non-Dimensional Film Evolution Equation 87
Appendix B Weak Formulation of Droplet Thickness 89
Curriculum Vitae 92

List of Figures

Figure 1.1 (a) Unwetted case: surface energy of solid vapor (γ_{SV}), (b) Wetted case: surface energies of liquid-vapor (γ_{LV}) and solid-liquid (γ_{SL}) 2

Figure 1.2 (a) Perfect wetting, $\theta = 0°$, (b) Partial wetting, $0° < \theta < 90°$, hydrophilic surface, (c) Partial wetting $\theta > 90°$, hydrophobic surface.... 2

Figure 1.3 Balance between the tangential components of surface forces at the contact line 3

Figure 1.4 Droplet sliding over a tilted flat substrate 4

Figure 1.5 Presentation of precursor film thickness (f_0) on solid substrate 9

Figure 2.1 Problem domain, droplet sliding on a substrate with sinusoidal topography..... 12

Figure 2.2 Hydrostatic force balance at the liquid-vapor interface 15

Figure 2.3 Droplet is represented as a spherical cap with an equilibrium angle of θ_e 19

Figure 3.1 Nine variable number nodes of two-dimensional element [59] 25

Figure 3.2 (●): Neumann boundary condition, (■): Dirichlet boundary condition, (a) Domain we use to solve spreading of a quarter droplet, (b) Domain we use to solve sliding problems where the north axis is the symmetry line 34

Figure 4.1 (a) Conformal mesh: all edges and vertices are connected; continuity is achieved in the domain. (b) Non-conformal mesh: there are non-intersecting edges at the level difference, discontinuous system..... 36

Figure 4.2 Conventional quadtree structure that relates parent and its children 37

Figure 4.3 Prequad data structure. All data are constructed in advance..... 38

Figure 4.4 Same example with Figure 4.1 but with a quadtree data structure 38

Figure 4.5 (a) Conventional data structure from Figure 4.2. Here nodes are in serial like their element number. (b) Prequad data structure from Figure 4.4. ROOT nodes are same but newly generated nodes are ordered in counterclockwise. Notice that nodes are defined such way that they are all unique..... 39

Figure 4.6 (a) Hanging points of linear elements, (b) Hanging points of quadratic elements at the non-intersecting edges..... 40

Figure 4.7 Geometrical marking of the contact line. $(--)$: Upper limit (η), $(-)$: Lower limit: in this case, it is ellipse equation 42
Figure 4.8 Contact line is marked with our disjoining pressure model. Upper and lower limits are decided by the pressure model. So, there is no need to specify additional parameter in this method 43
Figure 4.9 Balanced mesh: level difference is maximum one after the refinement . 43
Figure 4.10 Unbalanced mesh structure: finest level is neighboring (level 4) the level 2 which means there exist 2 level difference. This is an undesired mesh structure 44
Figure 4.11 Proper mesh structure: balanced and smooth transition 45
Figure 4.12 Comparison of level3 and level4 refinement for same resolution 46
Figure 5.1 Location of contact lines where $L_x = 20$ and $L_y = 1.2$ for time $t = 7.0$. Dark blue: $50x3$, Yellow: $100x6$, Red: $125x8$, Green: $150x9$ 48
Figure 5.2 Computed equilibrium angle for decreasing precursor film thickness. As we decrease the f_0, we approach equilibrium angle 51
Figure 5.3 Location of transition from precursor film thickness to droplet thickness for 3 different f_0 along *x*-axis at the symmetry line 52
Figure 5.4 Change of central droplet height (f_{max}) with respect to time *t* 55
Figure 5.5 Change of capillary number for different inclination angels. $(-*)$: Kumar [54] for $\theta_e = 45°$ and $f_0 = 0.005$, $(-\blacksquare)$: Ahmed [61] for $\theta_e = 45°$ and $f_0 = 0.01$, $(--o)$: Our results for $\theta_e = 45°$ and $f_0 = 0.01$, $(-o)$: Our results for $\theta_e = 45°$ and $f_0 = 0.0025$, $(-\diamond)$: Experimental data of Podgorski [49] 56
Figure 5.6 Aerial view of sliding droplets with different tilt angles. (a) Tilt angle is so small that droplet takes circular shape, (b) First critical tilt angle is passed, droplet begins forming a corner. Change in the mass center of droplet can be seen from yellow contour 57
Figure 5.7 Aerial view of sliding droplet with pearls behind 58
Figure 5.8 $(-o)$: Ca vs θ_A^3 , $(-\diamond)$: Ca vs θ_R^3 from Cox-Voinov 59
Figure 6.1 Residual droplet deposition for (a) Å $= 0.05$, (b) Å $= 0.075$, (c) Å $= 0.1$ 62
Figure 6.2 Curvature formation at the receding contact line for Å $= 0.1$ at times: (a) 4.55, (b) 4.76, (c) 4.98, (d) 5.29 64

Figure 6.3 Propagation of lateral contact line from *x-y* plane for $(- \cdot -)$: $\text{Å} = 0.1$, $(-)$: $\text{Å} = 0.075$, $(- -)$: $\text{Å} = 0.05$, $(\cdots)$: Single sinusoidal cell 65

Figure 6.4 Aerial view (*x-y* plane) of curvature formation for $(- \cdot -)$: $\text{Å} = 0.1$, $(-)$: $\text{Å} = 0.075$, $(- -)$: $\text{Å} = 0.05$. $(\cdots)$: Single sinusoidal cell 66

Figure 6.5 Droplet sliding over double sinusoidal cell with $\text{Å} = 0.05$ and $\lambda = 0.75$ 67

Figure 6.6 Droplet sliding over triple sinusoidal cell with $\text{Å} = 0.05$ and $\lambda = 0.75$ 68

Figure 6.7 Aerial view of curvature formation for triple sinusoidal function with $\text{Å} = 0.05$ and $\lambda = 0.75$ 69

Figure 6.8 Entrapment of droplets for (a): $\text{Å} = 0.025$, (b): $\text{Å} = 0.05$, (c): $\text{Å} = 0.075$ for same frequency $\lambda = 0.75$ 71

Figure 6.9 Detailed view of $\text{Å} = 0.075$ and $\lambda = 0.75$ domain in figure 6.8(c) 72

Figure 6.10 *x-z* plane view of sliding droplet over sinusoidal cell with same amplitude, $\text{Å} = 0.075$, as in Figure 6.8(c) but with higher frequency $\lambda = 0.125$.... 73

Figure 6.11 Entrapment of droplets for (a): $\text{Å} = 0.025$, (b): $\text{Å} = 0.05$, (c): $\text{Å} = 0.075$ for same frequency $\lambda = 0.75$, (d): $\text{Å} = 0.05$ and $\lambda = 1.25$ 73

List of Tables

Table 3.1 Quadratic interpolation functions according to Figure 3.1 25

Table 4.1 Number of total nodes to analyze same problem for equal resolution. Length on the *y*-axis is constant and same for all cases, $L_y = 1.2$ 45

Table 5.1 Change of the equilibrium angle with total number of elements N at ROOT 48

Table 5.2 Equilibrium angles for decreasing precursor film thickness 50

Table 5.3 Relative errors between measured and expected equilibrium angles for various film thicknesses 53

Table 5.4 Thin flow assumption for different equilibrium angles 53

Table 6.1 Residual droplet volumes for various amplitudes 65

Table 6.2 Total volume of trapped droplets 71

Table 6.3 Trapped droplet volumes at each cell for various Å 72

Table 6.4 Trapped volumes comparison between lower slope high frequency and high slope low frequency cells 74

List of Symbols

α	Inclination angle
Å	Amplitude of sinusoidal wave
γ	Surface tension
Γ	Dirichlet boundary
δ	Kronecker delta
Δ	Difference
∇	Gradient
ε	Thin-flow scale
η	Upper marking limit
μ	Dynamic viscosity of droplet
θ	Contact angle
θ_e	Equilibrium contact angle
θ_m	Mesoscopic contact angle
ρ	Fluid density
λ	Wavelength of sinus wave
ζ	Film surface
Π	Disjoining pressure
τ	Time step size
φ	Shape function
Ω	Fluid domain
ℓ_0	Length scale
ℓ_{micro}	Microscopic length scale

$H_1(\Omega)$.	Hilbert-Sobolov space
a	Time step constant from Taylor Expansion
b	Time step constant from Taylor Expansion
Bo	Bond number
C_1	First unknown integration constant
C_2	Second unknown integration constant
C_3	Third unknown integration constant
c	Time step constant from Taylor Expansion
Ca	Capillary number
d_x	Grid size on *x*-axis
d_y	Grid size on *y*-axis
f	Droplet thickness
$\overline{f}$	Corresponding test function of droplet thickness
f_0	Precursor film thickness
$\underline{g}$	Gravitational force vector
$h(x,y)$	Topography function
h_0	Height scale
H	Hamakar constant
$\boldsymbol{J}$	Jacobian operator
$\underline{\underline{\boldsymbol{K}}}$	Stiffness matrix
L	Length of the droplet
m	Degree of liquid-solid attraction
$maxx$	Contact line location at east
$maxy$	Contact line location at north
$minx$	Contact line location at west
$miny$	Contact line location at south

n	Degree of liquid-solid repulsion
$\underline{\boldsymbol{n}}$	Normal vector at liquid-gas interface
N	Number of elements
$\overline{p}$	Corresponding test function of pressure
p	Pressure
p^G	Gas pressure at liquid-vapor interface
p^L	Liquid pressure at liquid-vapor interface
p^s	Pressure scale
q	Volumetric flow rat
r	Natural coordinate corresponds to *x*-axis
$\underline{r}$	Residual vector
R	Radius of spherical cap
$\underline{R}$	Right hand side vector
Re	Reynolds number
s	Natural coordinate corresponds to *y*-axis
S	Spreading parameter
t	Time
$\underline{\underline{T}}$	Tangent stiffness matrix
u	Velocity
$\mathcal{V}$	Volume of the droplet
x_0	Droplet center on *x*-axis
y_0	Droplet center on *y*-axis

Subscripts

A	Advancing
max	Maximum

q	Quadratic
r	Residual
R	Receding
s	Scale
t	Trapped
x	Direction on *x*-axis
y	Direction on *y*-axis
z	Direction on *z*-axis

Subscripts

$*$	Dimensional parameter

Chapter 1

Introduction

Droplet motion is a phenomenon that occurs everywhere and even affects us in numerous ways. Sometimes it brings joy or tranquility to a person just by sliding over a window on a rainy day and sometimes it is the only survival chance of an insect at extreme climates like deserts [1-2]. It is over a century old field of study that is still being investigated. To understand the necessity of this study field, let's examine a simple example. Capability of a raindrop to slide over a glass window is an indicator of clean or contaminated surface. If the drop slides with difficulty and leaves many different regimes on glass surface, this means that the surface is contaminated. Otherwise, droplet slides rather with ease. Investigating such features allows us to understand self-cleaning properties and this can be utilized for designing surfaces where cleanliness is important such as solar panels and car windshields [3-4]. Similar benefits can be achieved for industrial applications like printing of electronics [5-6] and heat exchangers [7-8] as well. Droplet motion in the nature can be imitated to design water harvesting systems [1-2], anti-fogging [9] and anti-icing [10] properties. So, there are many ways to utilize from this field of study.

1.1 Wetting

Wetting is the study of how well a liquid covers a solid surface and research on origins of wetting goes back to early 18^{th} century. Wetting is examined in capillarity tubes and thus even today it is often referred to capillarity [11]. For the first time to our knowledge, Hauksbee [12] observes the wetting phenomenon on a capillary tube. He notes that the fluid height and tube diameter have an inverse proportion and vacuum does not influence liquid rise. Similar research is conducted with capillary tubes to

explore this subject [11]. But what really is wetting? To answer that we assume solid (S), liquid (L) and vapor (V) as well-defined surface energy (γ) independent of the existence of other interfaces and solid surfaces are assumed to be atomically smooth and chemically homogeneous (see Figure 1.1).

Figure 1.1: (a) Unwetted case: surface energy of solid vapor (γ_{SV}), (b) Wetted case: surface energies of liquid-vapor (γ_{LV}) and solid-liquid (γ_{SL})

The difference of energies of unwetted and wetted cases are defined as the spreading parameter denoted as S and given as

$$S = \gamma_{SV} - (\gamma_{SL} + \gamma_{LV}). \tag{1.1}$$

For negligible gravity, the state of minimum energy is spherical cap meeting the solid boundary at a defined angle and this angle known as contact angle denoted with θ. This contact angle is the measure of wetting of a fluid. If $S > 0$, wetting is complete and reduces the energy of the system. However, if $S < 0$, then wetting is referred to as partial (see Figure 1.2).

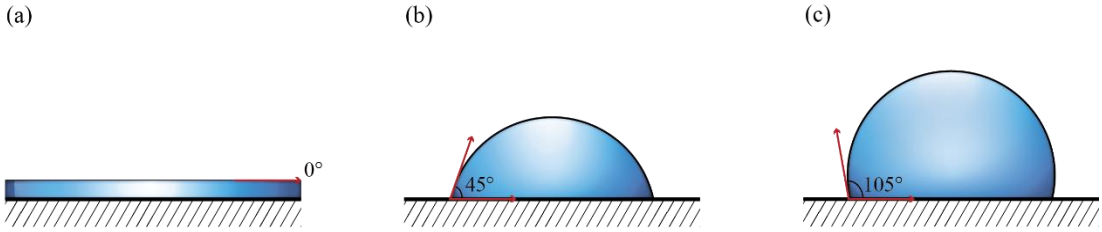

Figure 1.2: (a) Perfect wetting, $\theta = 0°$, (b) Partial wetting, $0° < \theta < 90°$, hydrophilic surface, (c) Partial wetting $\theta > 90°$, hydrophobic surface

At the beginning of the 19th century, study conducted by Young [13] on work of adhesion relates the contact angle and surface energies at the solid-liquid-gas interface or simply contact line (see Figure 1.3).

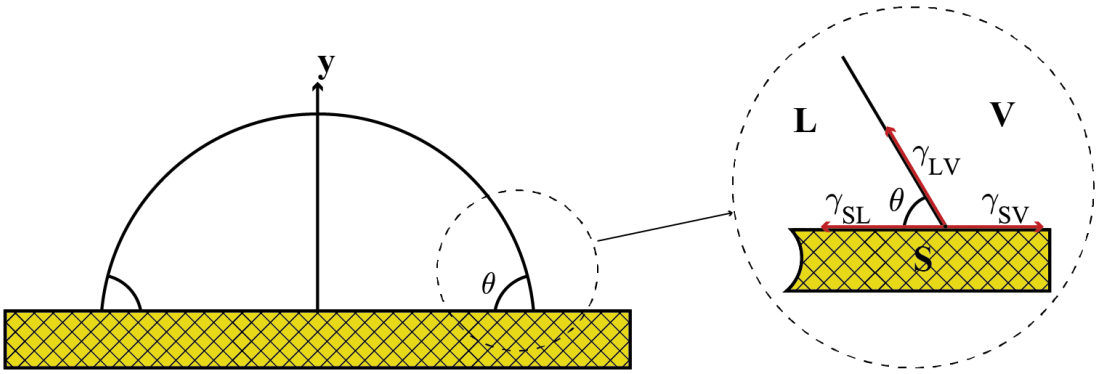

Figure 1.3: Balance between the tangential components of surface forces at the contact line

He determines this angle from tangential force balance at the contact line which is known as Young condition and given by

$$\cos\theta = \frac{\gamma_{SV} - \gamma_{SL}}{\gamma_{LV}}. \tag{1.2}$$

Angle in equation (1.2) is also known as static or equilibrium contact angle where droplet is at its equilibrium. Young defines this angle for ideal substrates (atomically smooth and chemically homogeneous). However, real world surfaces are exposed to chemical contamination and roughness. In such surfaces, droplet over a tilted substrate is pulled by the gravitational forces while surface tension forces restrain it. The force balance between these factors distorts the droplet into an asymmetric shape. Therefore, we cannot mention a unique contact angle anymore. Front side of the droplet bulks over itself due to gravity that makes a larger angle called advancing contact angle while rear side decreases because of the retention effects and this angle is called receding contact angle. Difference between these two is known as contact angle hysteresis [14-17] and it is a crucial feature in droplet dynamic studies. Thin film evolution equation in long-wave or lubrication approximation is a widely used method to qualitatively model these important dynamics. So, before we continue, let's explore the details of the long-wave approximation.

1.2 Lubrication Approximation

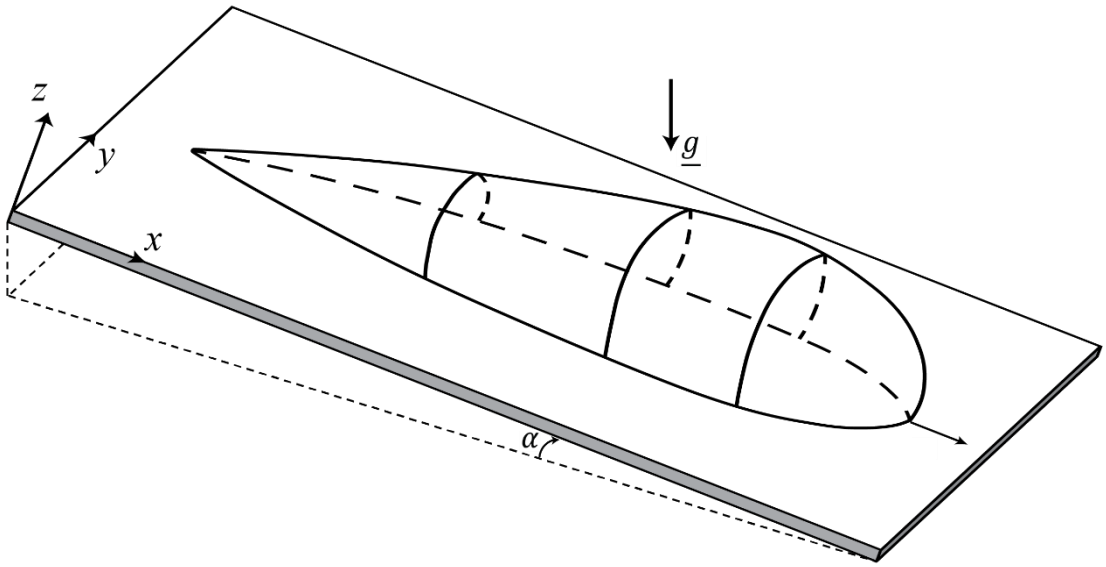

Figure 1.4: Droplet sliding over a tilted flat substrate

In continuum regime the motion of Newtonian fluid particles within the droplet (see Figure 1.4) is governed by

$$\rho\left(\frac{\partial \underline{u}^*}{\partial t^*} + \underline{u}^* \cdot \nabla \underline{u}^*\right) = -\nabla p^* + \mu \nabla^2 \underline{u}^* + \rho \underline{g}, \tag{1.3}$$

where asterisk shows dimensional terms and continuity for incompressible fluid is

$$\frac{\partial u_x^*}{\partial x^*} + \frac{\partial u_y^*}{\partial y^*} + \frac{\partial u_z^*}{\partial z^*} = 0. \tag{1.4}$$

In a typical microfluidic system, length scales are around $L \sim 10\ \mu m$ and the characteristic velocity of the flow scales as $u \sim < 0.01\ m/s$. If the fluid is water ($\rho = 999.7\ kg/m^3$ and $\mu = 0.001308\ kg/(m.s)$ at 10° Celsius), then the Reynolds number (Re) is around 0.01 which is much less than 1, $Re = 0.01 \ll 1$. So, we can conclude that the flow is viscous dominated. In our problem, the velocity along the flow (*x*-*y* axis) is much bigger than the velocity across the flow (*z*-axis) and such flows are considered as quasi-parallel flows (thin and long flow) which allows us to use

lubrication theory [18]. With these two specialties, we alter the Navier-Stokes equation by first non-dimensionalizing equation (1.3) and equation (1.4) with the scales below.

$$u_x^* = u_y^* = u\, u^s \tag{1.5}$$

$$u_z^* = u_z\, u_z^s \tag{1.6}$$

$$x^* = x\, \ell_0 \tag{1.7}$$

$$y^* = y\, \ell_0 \tag{1.8}$$

$$z^* = z\, h_0 \tag{1.9}$$

$$\varepsilon = \frac{z_s}{x_s} = \frac{z_s}{y_s} = \frac{h_0}{\ell_0} \tag{1.10}$$

$$t^* = t\, t^s = t\frac{\ell_0}{u^s} \tag{1.11}$$

$$p^* = p\, p^s \tag{1.12}$$

First, we begin with equation (1.4).

$$\frac{\partial(u_x\, u^s)}{\partial(x\, \ell_0)} + \frac{\partial\left(u_y\, u^s\right)}{\partial(y\, \ell_0)} + \frac{\partial(u_z\, u_z^s)}{\partial(z\, h_0)} = 0 \tag{1.13}$$

We rearrange the equation (1.13) by gathering all scales to *z-axis* component.

$$\frac{\partial(u_x)}{\partial(x)} + \frac{\partial\left(u_y\right)}{\partial(y)} + \frac{\ell_0\, u_z^s}{u^s\, h_0}\, \frac{\partial(u_z)}{\partial(z)} = 0 \tag{1.14}$$

We determine u_z^s by picking the coefficient of the last term in (1.5) as unity as

$$u_z^s = \frac{u^s\, h_0}{\ell_0}. \tag{1.15}$$

Now we use same procedure on Navier-Stokes equation (1.3) by first separating it into its components.

x-component: $$\rho\left(\frac{\partial u_x^*}{\partial t^*} + u_x^*\frac{\partial u_x^*}{\partial x^*} + u_y^*\frac{\partial u_x^*}{\partial y^*} + u_z^*\frac{\partial u_x^*}{\partial z^*}\right)$$

$$= -\frac{\partial p^*}{\partial x^*} + \rho\, g \sin\alpha + \mu\left(\frac{\partial^2 u_x^*}{\partial x^{*2}} + \frac{\partial^2 u_x^*}{\partial y^{*2}} + \frac{\partial^2 u_x^*}{\partial z^{*2}}\right) \tag{1.16}$$

y-component: $$\rho\left(\frac{\partial u_y^*}{\partial t^*} + u_x^*\frac{\partial u_y^*}{\partial x^*} + u_y^*\frac{\partial u_y^*}{\partial y^*} + u_z^*\frac{\partial u_y^*}{\partial z^*}\right)$$

$$= -\frac{\partial p^*}{\partial y^*} + \mu\left(\frac{\partial^2 u_y^*}{\partial x^{*2}} + \frac{\partial^2 u_y^*}{\partial y^{*2}} + \frac{\partial^2 u_y^*}{\partial z^{*2}}\right) \tag{1.17}$$

z-component: $$\rho\left(\frac{\partial u_z^*}{\partial t^*} + u_x^*\frac{\partial u_z^*}{\partial x^*} + u_y^*\frac{\partial u_z^*}{\partial y^*} + u_z^*\frac{\partial u_z^*}{\partial z^*}\right)$$

$$= -\frac{\partial p^*}{\partial z^*} - \rho\, g \cos\alpha + \mu\left(\frac{\partial^2 u_z^*}{\partial x^{*2}} + \frac{\partial^2 u_z^*}{\partial y^{*2}} + \frac{\partial^2 u_z^*}{\partial z^{*2}}\right) \tag{1.18}$$

Again, we use the scales above and non-dimensionalize the equation (1.16).

$$\rho\left(\frac{u^s}{t_s}\frac{\partial u_x}{\partial t} + u^s\frac{u^s}{\ell_0}\frac{\partial u_x}{\partial x}u_x + u^s\frac{u^s}{\ell_0}\frac{\partial u_x}{\partial y}u_y + u_z^s\frac{u^s}{h_0}\frac{\partial u_x}{\partial z}u_z\right)$$

$$= -\frac{p^s}{\ell_0}\frac{\partial p}{\partial x} + \rho\, g \sin\alpha + \mu\left(\frac{u^s}{\ell_0^2}\frac{\partial^2 u_x}{\partial x^2} + \frac{u^s}{\ell_0^2}\frac{\partial^2 u_x}{\partial y^2} + \frac{u^s}{h_0^2}\frac{\partial^2 u_x}{\partial z^2}\right) \tag{1.19}$$

By using the scales (1.10), (1.11) and (1.15), we rearrange equation (1.19).

$$\frac{\rho\, u^{s2}}{\ell_0}\left(\frac{\partial u_x}{\partial t}+\frac{\partial u_x}{\partial x}u_x+\frac{\partial u_x}{\partial y}u_y+\frac{\partial u_x}{\partial z}u_z\right)$$

$$=\ -\frac{p^s}{\ell_0}\frac{\partial p}{\partial x}+\rho\, g\sin\alpha+\mu\frac{u^s}{h_0^2}\left(\varepsilon^2\frac{\partial^2 u_x}{\partial x^2}+\varepsilon^2\frac{\partial^2 u_x}{\partial y^2}+\frac{\partial^2 u_x}{\partial z^2}\right) \qquad (1.20)$$

We divide both side of the equation (1.20) with $\mu\frac{u^s}{h_0^2}$ and make some algebraic adjustments.

$$\frac{\rho\, u^s\, \ell_0}{\mu}\left(\frac{\partial u_x}{\partial t}+\frac{\partial u_x}{\partial x}u_x+\frac{\partial u_x}{\partial y}u_y+\frac{\partial u_x}{\partial z}u_z\right)$$

$$=\ -\frac{p^s h_0^2}{\ell_0\,\mu\,u^s}\frac{\partial p}{\partial x}+\frac{h_0^2}{\mu\,u^s}\rho\, g\sin\alpha+\left(\varepsilon^2\left(\frac{\partial^2 u_x}{\partial x^2}+\frac{\partial^2 u_x}{\partial y^2}\right)+\frac{\partial^2 u_x}{\partial z^2}\right) \qquad (1.21)$$

Here the term $\frac{\rho\, u^s\, \ell_0}{\mu}$ is the Reynolds number (*Re*) that gives the ratio between inertial forces to viscous forces. As we previously mentioned, our flow is viscous dominated, $Re \ll 1$, thus we can nullify the terms that are multiplied with Reynolds number. Also, the flow is thin and long such that we neglect the terms with ε by the fact that $\varepsilon \ll 1$. So, we end up with the equation (1.22).

$$0=\ -\frac{p^s h_0^2}{\ell_0\,\mu\,u^s}\frac{\partial p}{\partial x}+\frac{h_0^2}{\mu\,u^s}\rho\, g\sin\alpha+\frac{\partial^2 u_x}{\partial z^2} \qquad (1.22)$$

From here, we find our pressure scale p^s and find final non-dimensional equation (1.24).

$$p^s=\frac{\mu\, u^s\, \ell_0}{h_0^2} \qquad (1.23)$$

$$0 = -\frac{\partial p}{\partial x} + \frac{h_0^2}{\mu\, u^s}\rho\, g \sin\alpha + \frac{\partial^2 u_x}{\partial z^2} \tag{1.24}$$

Now we re-dimensionalize equation (1.24).

$$0 = -\frac{\partial\left(\frac{p^*}{p^s}\right)}{\partial\left(\frac{x^*}{\ell_0}\right)} + \frac{h_0^2}{\mu\, u^s}\rho\, g \sin\alpha + \frac{\partial^2\left(\frac{u_x^*}{u^s}\right)}{\partial\left(\frac{z^*}{h_0}\right)^2}$$

$$0 = \frac{h_0^2}{\mu\, u^s}\left(-\frac{\partial p^*}{\partial x^*} + \rho\, g \sin\alpha + \mu\frac{\partial^2 u_x^*}{\partial z^{*2}}\right) \tag{1.25}$$

Finally, we get rid of $\frac{h_0^2}{\mu\, u^s}$ term. This ends up with dimensional *x*-component of lubrication equation.

$$0 = -\frac{\partial p^*}{\partial x^*} + \rho\, g \sin\alpha + \mu\frac{\partial^2 u_x^*}{\partial z^{*2}} \tag{1.26}$$

Same procedure is followed for *y* and *z* components of Navier-Stokes equation but for clarity purposes, we don't include them. They are given below as equation (1.27) and (1.28).

$$0 = -\frac{\partial p^*}{\partial y^*} + \mu\frac{\partial^2 u_y^*}{\partial z^{*2}} \tag{1.27}$$

$$0 = -\frac{\partial p^*}{\partial z^*} - \rho\, g \cos\alpha \tag{1.28}$$

The length of droplet is much bigger than its thickness ($L >> f$), height of the droplet requires there to be a pressure gradient along the flow axis to satisfy mass-conservation. Because of that pressure terms cannot be neglected. By this way, we've altered the Navier-Stokes equation into lubrication equation.

1.3 Literature Survey

Free surfaces of the droplet and moving contact line are the main issues in our model. Fluid moving over a solid substrate shows a stick-slip motion referred to as no-slip condition. However, we do know that our contact line is moving so there is a contradiction to no-slip condition. This lack of physics or singularity at the contact line must be alleviated in order to obtain accurate results [19]. Slip length [20-24] or disjoining pressure model [25-29] is adopted in the literature to resolve this problem. First one imposes a slip length at the contact line to relieve the no-slip boundary condition. Latter method introduces a really thin-film, known as precursor film, over substrate to incorporate molecular interactions between solid-liquid interface. In other words, we assume that the droplet is sliding over this thin film rather than a solid surface (see Figure 1.5).

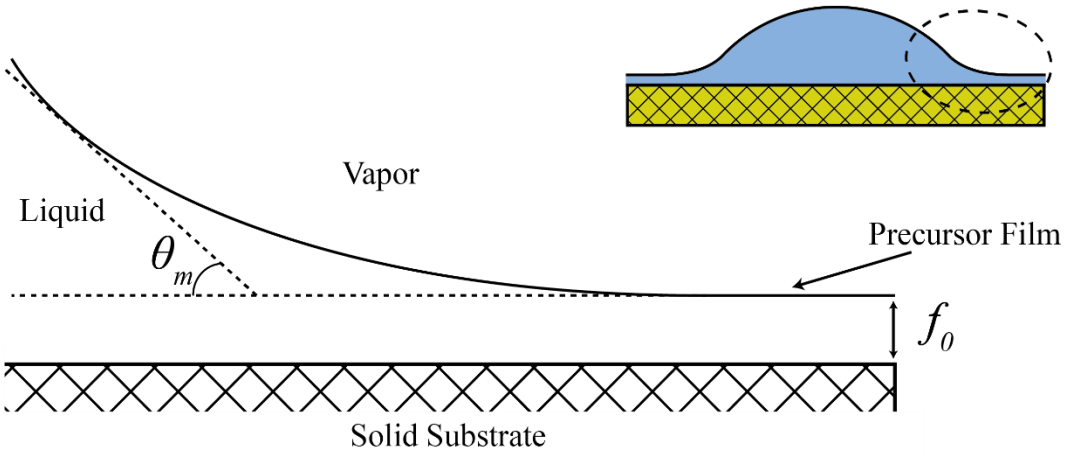

Figure 1.5: Presentation of precursor film thickness (f_0) on solid substrate

Angle θ_m is the mesoscopic angle that replaces our macroscopic contact angle. Under normal circumstances, we derive the macroscopic contact angle from the surface energies at the three-phase contact line as we previously mentioned. However, by adding a thin film over our substrate, we lose the real contact line. Thus, we define a new angle that depends on wetting potential [30]. Even though both methods have its own downsides and upsides, it is reported that they both lead to similar dynamics [31]. Reducing the thin-film equation into a two-dimensional problem is a common approach in the literature and it revealed numerous physical qualities. For instance, Ceyhan et al. [32] analyze a sliding droplet over a single topography defined as

hyperbolic tangent function. They demonstrate the retention force increment for higher slope steps and domination over gravity by a simple force balance at the pinned contact line. They show that the pinning occurs at the most negative slope of the topography and the transition of pinning-depinning can be fit in a phase diagram with numerical experiments. If frequency of the step is increased, droplet deposition may occur at the receding contact line depending on the step. Surface heterogeneity does not have to be limited to surface roughness. It could be defined as chemical or both as well. Thiele [33] investigate different pinning types on heterogeneous substrates and incorporate depinning process as a bifurcation problem on hydrophobic and hydrophilic steps. They observe two different types of depinning where droplet depins from hydrophilic defect by destabilizing at a saddle-node bifurcation referred as sniper bifurcation. For hydrophobic steps, pinned droplet destabilizes again but this time with an additional feature which is back and forth oscillation. Many other studies have been conducted experimentally [34-39] and theoretically [40-46] to investigate these behaviors and yet there are questions to be answered.

These physical aspects can be analyzed realistically despite being reduced into two-dimensional cases [47]. However, ignoring lateral effects in two-dimension detains us from important features. For instance, a droplet sliding over a tilted substrate may form a cusp at the receding corner and beyond the critical velocity or capillary number which is the dimensionless number giving the ratio of viscous forces to capillary forces, these cusps break and emit a pearl to the surface [48,49]. These features are all three-dimensional. Also, study conducted by Thiele [47] observe different morphologies and droplet profiles that we don't get in two-dimension. Therefore, three-dimensional study is required for detailed examination of droplet dynamics.

Podgorski's experimental study [49] is renowned in three-dimensional problems. Droplet formations and transition between these formations are investigated for silicon oil and water. His results show that there exists linear relation between $Bo \sin \alpha$, where α is the inclination angle of domain, and capillary number. After critical threshold is passed, droplet forms corners and cusps in which further increment of tilt angle promotes pearling formation. Snoeijer [50] analyze this corner and rivulet formation with lubrication approximation. He relates the speed of the droplet with the corner angle to explain the transition from corner to rivulet formation. Winkels [51] conducts

similar study where they analyze V-shape receding contact lines with Immersion Lithography. They find that as the contact line speed increases, linear relation between cube of dynamic and static contact angle to capillary number known as Cox-Voinov law [52] loses its validity due to corner formation. Schwartz [53] presents simple dynamical analysis of a droplet on vertical wall. He examines droplet formations for single non-dimensional control parameter. These are the studies that inspects fundamental dynamics. There exist specific studies in the literature based on delaying and trapping droplets. For instance, Espin [54] imposes an external shear to system for delaying contact line motion. He also uses a permeable substrate and reveals that pearling formations can be suppressed due to decreasing volume of the droplet. Other experimental [34,55] and theoretical [33,30] studies introduce chemical heterogeneity to pin or delay the contact line.

1.4 Motivation of the Study

Even though there exist various types of studies for three-dimensional droplet dynamics, entrapment of droplets has received little attention. Thus, we study the motion of three-dimensional slender droplet on a rough surface to understand the physics behind the entrapment of droplets. Instead of using chemical heterogeneity, we investigate surface roughness to manipulate contact angle hysteresis and other dynamics that we discuss in this thesis. Sinusoidal wave function is used to associate this roughness which is a surface with continuous peaks and troughs.

Organization of the thesis is as follows. In Chapter 2, problem domain is introduced and non-dimensional evolution equation is obtained. Numerical method and solver are explained in Chapter 3. Our own data structure, preload data structure, is explained with whole adaptive mesh refinement method in Chapter 4. Results from the solver are validated with well-known laws and compared with experiments from the literature in Chapter 5. Mechanism of droplet entrapment is explained in Chapter 6. Finally, conclusion is given in Chapter 7.

Chapter 2

Model Problem

In this chapter, we represent our problem domain and derive dimensional film evolution equation from lubrication equation $(1.26 - 1.28)$. Contact angle hysteresis, pinning-depinning transitions and similar physical actions are highly related to force balance at the three-phase interface of a droplet. Simplification of a domain is a cunning way to solely focus on this force balance which allows us to apprehend this mechanics. In our previous study [32], we use this concept to analyze a single hyperbolic tangential topography at the end of domain and we revealed that the slope of this surface heterogeneity is responsible from pinning-depinning transitions. In the light of our previous study, we define our domain (see Figure 2.1) as a chemically homogenous substrate with a sinusoidal topography to imitate surface roughness. For various amplitudes and frequencies, we investigate trapped or pinned residual droplets.

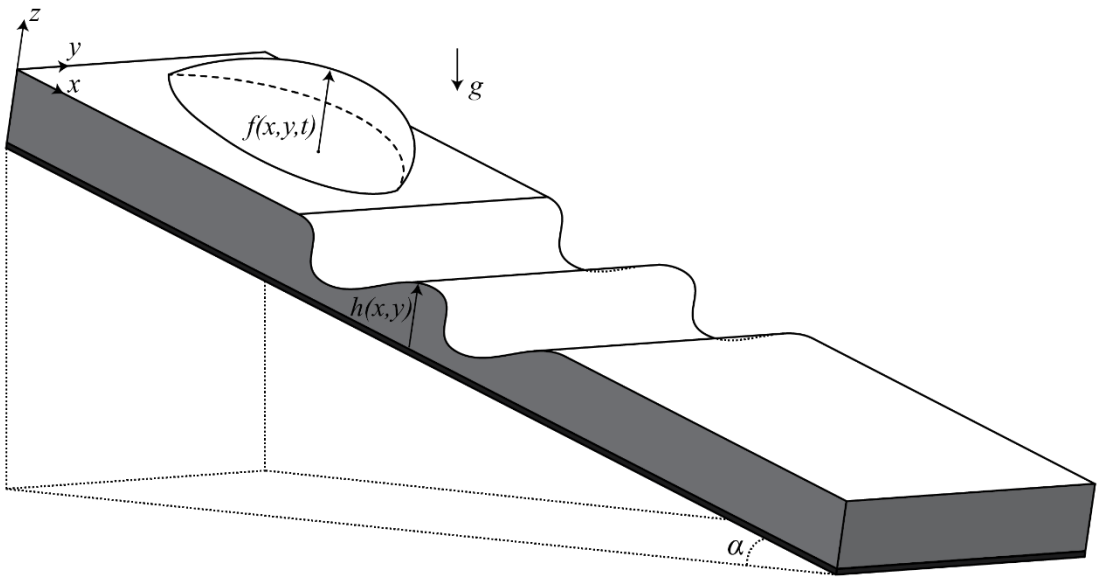

Figure 2.1: Problem domain, droplet sliding on a substrate with sinusoidal topography

Here, parameters α, $f(x,y,t)$, $h(x,y)$ and $\underline{g}$ are inclination angle, droplet thickness, film surface, topography function and magnitude of gravitation acceleration, respectively. The topography function is defined as follows:

$$h(x,y) = \text{Å}\left(\sin\frac{2\pi}{\lambda}\, x\right). \tag{2.1}$$

Parameters λ and Å are wavelength and amplitude of the sine wave. We utilize these parameters to configure the slope of our topography function. To derive dimensional film-evolution equation, we use equation (1.26), equation (1.27) and equation (1.28).

$$0 = -\frac{\partial p^*}{\partial x^*} + \rho\, g \sin\alpha + \mu\frac{\partial^2 u_x^*}{\partial {z^*}^2} \tag{1.26}$$

$$0 = -\frac{\partial p^*}{\partial y^*} + \mu\frac{\partial^2 u_y^*}{\partial {z^*}^2} \tag{1.27}$$

$$0 = -\frac{\partial p^*}{\partial z^*} - \rho\, g \cos\alpha \tag{1.28}$$

To obtain our flow model, we integrate these equations with following boundary conditions. First one is previously mentioned as no-slip boundary condition where the fluid sticks to the solid substrate and shears the flow: at $z^* = h^*$, $u_x^* = u_y^* = 0$. Second is coming from the tangential component of interfacial momentum balance on liquid-gas interface. Mathematically, at $z^* = h^* + f^* = \zeta^*$, $\frac{\partial u_x^*}{\partial z^*} = \frac{\partial u_y^*}{\partial z^*} = 0$. We get the velocity profile along the *x*-axis by integrating equation (1.26) with respect to *z*-axis.

$$u_x^*(z^*) = \frac{1}{2\mu}\left(\frac{\partial p^*}{\partial x^*} - \rho g \sin\alpha\right){z^*}^2 + C_1 z^* + C_2 \tag{2.2}$$

We use the second boundary condition, $z^* = \zeta^*$, to find unknown constant C_1.

$$\frac{1}{\mu}\left(\frac{\partial p^*}{\partial x^*} - \rho g \sin\alpha\right)\zeta^* + C_1 = 0$$

$$C_1 = -\frac{1}{\mu}\left(\frac{\partial p^*}{\partial x^*} - \rho g \sin\alpha\right)\zeta^* \tag{2.3}$$

Latter constant, C_2, is found by using the no-slip boundary condition and constant in equation (2.3).

$$\frac{1}{2\mu}\left(\frac{\partial p^*}{\partial x^*} - \rho g \sin\alpha\right)h^{*2} + C_1 h^* + C_2 = 0$$

$$C_2 = -\frac{h^{*2} - 2\rho h}{2\mu}\left(\frac{\partial p^*}{\partial x^*} - \rho g \sin\alpha\right) \tag{2.4}$$

Substituting the constants (2.3) and (2.4) into equation (2.2) gives us the *x*-component of the velocity as

$$u_x^*(z^*) = \left(\frac{\partial p^*}{\partial x^*} - \rho g \sin\alpha\right)\frac{(z^* - h^*)(z^* - h^* - 2f^*)}{2\mu}. \tag{2.5}$$

With the same boundary conditions, we find velocity along *y*-axis from equation (1.27).

$$u_y^*(z^*) = \left(\frac{\partial p^*}{\partial y^*}\right)\frac{(z^* - h^*)(z^* - h^* - 2f^*)}{2\mu} \tag{2.6}$$

Equation (1.28) yields the pressure distribution of the system as follows.

$$p^*(x^*, y^*, z^*) = -\rho g \cos\alpha\, z^* + C_3 \tag{2.7}$$

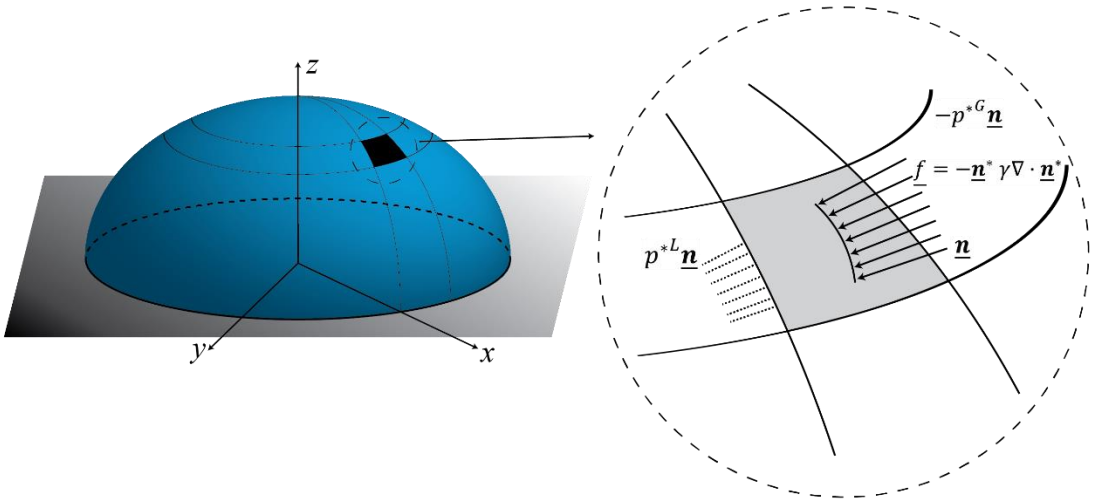

Figure 2.2: Hydrostatic force balance at the liquid-vapor interface

The normal stress balance at the liquid-vapor interface is

$$p^{*L} - p^{*G} = \gamma \nabla \cdot \underline{n}^* - \Pi^*, \tag{2.8}$$

where p^{*L}, p^{*G}, γ, $\underline{n}^*$, $\nabla \cdot \underline{n}^*$ and Π^* are liquid-gas pressure, surface tension, normal vector of liquid-gas interface, divergence of normal vector of liquid gas-interface and disjoining pressure [56], respectively. At the liquid-vapor interface, $z^* = \zeta^*$, we make an interfacial momentum balance on chosen control volume for a uniform surface tension. Our interface is defined as $z^* - \zeta^*(x^*, y^*) = 0$. Normal vector from this interface is defined below.

$$\underline{n}^* = \frac{\nabla(z^* - \zeta^*(x^*, y^*))}{|\nabla(z^* - \zeta^*(x^*, y^*))|} \tag{2.9}$$

$$\nabla \cdot \underline{n}^* = \frac{\partial}{\partial x^*}\left(\frac{\underline{k} - \frac{\partial \zeta^*}{\partial x^*}\underline{i} - \frac{\partial \zeta^*}{\partial y^*}\underline{j}}{\sqrt{1 + \left(\frac{\partial \zeta^*}{\partial x^*}\right)^2 + \left(\frac{\partial \zeta^*}{\partial y^*}\right)^2}}\right) + \frac{\partial}{\partial y^*}\left(\frac{\underline{k} - \frac{\partial \zeta^*}{\partial x^*}\underline{i} - \frac{\partial \zeta^*}{\partial y^*}\underline{j}}{\sqrt{1 + \left(\frac{\partial \zeta^*}{\partial x^*}\right)^2 + \left(\frac{\partial \zeta^*}{\partial y^*}\right)^2}}\right) \tag{2.10}$$

Terms with square roots of ζ simplify to unity due to small slope interface. Then the normal at the interface simplifies to

$$\nabla \cdot n^* = -\frac{\partial^2 \zeta^*}{\partial x^{*2}} - \frac{\partial^2 \zeta^*}{\partial y^{*2}}. \tag{2.11}$$

For $z^* = \zeta^*$, the general pressure, equation (2.7), is equal to liquid pressure at liquid-gas interface, equation (2.8). From this relation, we find the constant C_3.

$$p^*(x^*, y^*, \zeta^*) = p^{*L} = -\rho g \cos\alpha\, \zeta + C_3$$

$$p^{*G} + \gamma \nabla \cdot \underline{n}^* - \Pi^* = -\rho g \cos\alpha\, \zeta + C_3$$

$$C_3 = p^{*G} + \rho g \cos\alpha\ \zeta^* + \gamma \nabla \cdot \underline{n}^* - \Pi^* \tag{2.12}$$

We substitute the constant in equation (2.12) into equation (2.7) to find general pressure distribution of our system, equation (2.13).

$$p^*(x^*, y^*, z^*) = (\rho g \cos\alpha)\,(f^* + h^* - z^*) + p^{*G} + \gamma \nabla \cdot \underline{n}^* - \Pi^* \tag{2.13}$$

The disjoining pressure is the excess pressure that emerges from thin film because of the cumulative effects of van der Waals, ion-electrostatic and structural forces. We use two-term disjoining pressure model [25] to account such interactions.

$$\Pi^* = H\left[\left(\frac{f_0}{f^*}\right)^n - \left(\frac{f_0}{f^*}\right)^m\right] \tag{2.14}$$

where H is the non-dimensional Hamakar constant [57] given by

$$H = \frac{1}{f_0}\left(\frac{\theta_e \sin\theta_e}{1 - \cos\theta_e}\right)^2 \frac{(n-1)(m-1)}{2\,(n-m)}. \tag{2.15}$$

Parameters n and m are positive constants and they relate the level of liquid-solid repulsion and attraction, respectively. They are chosen as $n > m > 1$. Finally, f_0 is the thin stable film to alleviate singularities at the contact line, also known as precursor film thickness. Thin stable film is a crucial parameter for convenient droplet dynamics and its effect is discussed widely in further sections.

Coming sections require the change of pressure at *x* and *y* axes. To find the pressure distribution along each axis, derivative of equation (2.13) is taken with related Cartesian coordinates. We neglect the changes in gas pressure, p^{*G}, because it is uniform along the domain.

$$\frac{\partial p^*}{\partial x^*} = \rho g \cos\alpha \frac{\partial \zeta^*}{\partial x^*} + \gamma \frac{\partial}{\partial x^*} (\nabla \cdot \underline{n}) - \Pi_x^* \tag{2.16}$$

$$\frac{\partial p^*}{\partial y^*} = \rho g \cos\alpha \frac{\partial \zeta^*}{\partial y^*} + \gamma \frac{\partial}{\partial y^*} (\nabla \cdot \underline{n}) - \Pi_y^* \tag{2.17}$$

2.1 Unsteady Film-Evolution Equation

To explain this sub-section, we return to Figure 1.4. But this time we consider the film thickness (*f*) which is a function of space and time. For two-dimensional case, we can write volume flow rate for unit depth as follows.

$$q = \int_0^{f(x,t)} u_x \, dy \tag{2.18}$$

We rewrite the change of volume flow rate about *x*-axis with Leibnitz theorem and using a property coming from the continuity equation as follows.

$$\frac{dq}{dx} = -u_y(x,f) + u_x \frac{\partial f}{\partial x} \Big|_f \tag{2.19}$$

Our interface is material. So, we take material derivative at the liquid-vapor interface.

$$\frac{D}{Dt}\big(y - f(x,t)\big) = 0$$

$$\frac{\partial f}{\partial t} = u_y - u_x \frac{\partial f}{\partial x}$$

$$\frac{\partial f}{\partial t} = -\frac{dq}{dx} \tag{2.20}$$

We combine equation (2.19) and equation (2.20) to obtain unsteady film-evolution equation.

$$\frac{\partial f^*}{\partial t^*} + \nabla \cdot \underline{q}^* = 0 \tag{2.21}$$

Here $\underline{q}^*$ is the volume flow rate and has two components. Volume flow rate on any axis is found by integrating associated axial velocity between solid substrate and droplet. From this denotation, volume flow rate along *x*-axis (q_x) and *y*-axis (q_y) are obtained as

$$q_x^* = \int_{h^*}^{f^*+h^*} \left(\frac{\partial p^*}{\partial x^*} - \rho g \sin\alpha\right) \frac{(z^* - h^*)(z^* - h^* - 2f^*)}{2\mu}\, dz$$

$$q_x^* = -\frac{f^{*3}}{3\mu}\left(\frac{\partial p^*}{\partial x^*} - \rho g \sin\alpha\right), \tag{2.22}$$

$$q_y^* = \int_{h^*}^{f^*+h^*} \frac{1}{2\mu}\frac{\partial p^*}{\partial y^*}\,(z^* - h^*)(z^* - h^* - 2f^*)$$

$$q_y^* = -\frac{f^{*3}}{3\mu}\frac{\partial p^*}{\partial y^*}. \tag{2.23}$$

At this moment, we have all required information. We combine equation (2.21), (2.22) and (2.23) to finalize our dimensional unsteady film-evolution equation.

$$\frac{\partial f^*}{\partial t^*} + \frac{\partial}{\partial x^*}\left[-\frac{f^{*3}}{3\mu}\left(\frac{\partial p^*}{\partial x^*} - \rho g \sin\alpha\right)\right] + \frac{\partial}{\partial y^*}\left[-\frac{f^{*3}}{3\mu}\frac{\partial p^*}{\partial y^*}\right] = 0 \tag{2.24}$$

2.2 Non-dimensional Film-Evolution Equation

We non-dimensionalize the film evolution equation as follows. As a starting point, we approximate the shape of a droplet as a spherical cap [58] meeting the substrate at a defined contact angle θ.

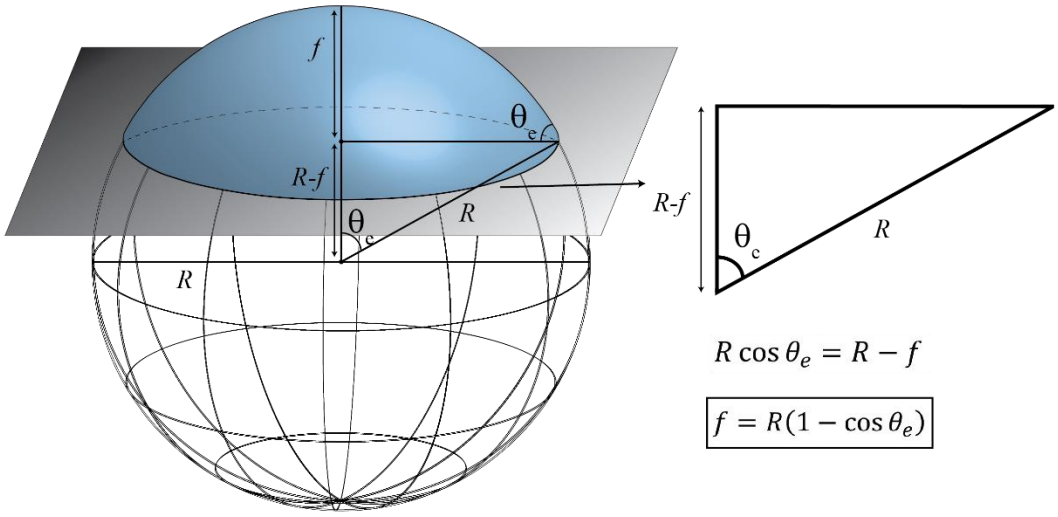

Figure 2.3: Droplet is represented as a spherical cap with an equilibrium angle of θ_e

Parameters are non-dimensionalized with the following scales.

$$x^* = R\ \sin\theta_e\ x \tag{2.25}$$

$$y^* = R\ \sin\theta_e\ y \tag{2.26}$$

$$z^* = R\,(1-\cos\theta_e)\,z \tag{2.27}$$

$$t^* = \frac{\mathrm{R}\sin\theta_e}{u_s}\,t \tag{2.28}$$

$$\varepsilon = \frac{z_s}{x_s} = \frac{z_s}{x_s} = \frac{1-\cos\theta_e}{\sin\theta_e} \tag{2.29}$$

Velocity and pressure related parameters, u^s and Π_s are found by rearranging the film evolution equation with scales above. After the alterations, we find the unknown scales by equalizing the accompanied constants to unity. Details are given in Appendix A to maintain the clarity of the thesis.

$$u^s = \frac{\varepsilon^3\,\gamma}{3\mu} \tag{2.30}$$

$$\Pi_s = \frac{\gamma\,\varepsilon}{R\ \sin\theta_e} \tag{2.31}$$

$$t_s = \frac{R\ \sin\theta_e\ 3\mu}{\gamma\,\varepsilon^3} \tag{2.32}$$

$$Bo = \frac{\rho\,g\,(R\ \sin\theta_e)^2}{\gamma} \tag{2.33}$$

Here in equation (2.33), Bo is the non-dimensional Bond number that measures the ratio of gravitational forces to surface forces. We should note that Bo definition here is based on x_s, later we compare with $Bo_{\mathcal{V}}$ defined using $\mathcal{V}^{\frac{2}{3}}$. We initialize our droplet with the scales above as given in equation (2.34).

$$f(x,y,t) = f_0 + \frac{\cos\theta_e + \sin\theta_e \sqrt{\frac{1}{\sin^2\theta_e} - (x-x_0)^2 - (y-y_0)^2}}{(1-\cos\theta_e)} \qquad (2.34)$$

Finally, we find non-dimensional unsteady film evolution equation as in equation (2.35).

$$\frac{\partial f}{\partial t} + \frac{\partial}{\partial x}\left[-f^3\left(Bo\cos\alpha\frac{\partial(f+h)}{\partial x} - \frac{\partial^3(f+h)}{\partial x^3} - \frac{\partial^2(f+h)}{\partial y^2}\frac{\partial}{\partial x}\right)\right]$$

$$+\frac{\partial}{\partial x}\left[-f^3\left(-\frac{\partial\Pi}{\partial x} - \frac{Bo}{\varepsilon}\sin\alpha\right)\right] + \frac{\partial}{\partial y}\left[-f^3\left(Bo\cos\alpha\frac{\partial(f+h)}{\partial y}\right)\right]$$

$$+\frac{\partial}{\partial y}\left[-f^3\left(-\frac{\partial^3(f+h)}{\partial y^3} - \frac{\partial^2(f+h)}{\partial x^2}\frac{\partial}{\partial y} - \frac{\partial\Pi}{\partial y}\right)\right] = 0 \qquad (2.35)$$

Chapter 3

Numerical Method

In this chapter, we present the details of finite element method to solve our non-dimensional unsteady film-evolution equation which is 4th order non-linear partial differential equation. Weak formulation and quadratic shape functions are given in §3.1. Finite element approximations and time integration is explained in §3.2. Cartesian coordinates are transformed into a natural coordinate system to relate the terms with derivatives in §3.3. Dirichlet and Neumann boundary conditions are introduced for symmetric domains for different types of problems in §3.4.

3.1 Weak Formulation and Shape Functions

3.1.1 Weak Formulation

To integrate the evolution equation (2.35), space and time is discretized by quadratic finite elements and second order backward differentiation formula (BDF) with variable step. The equation (2.35) is valid in a domain Ω: $0 \leq x \leq L_x$ and $0 \leq y \leq L_y$, L_x and L_y being the domain lengths along *x* and *y* axes, respectively. Test functions and *f* are approximated from the same Hilbert-Sobolov space $H_1(\Omega)$. Evolution equation is separated into a set of two coupled equations where second system consists of pressure related terms.

$$\frac{\partial f}{\partial t} + \nabla \cdot \left[-f^3\left(\nabla(Bo\cos\alpha\,(f+h) - \mathcal{P})\right)\right] + \frac{\partial}{\partial x}\left(f^3\frac{Bo}{\varepsilon}\sin\alpha\right) = 0 \quad (3.1)$$

$$\nabla \cdot \nabla(f + h) + \Pi = \mathcal{P} \tag{3.2}$$

The weak formulation of the set of equations are obtained by first multiplying with corresponding test functions, namely $\overline{f}$ and $\overline{p}$. Then they are integrated over the domain Ω. For the clarity purposes, only equation (3.2) is used to demonstrate how to obtain weak formulation. Weak formulation of equation (3.1) can be found in Appendix B.

$$\left(\frac{\partial}{\partial x}\,\underline{i} + \frac{\partial}{\partial y}\,\underline{j}\right) \cdot \left(\frac{\partial}{\partial x}\,\underline{i} + \frac{\partial}{\partial y}\,\underline{j}\right)(f + h) + \Pi = \mathcal{P}$$

$$\frac{\partial^2 f}{\partial x^2} + \frac{\partial^2 h}{\partial x^2} + \frac{\partial^2 f}{\partial y^2} + \frac{\partial^2 h}{\partial y^2} + \Pi = \mathcal{P}$$

$$\int_\Omega \frac{\partial^2 f}{\partial x^2}\,\overline{p}\,\mathrm{d}\Omega + \int_\Omega \frac{\partial^2 h}{\partial x^2}\,\overline{p}\,\mathrm{d}\Omega + \int_\Omega \frac{\partial^2 f}{\partial y^2}\,\overline{p}\,\mathrm{d}\Omega + \int_\Omega \frac{\partial^2 h}{\partial y^2}\,\overline{p}\,\mathrm{d}\Omega$$

$$+ \int_\Omega \Pi\,\overline{p}\,\mathrm{d}\Omega = \int_\Omega \mathcal{P}\,\overline{p}\,\mathrm{d}\Omega \tag{3.3}$$

Here, topography functions are constant. Thus, they are taken into the right side and unknown terms, *f* and Ƥ, are gathered at the left side of the equation.

$$\int_{\partial\Omega} \frac{\partial}{\partial x}\left(\frac{\partial f}{\partial x}\,\overline{p}\right)\mathrm{d}\Omega - \int_\Omega \frac{\partial f}{\partial x}\frac{\partial \overline{p}}{\partial x}\,\mathrm{d}\Omega + \int_{\partial\Omega} \frac{\partial}{\partial y}\left(\frac{\partial f}{\partial y}\,\overline{p}\right)\mathrm{d}\Omega - \int_\Omega \frac{\partial f}{\partial y}\frac{\partial \overline{p}}{\partial y}\,\mathrm{d}\Omega$$

$$+ \int_\Omega \Pi\,\overline{p}\,\mathrm{d}\Omega - \int_\Omega \mathcal{P}\,\overline{p}\,\mathrm{d}\Omega = -\int_\Omega \frac{\partial^2 h}{\partial x^2}\,\overline{p}\,\mathrm{d}\Omega - \int_\Omega \frac{\partial^2 h}{\partial y^2}\,\overline{p}\,\mathrm{d}\Omega \tag{3.4}$$

Unknown terms are modified to weaken the differentiability requirement using the fact that the test functions are chosen to be zero at any Dirichlet boundary condition ($|_{\Gamma} = 0$). Then, we end up with the weak formulation of equation (3.2) as below.

$$\int_{\Omega} \mathrm{P}\,\overline{p}\,\mathrm{d}\Omega + \int_{\Omega} \frac{\partial f}{\partial x}\frac{\partial \overline{p}}{\partial x}\,\mathrm{d}\Omega + \int_{\Omega} \frac{\partial f}{\partial y}\frac{\partial \overline{p}}{\partial y}\,\mathrm{d}\Omega - \int_{\Omega} \Pi\,\overline{p}\,\mathrm{d}\Omega$$

$$= \int_{\Omega} \frac{\partial^2 h}{\partial x^2}\,\overline{p}\,\mathrm{d}\Omega + \int_{\Omega} \frac{\partial^2 h}{\partial y^2}\,\overline{p}\,\mathrm{d}\Omega \tag{3.5}$$

Notice that the disjoining pressure Π is taken to left side, because it is a function of film thickness (f). Weak formulation of equation (3.1) is found with the same procedure above.

$$\int_{\Omega} \frac{\partial f}{\partial t}\,\overline{f}\,\mathrm{d}\Omega + Bo\cos\alpha\left(\int_{\Omega} f^3\frac{\partial f}{\partial x}\frac{\partial \overline{f}}{\partial x}\,\mathrm{d}\Omega + \int_{\Omega} f^3\frac{\partial f}{\partial y}\frac{\partial \overline{f}}{\partial y}\,\mathrm{d}\Omega\right)$$

$$Bo\cos\alpha\left(+\int_{\Omega} f^3\frac{\partial h}{\partial x}\frac{\partial \overline{f}}{\partial x}\,\mathrm{d}\Omega + \int_{\Omega} f^3\frac{\partial h}{\partial y}\frac{\partial \overline{f}}{\partial y}\,\mathrm{d}\Omega\right) - \int_{\Omega} f^3\frac{\partial \mathrm{P}}{\partial x}\frac{\partial \overline{f}}{\partial x}\,\mathrm{d}\Omega$$

$$-\int_{\Omega} f^3\frac{\partial \mathrm{P}}{\partial y}\frac{\partial \overline{f}}{\partial y}\,\mathrm{d}\Omega - \frac{Bo}{\varepsilon}\sin\alpha\int_{\Omega} f^3\frac{\partial \overline{f}}{\partial x}\,\mathrm{d}\Omega = 0 \tag{3.6}$$

3.1.2 Shape Functions

We use shape functions or basis functions to map a two-dimensional Cartesian system into natural coordinates within the Gauss quadrature rule where the domain is given in $-1 \leq r \leq 1$ and $-1 \leq s \leq 1$ (see Figure 3.1).

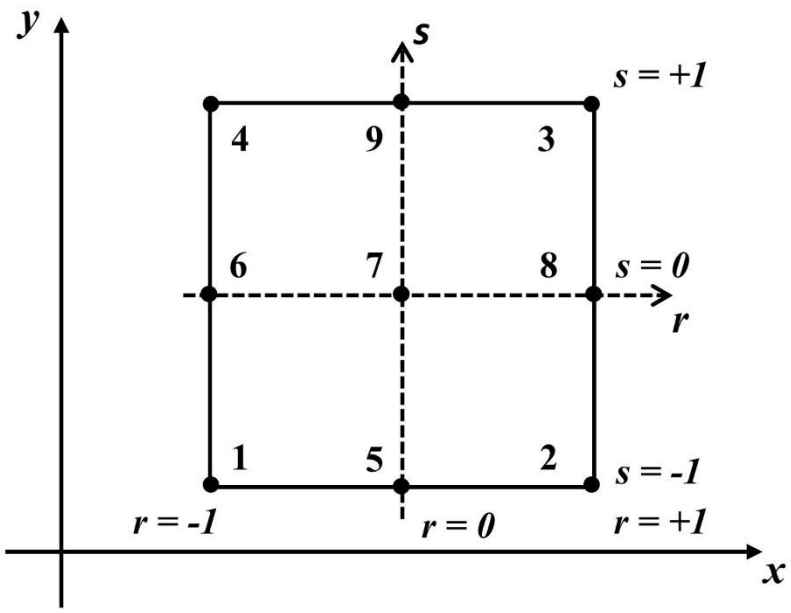

Figure 3.1: Nine variable number nodes of two-dimensional element [59]

Corresponding interpolation functions or quadratic shape functions for nine variable number nodes of two-dimensional element in Figure 3.1 that we use in our finite element solver are given in Table 3.1.

Table 3.1: Quadratic interpolation functions according to Figure 3.1

i = 1	$\varphi_1 = 0.25\,(1-r)\,(1-s) - 0.5\,\varphi_6 - 0.5\,\varphi_5 - 0.25\,\varphi_7$
i = 2	$\varphi_2 = 0.25\,(1+r)\,(1-s) - 0.5\,\varphi_5 - 0.5\,\varphi_8 - 0.25\,\varphi_7$
i = 3	$\varphi_3 = 0.25\,(1+r)\,(1+s) - 0.5\,\varphi_9 - 0.5\,\varphi_8 - 0.25\,\varphi_7$
i = 4	$\varphi_4 = 0.25\,(1-r)\,(1+s) - 0.5\,\varphi_9 - 0.5\,\varphi_6 - 0.25\,\varphi_7$
i = 5	$\varphi_5 = 0.5\,(1-r^2)\,(1-s) - 0.25\,\varphi_7$
i = 6	$\varphi_6 = 0.5\,(1-s^2)\,(1-r) - 0.25\,\varphi_7$
i = 7	$\varphi_7 = (1-r^2)\,(1-s^2)$
i = 8	$\varphi_8 = 0.5\,(1-s^2)\,(1+r) - 0.25\,\varphi_7$
i = 9	$\varphi_9 = 0.5\,(1-r^2)\,(1+s) - 0.25\,\varphi_7$

These shape functions are defined as piecewise continuous polynomials over sub elements and satisfy the condition $\varphi_i(x_j) = \delta_{ij} = \{0, if\ i \neq j \mid 1, if\ i = j\}$.

3.2 Finite Element Approximations and Time Integrations

We use piecewise continuous quadratic shape functions (φ^q) given in Table 3.1 to discretize the space. Approximation of f and $\mathcal{P}$ with corresponding test functions in isoparametric domain are given below.

$$f^{n+2} = \sum_{j=1}^{N} f_j^{n+2}\, \varphi_j^q(r,s) \tag{3.7}$$

$$\mathcal{P}^{n+2} = \sum_{j=1}^{N} \mathcal{P}_j^{n+2}\, \varphi_j^q(r,s) \tag{3.8}$$

$$f^{n+1} = \sum_{j=1}^{N} f_j^{n+1}\, \varphi_j^q(r,s) \tag{3.9}$$

$$\mathcal{P}^{n+1} = \sum_{j=1}^{N} \mathcal{P}_j^{n+1}\, \varphi_j^q(r,s) \tag{3.10}$$

$$f^{n} = \sum_{j=1}^{N} f_j^{n}\, \varphi_j^q(r,s) \tag{3.11}$$

$$\mathcal{P}^{n} = \sum_{j=1}^{N} \mathcal{P}_j^{n}\, \varphi_j^q(r,s) \tag{3.12}$$

$$\overline{f} = \sum_{i=1}^{N} f_i\, \varphi_i^q(r,s) \tag{3.13}$$

$$\overline{p} = \sum_{i=1}^{N} p_i \, \varphi_i^q(r,s) \tag{3.14}$$

Here, f_j and p_j are the nodal values and the weak formulations are valid for all f_i and p_i. For the time integration we use second order variable step backward differentiation formula. We approximate the unsteady term by

$$\frac{\partial f}{\partial t} = a\, f^{n+2} + b\, f^{n+1} + c\, f^{n}, \tag{3.15}$$

where *a*, *b* and *c* are constants that are coming from Taylor expansion as

$$a = \frac{(\tau_{n+1} + \tau_n)^2 - (\tau_{n+1})^2}{\tau_{n+1}\, \tau_n\, (\tau_{n+1} + \tau_n)}, \tag{3.15.a}$$

$$b = \frac{-(\tau_{n+1} + \tau_n)}{\tau_n\, \tau_{n+1}}, \tag{3.15.b}$$

$$c = \frac{\tau_{n+1}}{\tau_n\, (\tau_{n+1} + \tau_n)}. \tag{3.15.c}$$

When step size (Δt) is uniform, $\tau_{n+1} = \Delta t$ and $\tau_n = \Delta t$, equation (3.15) becomes second order backward differentiation, i.e.

$$\frac{2\Delta t}{3}\, \frac{\partial f}{\partial t} = f^{n+2} + \frac{4}{3} f^{n+1} + \frac{1}{3} f^{n}. \tag{3.15.d}$$

So, we put these relations into the weakened equations (3.5) and (3.6). In compact form, approximated equations are given below.

$$\sum_{j=1}^{N} f_j^{n+2} M_{ij} + \frac{1}{a}\, Bo \cos\alpha \left(\sum_{j=1}^{N} f_j^{n+2} \left(NL1x_{ij} + NL2x_{ij} + NL1y_{ij} \right) \right)$$

$$+ \frac{1}{a}\, Bo \cos\alpha \left(\sum_{j=1}^{N} f_j^{n+2} NL2y_{ij} \right) - \frac{1}{a} \left(\sum_{j=1}^{N} \mathrm{P}_j^{n+2} \left(NL1x_{ij} + NL1y_{ij} \right) \right)$$

$$- \frac{1}{a} \frac{Bo}{\varepsilon} \sin\alpha \sum_{j=1}^{N} f_j^{n+2} NL4_{ij} = - \frac{b}{a} \sum_{j=1}^{N} f_j^{n+1} M_{ij} - \frac{c}{a} \sum_{j=1}^{N} f_j^{n} M_{ij} \qquad (3.16)$$

$$\sum_{j=1}^{N} \mathrm{P}_j^{n+2} M_{ij} + \sum_{j=1}^{N} f_j^{n+2} \left(Bx_{ij} + By_{ij} \right) - H\, f_0^3 \sum_{j=1}^{N} f_j^{n+2} NL2_{ij}$$

$$+ H\, f_0^2 \sum_{j=1}^{N} f_j^{n+2} NL3_{ij} = \int_{\Omega} \frac{\partial^2 h}{\partial x^2}\, \varphi_i \, \mathrm{d}\Omega + \int_{\Omega} \frac{\partial^2 h}{\partial y^2}\, \varphi_i \, \mathrm{d}\Omega \qquad (3.17)$$

where M_{ij} and other non-linear terms are as follows

$$M_{ij} = \int_{\Omega} \varphi_j \varphi_i \, \mathrm{d}\Omega \qquad (3.18)$$

$$NL1x_{ij} = \int_{\Omega} \left(\sum_{j=1}^{N} f_j^{n+1} \varphi_j \right)^3 \frac{\partial \varphi_j}{\partial x} \frac{\partial \varphi_i}{\partial x} \, \mathrm{d}\Omega \qquad (3.19)$$

$$NL1y_{ij} = \int_{\Omega} \left(\sum_{j=1}^{N} f_j^{n+1} \varphi_j \right)^3 \frac{\partial \varphi_j}{\partial y} \frac{\partial \varphi_i}{\partial y} \, \mathrm{d}\Omega \qquad (3.20)$$

$$NL2x_{ij} = \int_{\Omega} \left(\sum_{j=1}^{N} f_j^{n+1} \varphi_j \right)^2 \frac{\partial h}{\partial x} \varphi_j \frac{\partial \varphi_i}{\partial x} \, \mathrm{d}\Omega \tag{3.21}$$

$$NL2y_{ij} = \int_{\Omega} \left(\sum_{j=1}^{N} f_j^{n+1} \varphi_j \right)^2 \frac{\partial h}{\partial y} \varphi_j \frac{\partial \varphi_i}{\partial y} \, \mathrm{d}\Omega \tag{3.22}$$

$$NL4_{ij} = \int_{\Omega} \left(\sum_{j=1}^{N} f_j^{n+1} \varphi_j \right)^2 \varphi_j \frac{\partial \varphi_i}{\partial x} \, \mathrm{d}\Omega \tag{3.23}$$

$$Bx_{ij} = \int_{\Omega} \frac{\partial \varphi_j}{\partial x} \frac{\partial \varphi_i}{\partial x} \, \mathrm{d}\Omega \tag{3.24}$$

$$By_{ij} = \int_{\Omega} \frac{\partial \varphi_j}{\partial y} \frac{\partial \varphi_i}{\partial y} \, \mathrm{d}\Omega \tag{3.25}$$

$$NL2_{ij} = \int_{\Omega} \left(\sum_{j=1}^{N} f_j^{n+1} \varphi_j \right)^{-4} \varphi_j \varphi_i \, \mathrm{d}\Omega \tag{3.26}$$

$$NL3_{ij} = \int_{\Omega} \left(\sum_{j=1}^{N} f_j^{n+1} \varphi_j \right)^{-3} \varphi_j \varphi_i \, \mathrm{d}\Omega \tag{3.27}$$

Now, we have a coupled system to be solved in the form of (3.28).

$$\underline{\underline{\boldsymbol{K}}}(\underline{u}) \, \underline{u} = \underline{R} \tag{3.28}$$

Here $\underline{\underline{\boldsymbol{K}}}$ is the stiffness matrix to be inverted to right side for evaluating unknown vector $\underline{u}$. However, $\underline{\underline{\boldsymbol{K}}}$ is already a function of unknown vector $\underline{u} = [f; \mathrm{P}]$ which makes the

problem non-linear. So, we need to find an approximate solution with a numerical technique. One of the techniques for the treatment of nonlinearity is Newton's method and we apply exactly this method for our FEM to treat nonlinearity by introducing a residual vector.

$$\underline{r}(\underline{u}) = \underline{\underline{\boldsymbol{K}}}(\underline{u})\,\underline{u} - \underline{R} \qquad (3.28.a)$$

We solve this relation for $\underline{u}$ to make residual zero. In order to do that we need to find the root of $\underline{r(u)}$. Newton's method is used to find this root. We apply the classical Newton's method to a vector function of a vector variable in which the tangent stiffness matrix is computed by equation (3.29).

$$\underline{\underline{\boldsymbol{T}}} = \frac{\partial \underline{r}(\underline{u})}{\partial \underline{u}} \qquad (3.29)$$

3.3 Mapping of the Derivative Terms

In §3.1, we show how to map two-dimensional Cartesian domain and in §3.2 we define the film thickness with related pressure terms in the natural coordinate system by these interpolation functions. One should notice that some of these terms contains derivatives with respect to local coordinates. Since the whole system is defined in the natural coordinates, we must transform *x* and *y* derivatives to *r* and *s* derivatives. To do that we use chain rule and solve the derivatives for relation below.

$$\begin{bmatrix} \frac{\partial}{\partial r} \\ \frac{\partial}{\partial s} \end{bmatrix} = \begin{bmatrix} \frac{\partial x}{\partial r} & \frac{\partial y}{\partial r} \\ \frac{\partial x}{\partial s} & \frac{\partial y}{\partial s} \end{bmatrix} \begin{bmatrix} \frac{\partial}{\partial x} \\ \frac{\partial}{\partial y} \end{bmatrix} \qquad (3.30)$$

In matrix notation, equation (3.30) is as follows.

$$\frac{\partial}{\partial r} = \boldsymbol{J}\frac{\partial}{\partial x} \tag{3.30.a}$$

where $\boldsymbol{J}$ is the Jacobian operator that relates the derivatives of local and natural coordinate systems. Relation above emphasizes unique analogy among these coordinate systems due to invertibility requirement of the Jacobian operator. For a unique nodal system, $\boldsymbol{J}$ is found by following relation.

$$\frac{\partial}{\partial x} = \boldsymbol{J}^{-1}\frac{\partial}{\partial r} \tag{3.30.b}$$

3.4 Symmetric Boundary Condition

Under normal circumstances, we enforce precursor film thickness at the edges of our domain via Dirichlet boundary condition. However, using a symmetry at *x* or *y* axis for various problems, such as spreading and sliding, saves a lot of computational time. This is introduced with Neumann boundary condition by assuming that the change of film thickness does not change along these axes due to symmetry property. Mathematically, it is represented for symmetry line around *y* axis (3.31) and symmetry line around *x* axis (3.32).

$$\frac{\partial f}{\partial x} = 0 \tag{3.31}$$

$$\frac{\partial f}{\partial y} = 0 \tag{3.32}$$

Now this raises an important question. How does it change our system? To show that let's get back to equation (3.1). Again, we start by multiplying our system with a test function, then integrate over the domain Ω and weaken the differentiability requirement. For clarity, we only focus on the following terms.

$$\int_{\Omega} \frac{\partial}{\partial x}\left(-f^3\, Bo \cos\alpha \frac{\partial f}{\partial x}\overline{f}\right) \mathrm{d}\Omega + \int_{\Omega} \frac{\partial}{\partial y}\left(-f^3\, Bo \cos\alpha \frac{\partial f}{\partial y}\overline{f}\right) \mathrm{d}\Omega \quad (3.1a)$$

We modify this term $(3.1a)$ as the divergence of gradient of droplet thickness so that we can use Divergence theorem to convert volume integral to surface integral.

$$\int_{\Omega} \nabla \cdot \left(-f^3\, Bo \cos\alpha\ \overline{f}\, \nabla f\right) \mathrm{d}\Omega \quad (3.33)$$

or simply

$$\int_{\Omega} -f^3\, Bo \cos\alpha\ \nabla^2 f\, \overline{f}\ \mathrm{d}\Omega. \quad (3.33.a)$$

Here, we rewrite $\nabla^2 f\, \overline{f}$ as follows.

$$\nabla^2 f\, \overline{f} = \left(\nabla \cdot \left(\overline{f}\, \nabla f\right) - \nabla \overline{f} \cdot \nabla f\right)$$

So that we have the following relation.

$$-\int_{\Omega} \nabla \cdot \left(\overline{f}\, \nabla f\right) f^3\, Bo \cos\alpha\ \mathrm{d}\Omega + \int_{\Omega} \left(\nabla \overline{f} \cdot \nabla f\right) f^3\, Bo \cos\alpha\ \mathrm{d}\Omega \quad (3.34)$$

Now we use Divergence theorem on the first term of (3.34) to convert the volume integral to the surface integral.

$$-\int_{\Omega} \nabla \cdot \left(\overline{f}\, \nabla f\right) f^3\, Bo \cos\alpha\ \mathrm{d}\Omega = -\int_{\partial\Omega} f^3\, Bo \cos\alpha \left(\overline{f}\, \nabla f\right) \cdot \underline{\boldsymbol{n}}\, \mathrm{d}\, \partial\Omega \quad (3.35)$$

We break-up the integral by the fact that we have both Dirichlet and Neumann boundary conditions.

$$-\int_{\partial\Omega} f^3\, Bo \cos\alpha \left(\overline{f}\,\nabla f\right)\cdot \underline{\boldsymbol{n}}\,\mathrm{d}\,\partial\Omega =$$

$$-\int_{\partial\Omega_1} f^3\, Bo \cos\alpha \left(\overline{f}\,\nabla f\right)\cdot \underline{\boldsymbol{n}}\,\mathrm{d}\,\partial\Omega - \int_{\partial\Omega_2} f^3\, Bo \cos\alpha \left(\overline{f}\,\nabla f\right)\cdot \underline{\boldsymbol{n}}\,\mathrm{d}\,\partial\Omega \quad (3.36)$$

Here, $\partial\Omega_1$ is the Dirichlet boundary condition and it is zero as we previously mentioned. Then we end up with following equation.

$$-\int_{\partial\Omega} f^3\, Bo \cos\alpha \left(\overline{f}\,\nabla f\right)\cdot \underline{\boldsymbol{n}}\,\mathrm{d}\,\partial\Omega = -\oint_{\partial\Omega_2} f^3\, Bo \cos\alpha\ \dot{\mathrm{N}}\, d\partial\Omega \quad (3.37)$$

where $\dot{\mathrm{N}} = \left(\overline{f}\,\nabla f\right)\cdot \underline{\boldsymbol{n}}$. Now we take normal vector $\boldsymbol{n} = i$ for *y* axis.

$$-\oint_{\partial\Omega_2} f^3\, Bo \cos\alpha\ \overline{f}\frac{\partial f}{\partial x}\,\mathrm{d}\partial\Omega \quad (3.37a)$$

Then $\boldsymbol{n} = j$ for *x* axis.

$$-\oint_{\partial\Omega_2} f^3\, Bo \cos\alpha\ \overline{f}\frac{\partial f}{\partial y}\,\mathrm{d}\partial\Omega \quad (3.37b)$$

Finally, we implement the boundary conditions (3.31) and (3.32) where Neumann states that there exists a symmetry along *x* and *y* axes. So, equation (3.37a) and (3.37b) are all become zero. Then we are left with only the second term of equation (3.34).

$$\int_{\Omega} \left(\nabla \overline{f} \cdot \nabla f\right) f^3 \, Bo \cos\alpha \; \mathrm{d}\Omega = \int_{\Omega} \left(\frac{\partial f}{\partial x}\frac{\partial \overline{f}}{\partial x} + \frac{\partial f}{\partial y}\frac{\partial \overline{f}}{\partial y}\right) f^3 \, Bo \cos\alpha \; \mathrm{d}\Omega \quad (3.38)$$

Which yields our original Dirichlet boundary condition. In brief, we do not need to change our previous weak formulation as long as the boundary nodes are defined properly. Whether analyzing quarter droplet spreading or sliding mechanism of a semi droplet, we just need to define the Dirichlet nodes (Figure 3.2).

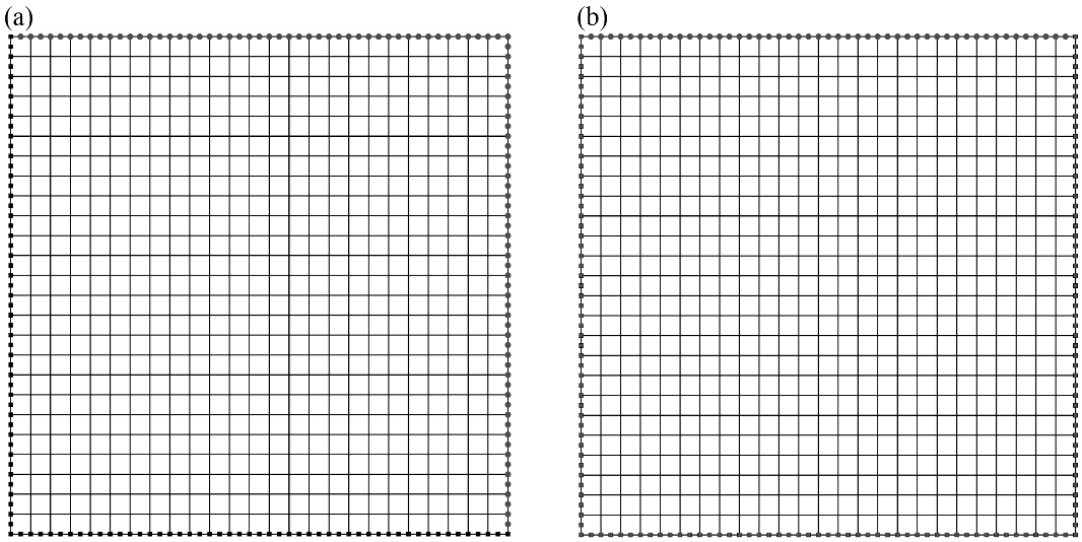

Figure 3.2: (●): Neumann boundary condition, (■): Dirichlet boundary condition, (a) Domain we use to solve spreading of a quarter droplet, (b) Domain we use to solve sliding problems where the north axis is the symmetry line

Chapter 4

Adaptive Mesh Refinement and Derefinement

Discretized partial differential equations can be solved in uniform grids and the values of unknowns at the grid points are estimated through the solutions of these equations. Yet grid size must be handled carefully to obtain for accurate results. For instance, precursor film thickness is a crucial parameter in modeling droplet dynamics which we are going to discuss its effect in Chapter 5. Studies in the literature often take f_0 as around %1 of characteristic thickness which is 0.01 [26,60,61]. However, higher values of f_0 leads to an inaccurate result [62] and special treatments like time scale corrections are needed to compensate this problem [25]. But as we decrease the precursor film, our system becomes stiff and it becomes harder to model molecular interactions at the contact line. Thus, higher resolution is required to model contact line. But this is computationally not feasible in three-dimensional problems even for values of f_0 around 10^{-3} . So, we decide to implement an adaptive mesh refinement method to focus our computation power around contact lines. By this way, we can work with smaller values of f_0 within a feasible computation scale.

There exist various types of AMR in the literature [63-68], but we only focus on nodal based quadratic quadrilateral finite elements [69]. Because, in our FEM solver data is stored at the vertex and edges of the element. In our previous study [32], we show that fine resolution is an obligation to get physically accurate results even in two-dimensional problems. To achieve such high resolution for three-dimensional problems in a uniform grid is not feasible and thus mesh refinement techniques are required. There are three basic type of refinement techniques which are p-type, r-type and h-type. Using a higher order shape function, quadratic or cubic instead of linear,

is the p-type mesh refinement technique. This method obviously increases the accuracy. However, for well-tried analysis of droplet spreading with quadratic elements, which will be mentioned in further sections, it is inadequate to maintain the shape of the droplet. Because pressure distribution at the contact line collapses due to weak resolution. Redistributing the existing node or r-type can be a solution to this problem at the contact line. But it still needs a fine resolution to begin with and thus generates finer resolution at the unused parts of the domain which results in longer computation times. Adding new nodes to our area of interest seems to be the most favorable choice in all three of them. Marking only the contact line and refining those specific regions allows us to concentrate our computational effort on the area where it is most needed, decreases memory storage and computation time over a uniform mesh for equal accuracy and gives complete control of grid resolution. Despite all these benefits, adaptive mesh refinement comes with its own disadvantages. Local mesh refinement creates level difference and this leads to a non-conformal interface (Figure 4.1).

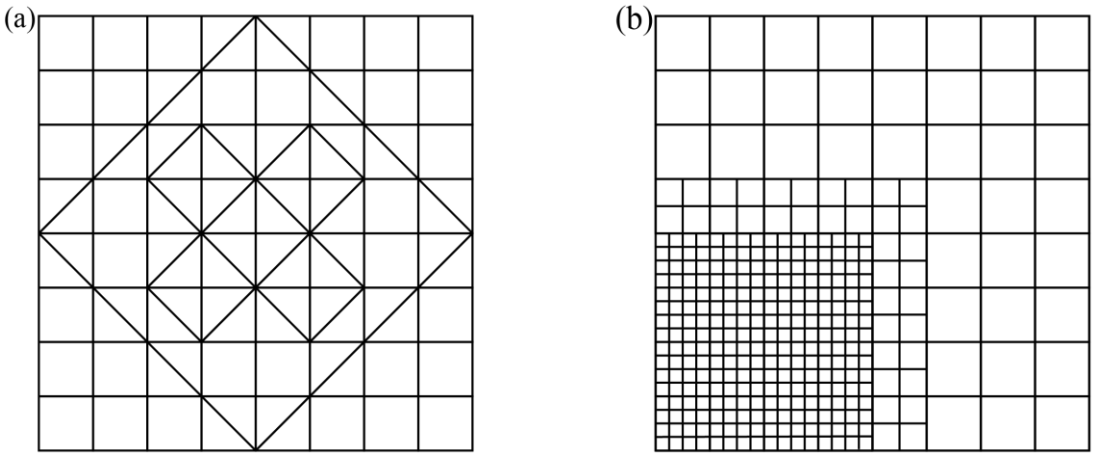

Figure 4.1: (a) Conformal mesh: all edges and vertices are connected; continuity is achieved in the domain. (b) Non-conformal mesh: there are non-intersecting edges at the level difference, discontinuous system

This poses an issue to continuity of our discrete functions. Another possible trouble with non-conformal mesh is the marking process. Elements to be refined can be marked with various approaches. However, decision of mesh size and smoothness of domain are key factors to obtain accurate results within a feasible time. Required treatments of these problems are discussed in this section.

4.1 Quadtree Data Structure

In brief, data structure is the systematic way of storing and organizing data. Tree is a data structure method to access and modify this data efficiently. For each newly generated elements, tree structure relates these children with their parents and contains other crucial information such as adjacent/neighboring elements, edges and level of the elements. Quadtree, a type of tree, is often used to subdivide a two-dimensional domain into four partitions or children in our case. In conventional quadtree structures, each parent and its children are constructed concurrently (Figure 4.2).

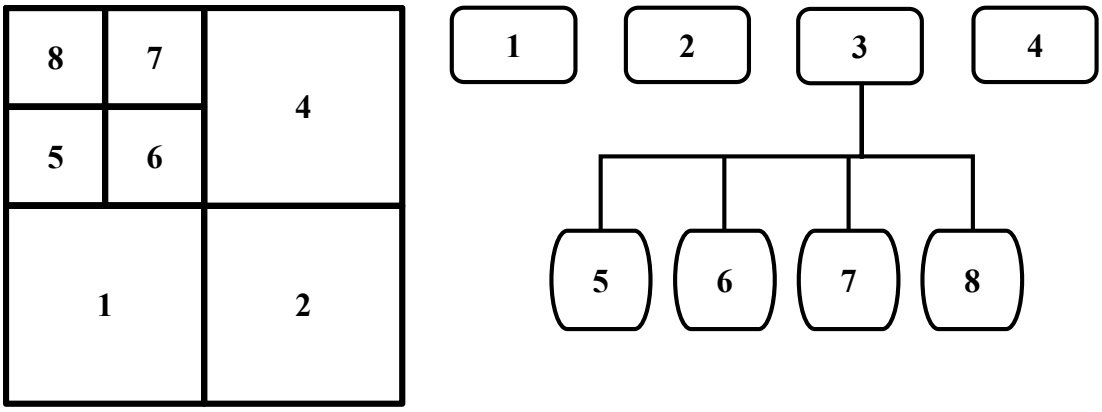

Figure 4.2: Conventional quadtree structure that relates parent and its children

From now on, every square with a number above will be called as element # where the number after hash symbol is going to indicate the corresponding number. Here, element #1-4 are called as ROOT which are on the coarsest level. Element #5-8 are newly generated elements and they are the children of element #3. Notice that the child numbers are in serial and their reference point is the latest element on the ROOT which is element #4. So, if we refine another element or one of the children, newly generated elements will be element #9-12. This continues until the finest level of the domain is achieved. Relation of children, parents and any other information are formed during the refinement, so it is a dynamic process. However, quadtree structure that we use in our code is quite different. We don't need to introduce or relate any information. Because we already constructed all necessary information beforehand. To show that Figure 4.3 is given below.

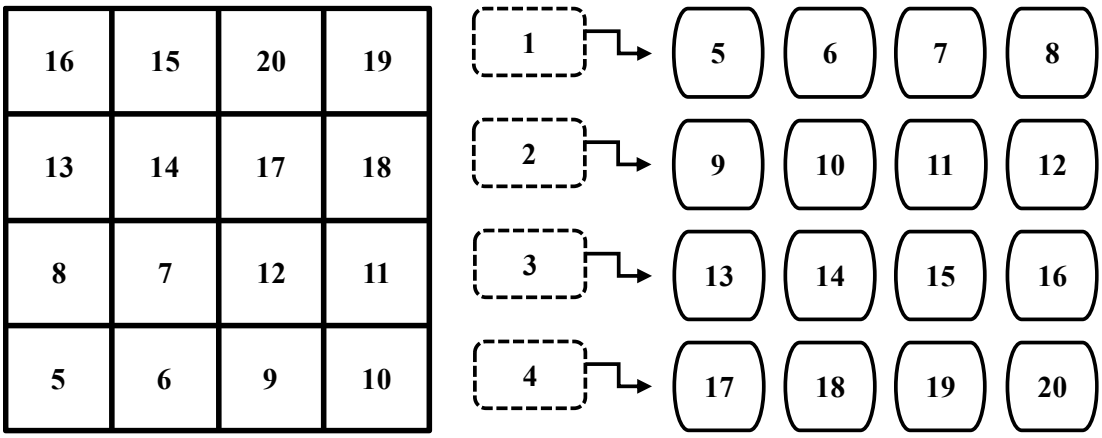

Figure 4.3: Prequad data structure. All data are constructed in advance

Apparent change from the previous structure is that this time every aspect of the domain including parents, children, neighboring elements and even possible hanging points at every level are constructed in advance, even though they are not present or refined in the domain. So, we have a static structure over a dynamic one which means that the order of refinement does not influence our data structure anymore. We call this structure as prequad data structure. However, this concept requires a new parameter we call as activity to distinguish existing and null elements. If an element is not yet present on the domain or it is a recently refined parent, this is a null or an inactive element. Otherwise, it is an exist or active element. To clarify the concept, let us examine previous example, Figure 4.4, with prequad structure.

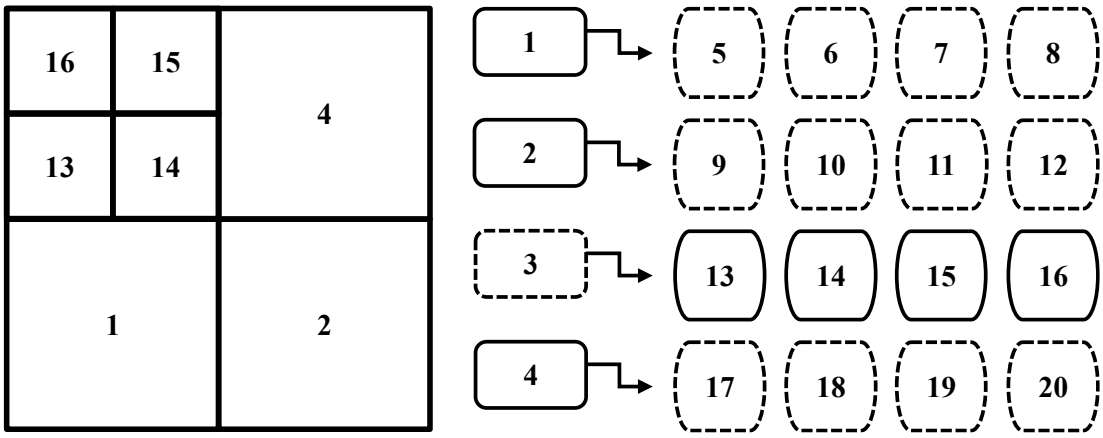

Figure 4.4: Same example with Figure 4.1 but with a quadtree data structure

Here, solid and dashed lines in the tree are active and inactive elements, respectively. We only use active elements in our FEM solver. In Figure 4.1 our children are element #5-8 due to dynamic structure. But here, they are element #13-16 and they cannot be

changed unless ROOT of the domain is modified. With this method, we don't need to add newly generated elements and their connected information into our quadtree structure since they are already present. What we must do is to activate recently refined children and inactive corresponding parents.

4.1.1 Consecutive Requirement

We construct our matrices and vectors in a consecutive manner. In the simplest form, row numbers of the connectivity matrix, matrix that contains node numbers of each element to satisfy uniqueness, corresponds to that element in the domain. When we define our domain priorly, we don't get consecutive but a higher element number and nodes. Let's compare previous examples. Children in conventional quadtree (Figure 4.1) are in order with the system by nature. But children of prequad system (Figure 4.4) and nodes are way bigger than our expectations and thus they must be put in an order (Figure 4.5).

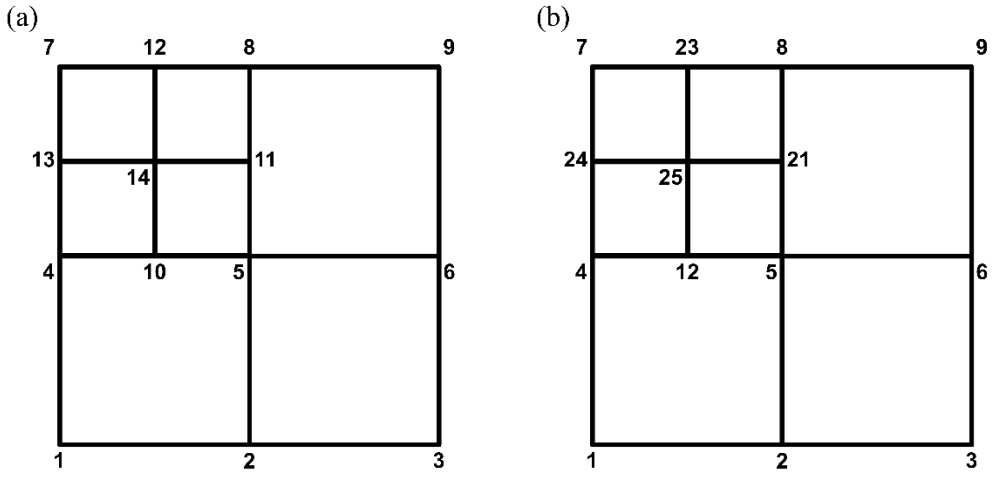

Figure 4.5: (a) Conventional data structure from Figure 4.2. Here nodes are in serial like their element number. (b) Prequad data structure from Figure 4.4. ROOT nodes are same but newly generated nodes are ordered in counterclockwise. Notice that nodes are defined such way that they are all unique

To modify prequad nodes in a consecutive order, we simply create a vector containing the unique node numbers of active elements and then we search this node numbers within the active elements again. Corresponding row number of unique vector is the consecutive adaption of our preload data. This is valid for every other information on the domain.

4.1.2 Hanging Points

In the finite element method, data is stored at the vertices of elements as nodes. Either linear or higher polynomial order, local refinement leads to a level difference and thus non-conformal mesh. Newly emerged nodes on these non-intersecting edges are referred as hanging points (as shown with ■ Figure 4.6) in the literature [69-71].

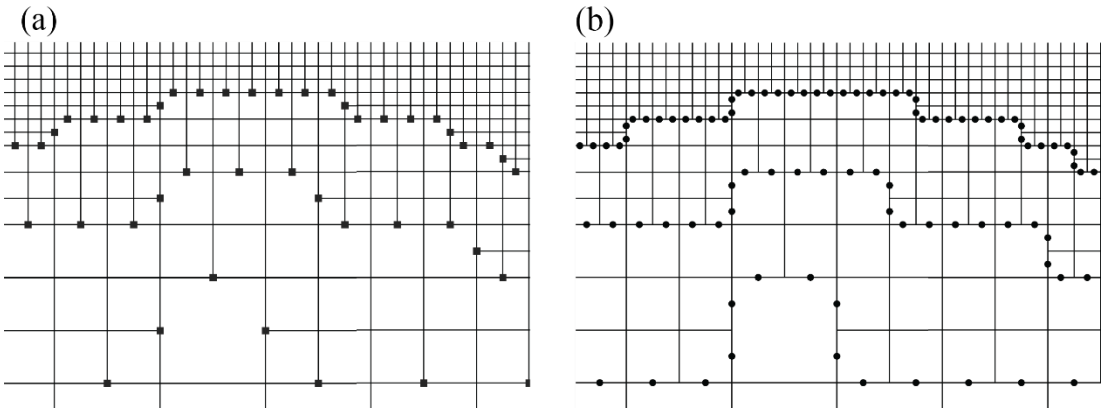

Figure 4.6: (a) Hanging points of linear elements, (b) Hanging points of quadratic elements at the non-intersecting edges

These new unknown nodes must be associated/interpolated into our system to maintain our continuous discrete functions. We store our hanging points in a matrix where rows represent the element number and columns are the walls of the element in counter clockwise direction. We check neighbors of the refined elements and since we know every information on the domain, thanks to our prequadtree structure, this is an easy procedure. Basically, if the neighboring element of newly refined element is active, their edges cannot be intersecting and thus there exist a hanging point at that wall. So, we check the location of non-intersecting edge by searching counterclockwise and find the hanging point at that wall, remember we also know node number of the hanging point due to prequadtree structure, and store it in our matrix. Then finally, we find the values of these hanging points by interpolating the estimated solutions from previous domain.

4.2 Element Marking Mechanism

In order to refine an element, we must mark it first. We demonstrate two ways to mark contact line which are geometry based and pressure based. Second one is the most versatile since droplet formation is susceptible to topography of the surface and sometimes it is hard to catch up these complex transitions with geometrical approach. Especially in the presence of liquid deposition to surface. Regardless, both are presented step by step.

4.2.1 Geometrical Marking

Geometric marking is a rather simple algorithm. We define the location of the contact lines. To clarify it, we are going to define the contact line with cardinal directions where droplet assumed to be sliding from left to right. So, west and east are receding and advancing contact line respectively. North and south are the lateral sides of the droplet. We find these locations as minx, maxx, miny and maxy being the contact lines at the west, east, south and north, respectively. Then we use ellipse equation to define lower limits of our marking.

$$\frac{(x-x_0)^2}{(maxx-minx)^2}+\frac{(y-y_0)^2}{(maxy-miny)^2}-1\leq 0 \qquad (4.1)$$

Equation (4.1) is dependent on the location of droplet. For instance, if our droplet is located at the symmetry axis of north wall, then maxy would be the length of *y*-axis which is L_y. Another example would be a spreading droplet. In this case, maxy and maxx are both length of the domain. We mark everywhere inside the ellipse with the mathematical expression in equation (4.1). To prevent unnecessary marking, we specify an upper limit constant (η) or we can use ellipse equation again, but this time with a different operator to restrain our marking areas and mark the elements in between upper and lower limits (Figure 4.7).

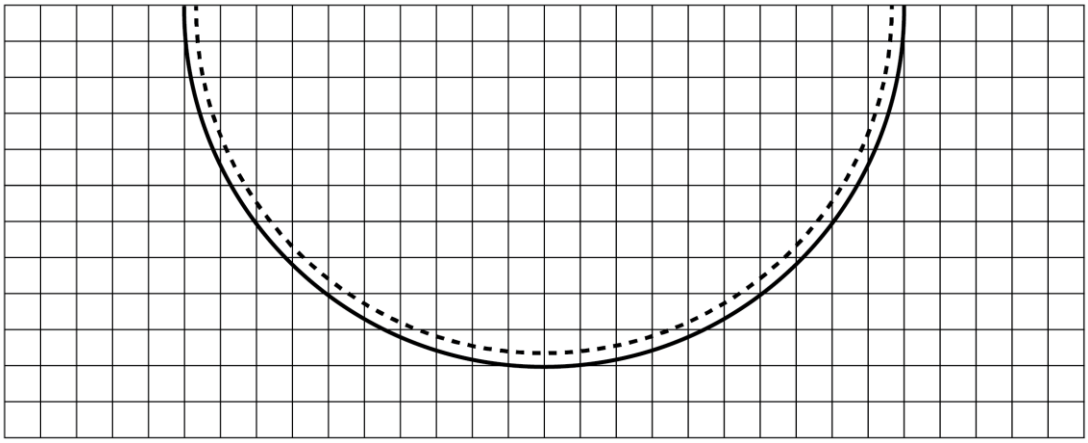

Figure 4.7: Geometrical marking of the contact line. $(--)$: Upper limit (η), $(-)$: Lower limit: in this case, it is ellipse equation

After the marking process, we use our quadtree structure to extend the marked line given in figure 4.7 by also taking adjacent neighbors into account. Then we activate and deactivate parent-child to refine our contact line. Derifenement is same for both methods, we regularly check location of maxx and minx and re-evaluate them and mark contact line. We check whether previously refined areas are marked again. If they are not marked, then we de-activate children and activate the parents.

4.2.2 Pressure Marking

This method is based on the disjoining model. Since we model the contact line by disjoining pressure, it gives us exactly the location of our contact line. So, we take the modulus of equation (2.14) to rule out the negative pressures at the contact line. Then, we put upper and lower limit by taking maximum and mean values of end up equation. This method differs from previous method in the sense of marking procedure. Here, we don't need to specify two separate boundaries as we do in geometrical marking. Because remaining values already give us the contact line (Figure 4.8).

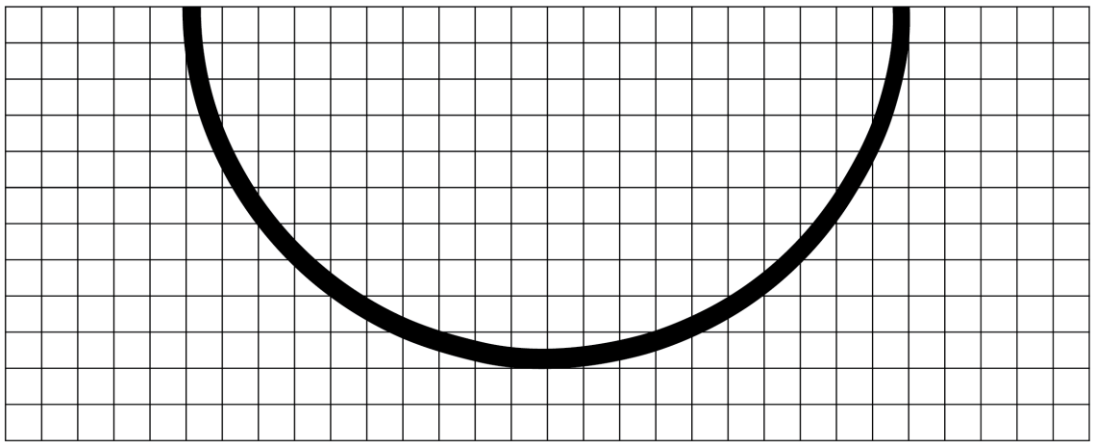

Figure 4.8: Contact line is marked with our disjoining pressure model. Upper and lower limits are decided by the pressure model. So, there is no need to specify additional parameter in this method

We believe this method is better than previous one since droplet dynamics can be affected with a slightest change on the domain. In some problems, droplet forms a pearl behind its tail and these small droplets might deceive the location of receding contact line that leads to unnecessary markings. Because of this, we use pressure marking method in our adaptive mesh refinement code. Just like the geometrical marking, we add neighbor elements after the contact line is marked for proper marking.

4.2.3 Mesh Balancing

If the level difference between adjacent elements after the refinement is one at maximum, then this mesh is balanced (Figure 4.9) otherwise, it is unbalanced (Figure 4.10).

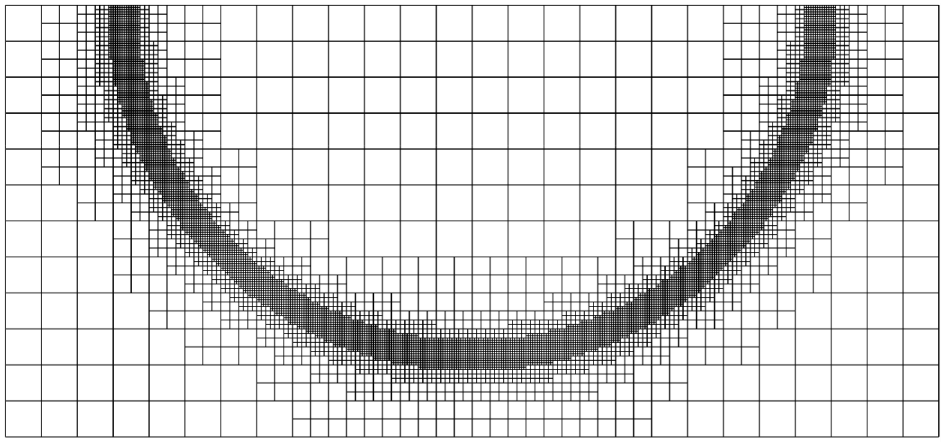

Figure 4.9: Balanced mesh: level difference is maximum one after the refinement

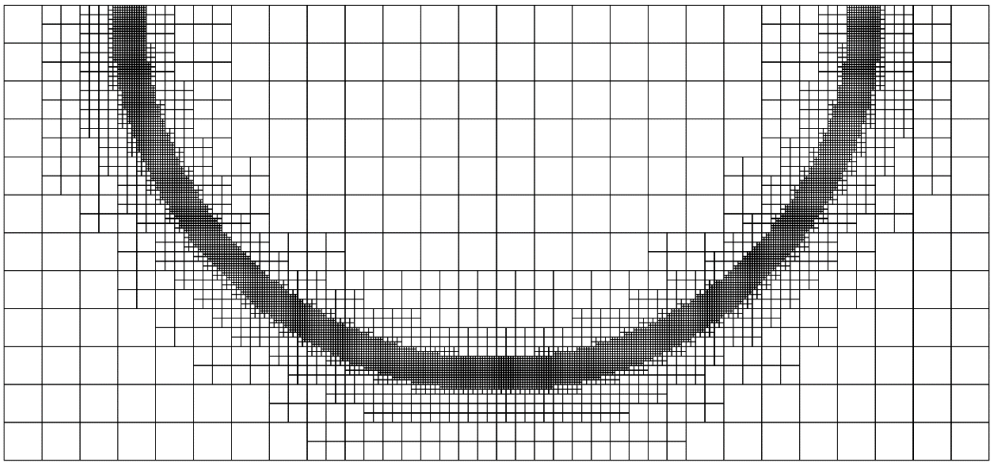

Figure 4.10: Unbalanced mesh structure: finest level is neighboring (level 4) the level 2 which means there exist 2 level difference. This is an undesired mesh structure

Local refinement of the contact line only is not sufficient to get accurate results. Balancing and distribution of the mesh, in other words the smooth transition of a mesh, is a key factor to get proper results. If these qualifications are not satisfied, then local errors become high which causes an issue in accuracy [72]. To overcome these problems, we propose the following solutions. After the refinement, we check activity of the refined elements, that are at least on first level, neighbors. If they are inactive, this means there exist a level difference higher than one. So, we de-activate this adjacent element parents and activate four children. We apply this procedure for all other refined elements that are not on ROOT. By this way, we balance our mesh. For the smooth distribution of mesh, we use neighbors again. Either geometric or pressure-based method, after marking the elements on contact line, we also take these elements neighbors for refining to achieve a proper distribution. This neighbor marking procedure is done by experimenting on the domain. We would like to emphasize that our preload data structure makes all these processes easier since we know everything about the domain. After these modifications, a proper mesh structure should look like in Figure 4.11.

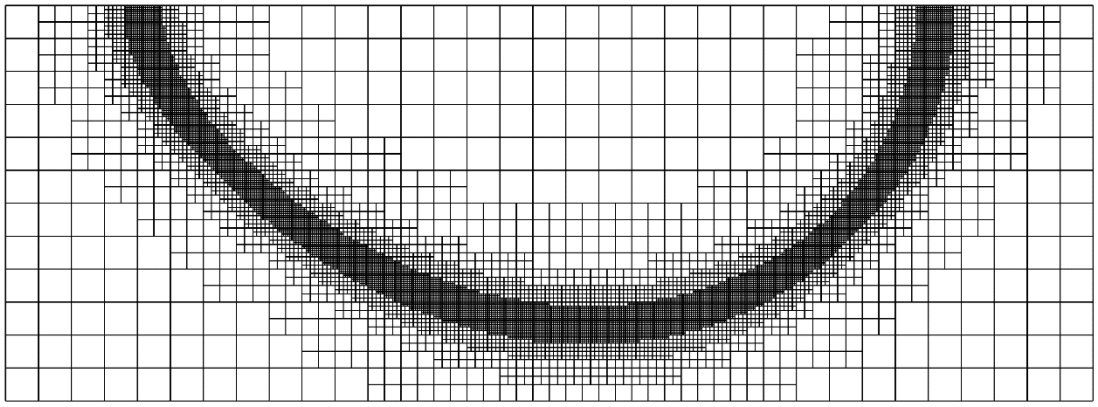

Figure 4.11: Proper mesh structure: balanced and smooth transition

Finally, we would like to show how much we save computationally by using adaptive mesh refinement. In Table 4.1, we present the number of nodes of an equal resolution system to analyze sliding droplet on a flat surface for uniform, three times refined and four times refined domain.

Table 4.1: Number of total nodes to analyze same problem for equal resolution. Length on the *y*-axis is constant and same for all cases, $L_y = 1.2$

L_x	Uniform	Level 3	Level 4
3	369985	76707	62533
3.5	431585	77927	62843
4	493185	79147	63153
4.5	554785	80367	63463
5	616385	81587	63773
5.5	677985	82807	64083
6	739585	84027	64393
6.5	801185	85247	64703
7	862785	86467	65013
7.5	924385	87687	65323
8	985985	88907	65633

As expected, to achieve same resolution in uniform domain, we require immense number of nodes. Even in this rather simple problem, we must use long distances along

x-axis, maybe between 10 and 15 to investigate cusp and pearling formations. But at $L_x = 8$, around a million number of nodes is needed to obtain accurate results in uniform domain. This is not computationally feasible for an unsteady problem and thus adaptive mesh refinement is needed. To compare the level3 and level4 cases, figure 4.12 is given.

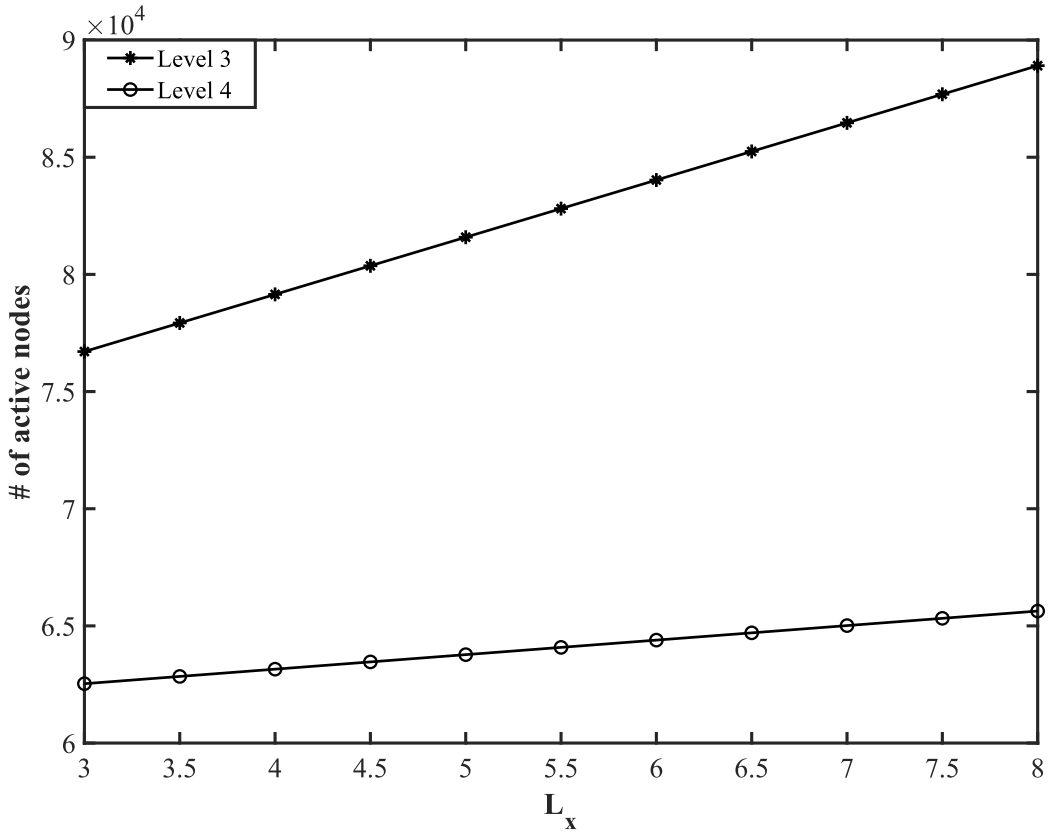

Figure 4.12: Comparison of level3 and level4 refinement for same resolution

As length of the domain increases, number of active nodes are increasing linearly. However, to get same resolution in level3 as level4, ROOT of the domain also needs to be finer. Thus, we refine our elements until level4 in our solver.

Chapter 5

Motion of Droplets Over Homogenous Substrates: Validation

In this chapter, we validate our solver for various problems. In §5.1, we check mesh independency. In §5.2, we place a droplet on a flat and horizontal substrate and let it spread to its equilibrium angle for different precursor film thicknesses to study the effect of f_0. Then, we use equilibrium angles in between $20°$ to $45°$ for same precursor film thickness to check the effect of equilibrium angle on our assumption from lubrication equation. In §5.3, we study the same problem, but this time, we set the equilibrium angle to zero and let it spread up to the non-dimensional time 100. Then we check the change of maximum height of droplet with respect to time to be able to compare with the scaling law of Tanner[73]. Finally, in §5.4, we investigate a sliding droplet on a flat substrate with a various inclination angle. The physical property of the droplet is chosen from the study of Podgorski[49]. Our results are compared with the numerical study of Ahmed[61] and Kumar[26]. Linear relation between cube of advancing contact angle and capillary number known as Cox-Voinov law is established from this analysis.

5.1 Mesh Independence

Before we begin to any other validation sections, we must first show that our results are independent of our mesh. To do that, we examine 2 problems. In first one, we place a droplet on flat horizontal substrate and set equilibrium angle as $20°$. Then we let it spread until it reaches its static angle. We measure these angles and tabulate them in Table 5.1 for various number of elements (N).

Table 5.1: Change of the equilibrium angle with total number of elements N at ROOT

N	θ_e
$20x20$	19.3314
$25x25$	19.3671
$30x30$	19.3716
$35x35$	19.3754
$40x40$	19.3783

Here, we should note that the total numbers in table 5.1 are the coarsest level. So, if we have a domain with a length of 2 in both axes, we have the grid size of $3.125x10^{-3}$. Because we are using adaptive mesh refinement that refines the domain four times. In our prequad structure, we have actually $640x640$ of total elements. From results we can say that for increasing number of elements, change in the computed equilibrium angle vanishes.

As a second problem, we place the droplet on flat inclined substrate and examine the location of the contact lines at same times for four different mesh. For this problem we use same precursor film thickness and Bond number which are $f_0 = 0.0075$ and $Bo = 1.1$. The results are shown in figure 5.1.

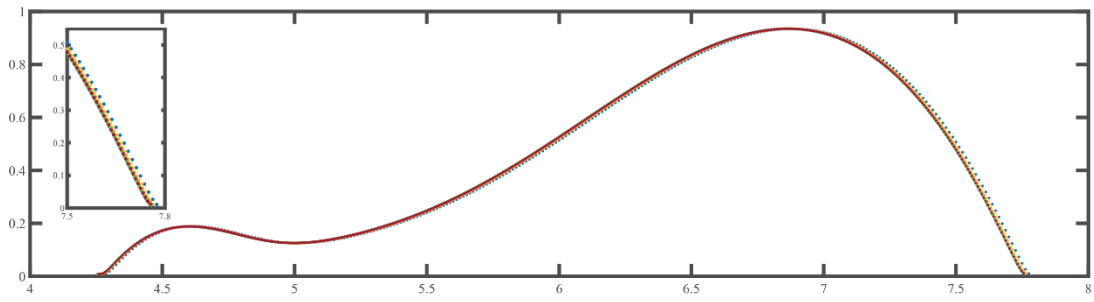

Figure 5.1: Location of contact lines where $L_x = 20$ and $L_y = 1.2$ for time $t = 7.0$. Dark blue: $50x3$, Yellow: $100x6$, Red: $125x8$, Green: $150x9$

For all meshes, the element size is same and square. For instance, dark blue mesh has a element size of $d_x = 0.4$ and $d_y = 0.4$ at the ROOT. It is clear from the figure 5.1 that our mesh does not have an effect for grid size smaller than 0.16 which is a mesh finer than $125x8$. So, from both of these experiments, we decide our optimal grid size as $d_x = 0.1$ and $d_y = 0.1$ at the ROOT.

5.2 Equilibrium Angle

5.2.1 Effect of Precursor Film Thickness

This part is necessary to check whether we really ensure the equilibrium angle that we impose to our droplet. Because static angle directly affects the contact angle hysteresis which is the key factor of our study. It is observed that the physics are deteriorating for higher values of f_0[62]. However, small precursor film creates a stiff structure to solve and thus requires high computational power. So, our aim is to approach to equilibrium angle as much as possible within a feasible scale. To do that we place a droplet at *x* and *y* symmetry axis (Figure 3.2.a) with an equilibrium angle of $20°$ on a flat and horizontal substrate and let it spread until it reaches an equilibrium. For different values of f_0, we measure the contact line and decide the optimal precursor film thickness for our solver. Results are shown in figure 5.2 and Table 5.2.

Table 5.2: Equilibrium angles for decreasing precursor film thickness

f_0	θ_e
0.03	16.3771
0.02	17.3993
0.01	18.6282
0.0075	18.7883
0.005	19.0536
0.003	19.2689
0.002	19.3817
0.0015	19.4382
0.001	19.4971
0.00075	19.5136
0.0005	19.5536

From table 5.2, it is clear that the computed angle converges to a certain angle that is around 19.5° for decreasing f_0. Film thicknesses smaller than 0.005 are within an acceptable error number which is 1% deviation from the original imposed angle. So, we are safe to use any of these f_0 lower than 0.005.

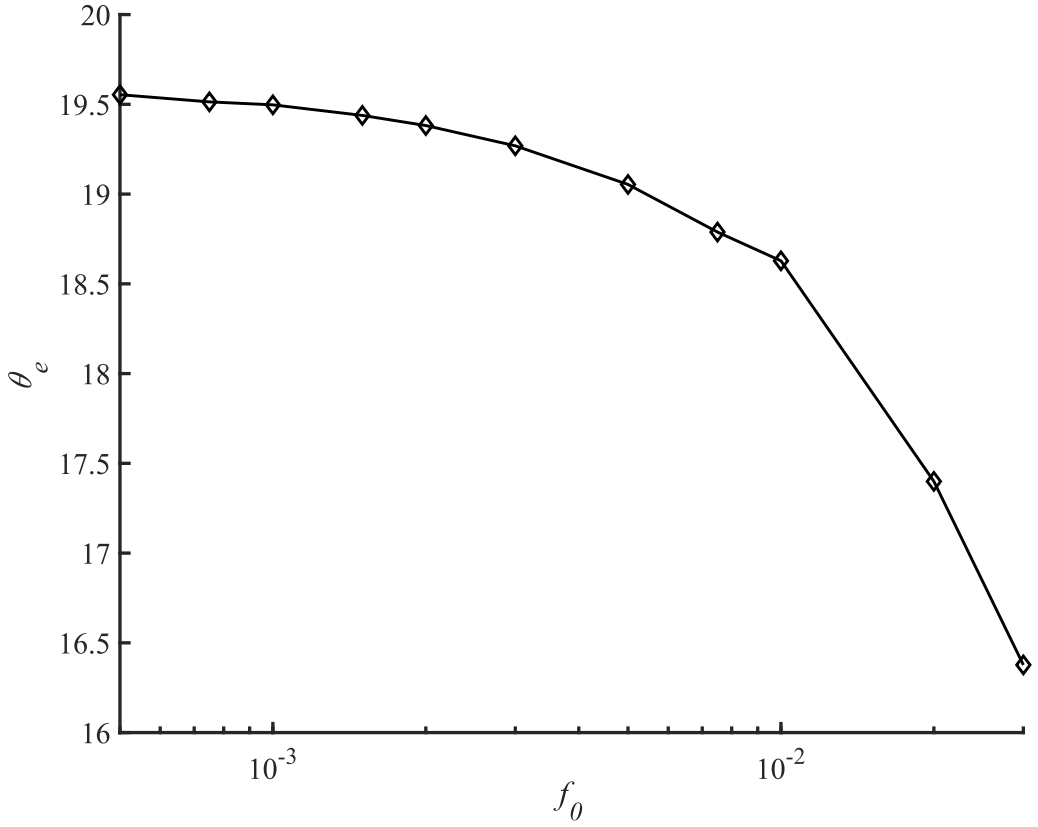

Figure 5.2: Computed equilibrium angle for decreasing precursor film thickness. As we decrease the f_0, we approach equilibrium angle

We should also emphasize that droplet cannot restrain its shape properly and slowly diffuses through the domain for film thickness higher than 0.03 which is expected because the length of the transition from the static region to flat precursor film region gets larger. But as we decrease the precursor film below 0.003, the transition from precursor film to contact line becomes sharper which requires higher resolution. This transition is given in figure 5.3.

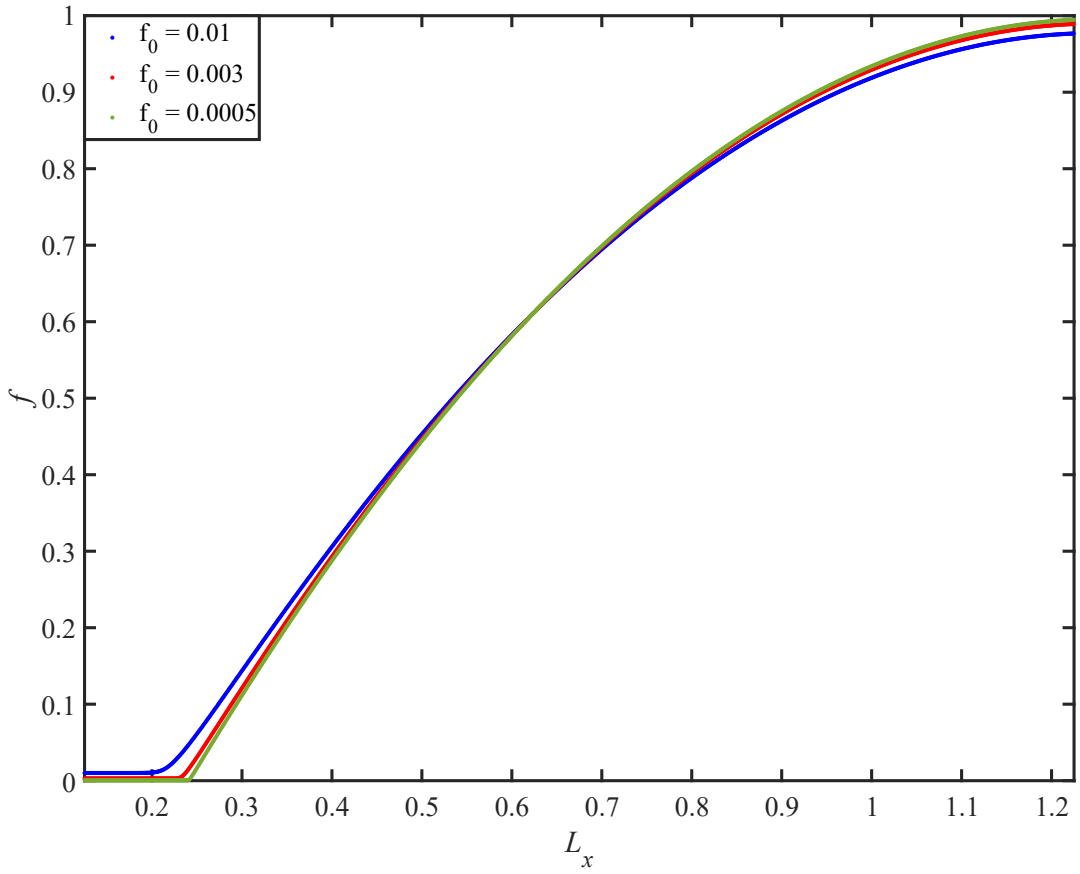

Figure 5.3: Location of transition from precursor film thickness to droplet thickness for 3 different f_0 along *x*-axis at the symmetry line

From figure 5.3 we can see the sharp transition in $f_0 = 0.003$ and $f_0 = 0.0005$ while $f_0 = 0.01$ is more like diffusing from droplet to precursor film. This sharp transition however returns us as a stiff structure that requires higher computation power. For this simple analysis, our grid size is $1.95x10^{-3}$ where the length of the domain is 1.25 for both *x* and *y* axis. Reaching this resolution for higher length domains such as $L_x = 10$ or $L_x = 20$ is not computationally feasible for us. Thus, with all these information above, we decided our optimal precursor film thickness to be 0.0025 in our solver.

5.2.2 Effect of Equilibrium Angle

We've explained the details of lubrication theory where we assume flow to be thin and long such that $\varepsilon \ll 1$ or $\frac{(1-\cos\theta_e)}{\sin\theta_e} \ll 1$. But we might not satisfy this assumption while analyzing droplets with high equilibrium angles. To check this effect, we again investigate the same problem in §5.1.1. This time we use same precursor film

thickness, but we change the static angle of our droplets. Our analysis is conducted for 3 different equilibrium angles which are $20°$, $30°$ and $45°$, respectively. Results are given in Table 5.3.

Table 5.3: Relative errors between measured and expected equilibrium angles for various film thicknesses

f_0	Expected θ_e	Measured θ_e	Relative Error %
0.01	45	39.0114	13.308
0.01	30	27.1946	9.351
0.01	20	18.6282	6.859
0.005	45	40.0291	11.046
0.005	30	27.9555	6.815
0.005	20	19.0536	4.732
0.0025	45	40.5558	9.876
0.0025	30	28.3451	5.516
0.0025	20	19.3502	3.249

As expected, we lost accuracy for droplets with higher equilibrium angle. This is because our thin-long flow assumption loses its validity. We show this in table 5.4 below. Notice that for higher film thickness, e.g., $f_0 = 0.01$, relative error increases drastically which agrees with our results from Table 5.2.

Table 5.4: Thin flow assumption for different equilibrium angles

θ_e	ε
10	0.0875
20	0.1763
30	0.2679
45	0.4142
55	0.5206

For higher equilibrium angles, we are getting closer to unity which does not satisfy our thin-film assumption. However, there exist studies in the literature that uses equilibrium angle of 45°[61] and even higher like 57°[54]. So, to use higher equilibrium angles in analysis, precursor film thickness must be minimized for decent results. In our case, we mostly set equilibrium angle to 30°. Another important feature is the effect of bond number on the equilibrium angle. For horizontal substrates, $\alpha = 0$, even though $Bo \sin \alpha$ is nullified, bond number effects the spreading of our droplet. Simply, for increasing Bond numbers, measured equilibrium angle decreases.

5.3 Tanner's Law

Experimental study conducted by Tanner[73] on spreading of silicone oil drops on horizontal substrate shows that the maximum height of the droplet is proportional to time and it scales with a power law known as Tanner's law. For three-dimensional problems this scaling is $t^{-0.2}$. To examine this, we place a droplet on a flat and horizontal substrate and let it spread until the time is 100. For this specific problem, we assume the droplet to be completely wetting the surface ($\theta_e = 0$) for proper investigation of this physical aspect and initiate its motion by setting the initial contact angle to 20°.

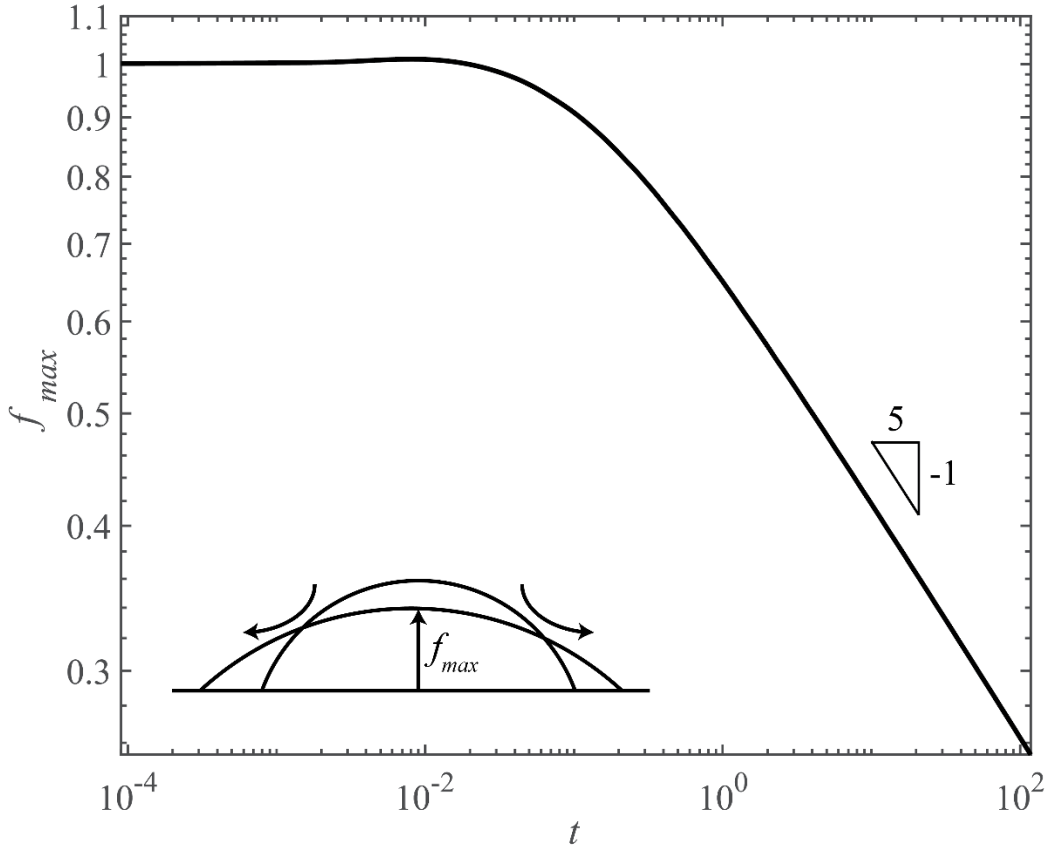

Figure 5.4: Change of central droplet height (f_{max}) with respect to time t

For $1 < t < 100$, we estimate the slope of the line in the figure 5.4 and we find that it is -0.2. This shows that our results agree with the Tanner's power law. We would like to make some remarks for the data $t < 1$. We initialize the droplet as spherical cap by assuming its sufficiently small. However, even though this is a valid assumption, the real shape of a droplet is different from a spherical cap, especially around the transition region from macroscopic region to precursor film. Thus, during this period, it is trying to obtain its original shape. This is observed in our previous study[32] and other studies as well. So, this is completely normal and acceptable.

5.4 Droplet Sliding Over Inclined Flat Substrates

Podgorski [49] states in his experimental study there exist three regimes for a sliding droplet over an inclined substrate, and they are all related to certain critical inclination angle. For smaller inclination angles, droplet reach to a terminal speed and takes an oval shape throughout the whole sliding process. This terminal speed is proportional to inclination angle and if we increase this angle to its first critical value, droplet

changes form and develops a corner at the receding contact line that is resembling to a teardrop shape. As we continue to increase tilt angle to second critical value, receding contact angle vanishes until it reaches to an effective capillary pressure and forms a neck. This neck later breaks into a smaller droplets which are referred as pearling [48,49,74]. To see whether we get the same physics, we place a droplet on a flat substrate inclined at an angle α. We increase gradually the inclination angle to adjust $Bo \sin\alpha$ and analyze its effect on the droplet speed and formation (Figure 5.5). The physical property of the droplet is taken from Podgorski [49] and our numerical results are compared with other two studies which are Kumar et al. [54] and Ahmed[61] for the same problem. Droplet is 47V10 silicon oil with a surface tension of $\gamma = 20.5x10^{-3}$ N/m, viscosity $\mu = 9.15x10^{-3}$ Pa.s, density $\rho = 924$ kg/m^3 and volume of $\mathcal{V} = 18$ µL.

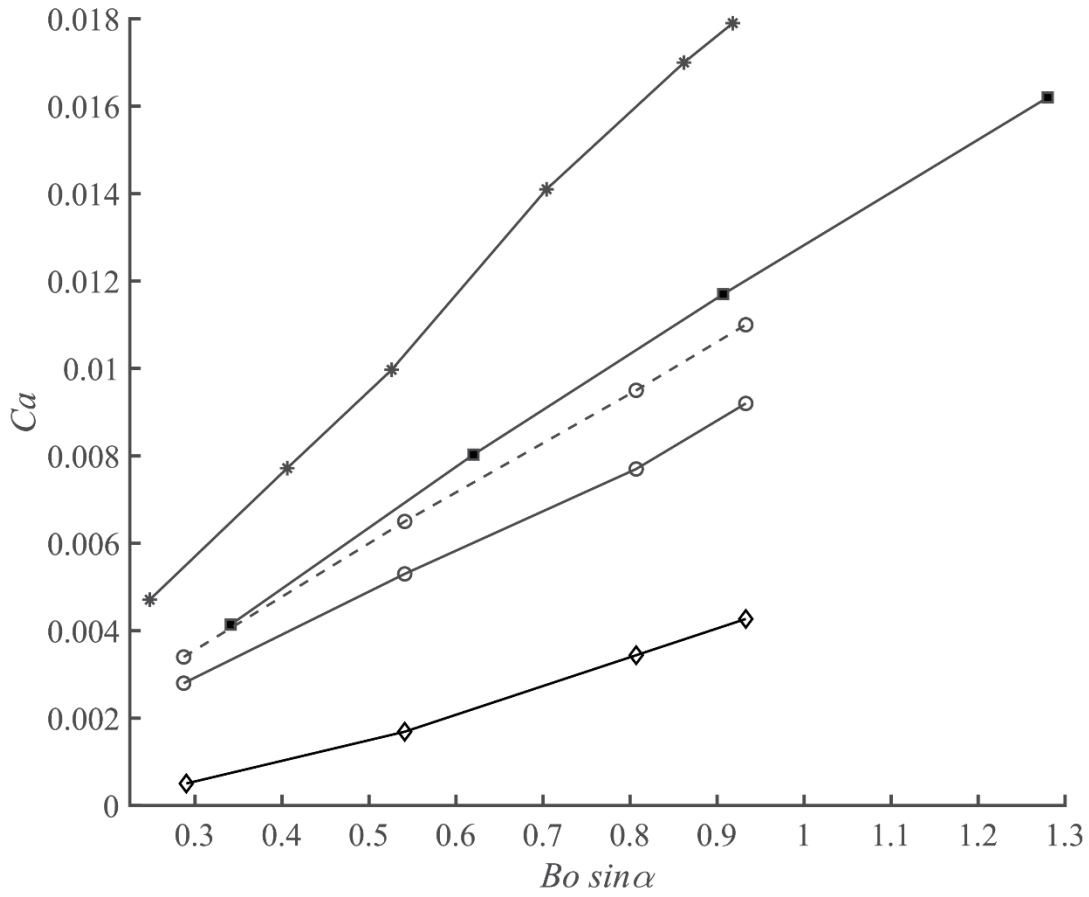

Figure 5.5: Change of capillary number for different inclination angels. $(-*)$: Kumar [54] for $\theta_e = 45°$ and $f_0 = 0.005$, $(-\blacksquare)$: Ahmed [61] for $\theta_e = 45°$ and $f_0 = 0.01$, $(--o)$: Our results for $\theta_e = 45°$ and $f_0 = 0.01$, $(-o)$: Our results for $\theta_e = 45°$ and $f_0 = 0.0025$, $(-\diamond)$: Experimental data of Podgorski [49]

For two different f_0, we change the α and analyze the droplet sliding. As we can see from the figure 5.5, our results show similar physics with experimental and other two theoretical studies. For increasing α, terminal speed and thus capillary number is increasing. The shape of the droplet is oval for all cases because we don't pass the first critical threshold of $Bo \sin \alpha$. Another important feature is that the advancing contact angle is directly proportional to capillary number while receding contact angle is reciprocally proportional. This relation is also observed in Le Grand's study [74] as well. Thus, we conclude that our results are physically accurate. To see droplet formations such as cusps and pearls, we conduct three different runs with required information from Podgorski's study again. Results are shown in figure 5.6 and figure 5.7.

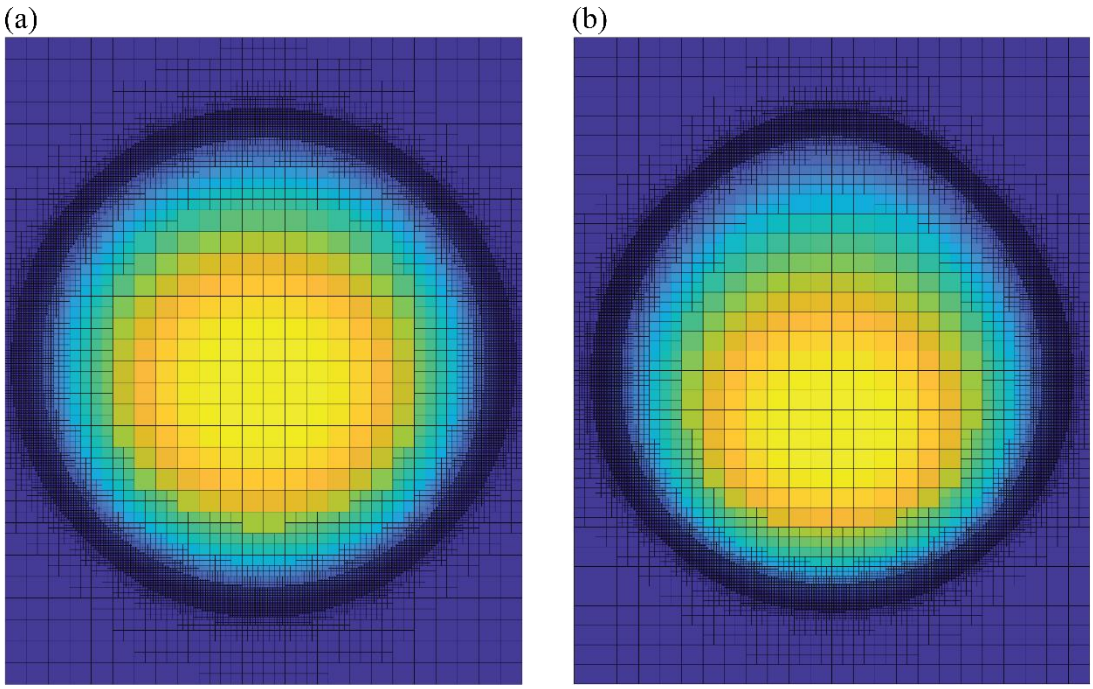

Figure 5.6: Aerial view of sliding droplets with different tilt angles. (a) Tilt angle is so small that droplet takes circular shape, (b) First critical tilt angle is passed, droplet begins forming a corner. Change in the mass center of droplet can be seen from yellow contour

Here, both droplets are at their terminal speeds so that their shape does not change anymore. Droplet at figure 5.6(b) passes the first critical threshold and forms a corner. Further increment leads to pearling formation as shown in figure 5.7 below.

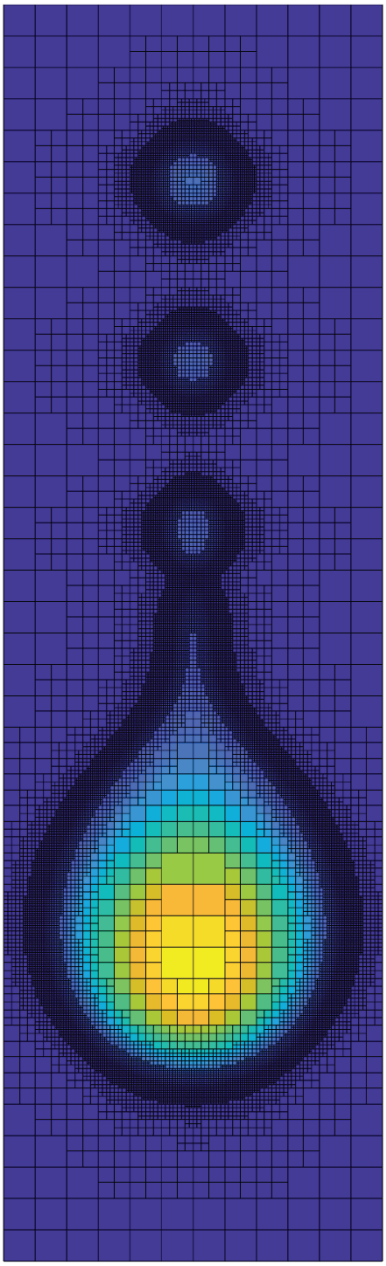

Figure 5.7: Aerial view of sliding droplet with pearls behind

As expected, after second critical angle is passed, receding contact line of the droplet vanishes but static angle never gets zero which is consistent with Snoeijer[48]. Then it creates a neck and deposits residual droplets after a while. The main droplet resembles to characteristic tear drop shape.

5.4.1 Cox-Voinov Law

In this section, we examine the consistency of the change in advancing and receding contact angle. The cube of dynamic angle must be linearly proportional to capillary number. It is given by the Cox-Voinov Law[52,75]

$$\theta_{A,R}^3 - \theta_e^3 = \pm 9 \ln \frac{x}{\ell_{micro}} \, Ca. \tag{5.1}$$

In equation (5.1), ℓ_{micro} is the microscopic length-scale. To show that, we use our previous data from the Podgroski and find the relation between contact angles and capillary as follows (Figure 5.8).

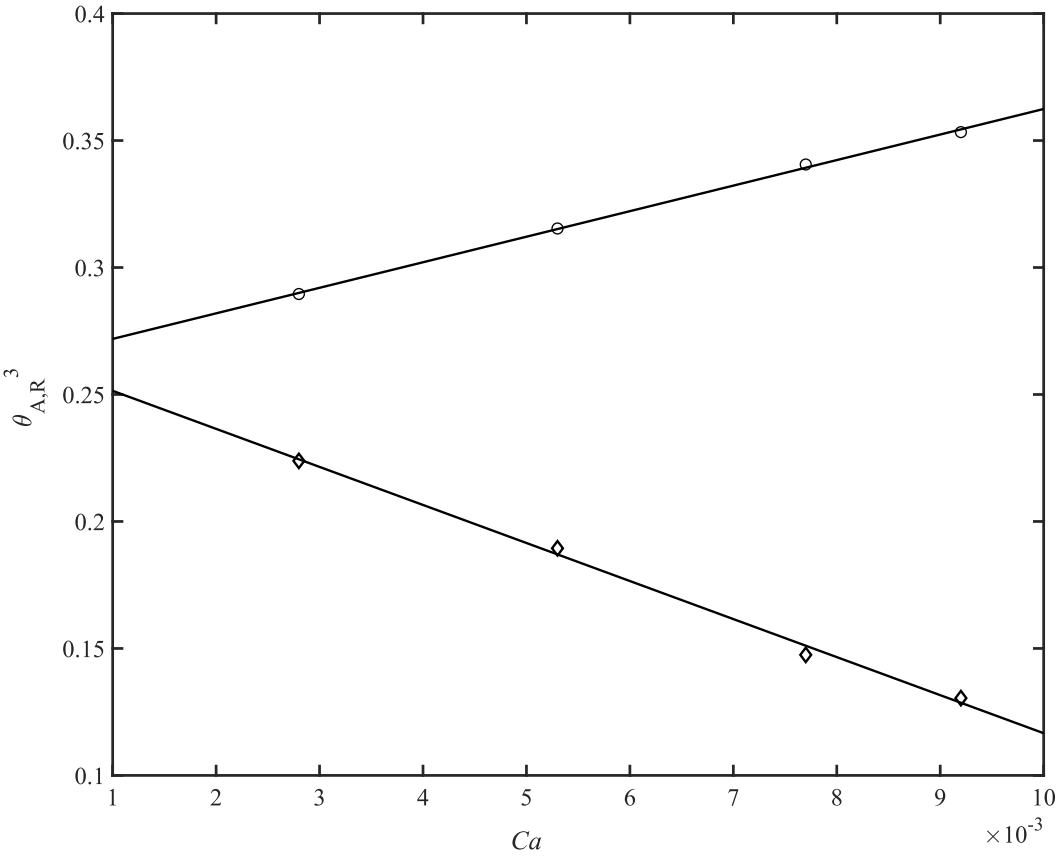

Figure 5.8: $(-o)$: Ca vs θ_A^3 , $(- \diamond)$: Ca vs θ_R^3 from Cox-Voinov

We fit our data into a line in figure 5.8 and it represents linear relation that satisfies Cox-Voinov law. This relation is also mentioned in Le Grand's study[74] as well.

In final words, we've discussed the effect of equilibrium angle to our results and confirm that we are measuring proper angles for decided precursor film thickness. Maximum height of the spreading droplet is related with time that satisfies Tanner's law. Linear relation between the cube of advancing, receding contact angles and Capillary number is achieved from Cox-Voinov model. Change of Capillary number with respect to $Bo \sin \alpha$ for different tilt angles is demonstrated. Finally, for three different tilt angles we examine different droplet formations where we pass critical threshold in two cases. In the lowest α, droplet takes circular shape. After first critical tilt angle, droplet speeds up and forms a corner. In final case, tilt angle is so high that droplet forms pearls at the receding contact line. From all these examinations, we conclude that our finite element solver can accurately capture the physics of slender droplet motion over substrates.

Chapter 6

Effect of Surface Topography on Pearling

Sliding droplet on an inclined substrate takes many formations depending on their capillary and bond numbers [74]. As droplet slides on the substrate, surface tension forces pull the droplet to opposite side of sliding whilst gravitational forces assist the sliding motion and this force balance creates the contact angle hysteresis. For some droplets receding contact angle vanishes with this force balance such that gravitational forces become insignificant and viscous flow at the receding contact line solely depends on the gradient of capillary pressure [48]. For high Bond numbers, this contact angle forms a sharp corner and eventually deposits pearls on to substrate. These physical features can be expedited with surface heterogeneities while the motion of droplets is delayed. Oliver [76] shows this delay on sharp-edged crystalline steps where he observes the contact line motion of a spreading droplet on such rough surfaces. He states that surface roughness significantly retards the contact line motion. Based on this, studies are conducted to delay contact line motion by either using chemically heterogeneous substrates or introducing an external force. For instance, Yong [77] observe droplet entrapment for a hydrophobic surface with hydrophilic cavities where Liang [78] uses Lamb waves and excites the surface to trap pearls onto the surface. To analyze this process, we use chemically homogeneous substrate with only gravity as a driving force. We delay the contact line motion and trap the residual droplets with a surface roughness only. This surface roughness is introduced with a basic sinusoidal function given in equation (2.1) to focus on certain parameter effects such as slope and cell frequency. For varying amplitudes and frequencies, we try to understand the mechanism of droplet entrapment. We construct sinusoidal wave grooves to be parallel with the motion of contact line based on Cox's study [79]. Cox

proves that orientation of sinusoidal wave changes the dynamics where grooves that are parallel to motion of contact line effectively decelerates the motion of contact line.

Rest of the chapter is as follows. In §6.1, we begin with a single sinusoidal cell of various configurations to investigate the effect of slope on droplet deposition. Then we gradually increase the number of cells to maximum three for fixed slope in order to examine the effect of topography frequency. In §6.2, we extend the analysis for the motion of droplet on full sinusoidal substrates.

6.1 Factors that Effect Droplet Deposition

Before we begin with fully sinusoidal domain, we would like to investigate the effect of slope on residual droplet formation and droplet entrapment. Thus, we analyze a droplet having following parameters $Bo = 1.1$, $f_0 = 0.0025$, $\theta_e = 30°$ and $\alpha = 90°$ on a substrate with a single sinusoidal cell. Slope of the topography is adjusted by the amplitude ($Å$) in equation (2.1). We use three different amplitudes which are $Å = 0.05$, $Å = 0.075$ and $Å = 0.1$ with fixed wavelength $\lambda = 0.75$. Initial droplet has a non-dimensional volume of 1.6082. Figure 6.1 shows the droplet profiles in *x*-*z* plane at non-dimensional times 6.99, 7.76 and 8.23, the coordinate system is same as we show in figure 2.1.

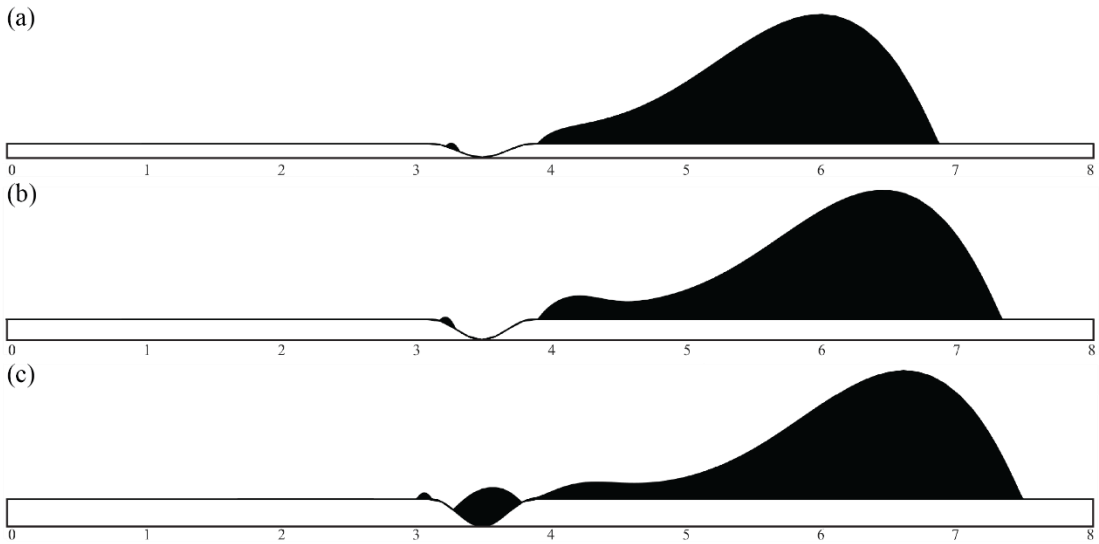

Figure 6.1: Residual droplet deposition for (a) $Å = 0.05$, (b) $Å = 0.075$, (c) $Å = 0.1$

For three different cases, we examine droplet formation after it depins itself from the sinusoidal groove. In all three cases, the steepest topography, $\text{Å} = 0.1$, is the only one that can properly trap a droplet. We measure the non-dimensional volume of this trapped droplet as 0.0312, which is nearly %2 of our initial droplet. As Å increases, droplet profile changes where receding contact line of droplet sliding on a higher amplitude cell tends to elongate more after it depins. We also examine delay in the motion with increasing slope. Non-dimensional times are 6.99, 7.76 and 8.23 for Figure 6.1(a), Figure 6.1(b) and Figure 6.1(c), respectively. At the same time, droplet on the least steep slides faster than other two droplets. Interestingly, in all cases we observe a small residual droplet compared to the trapped droplet, around %0.02 of initial droplet volume, that either pins or slowly slides into our cell. We believe this can be explained with Snoeijer's and Cox's statements. When our main droplet slides into cell, location of maximum advancing contact angle is achieved at the highest absolute slope of the topography[79]. There droplet pins to substrate for a while and spreads across the groove until it depins. After depinning, receding contact line of the droplet enters the cell. As droplet continues to slide away from the cell, lateral contact line propagates parallel to groove orientation whilst receding contact line creates a transverse curvature[48]. In this period, capillary pressure tries to maintain the shape of receding contact line as contact angle decreases and begins to form a sharp corner that later turns into a tail (See Figure 6.2).

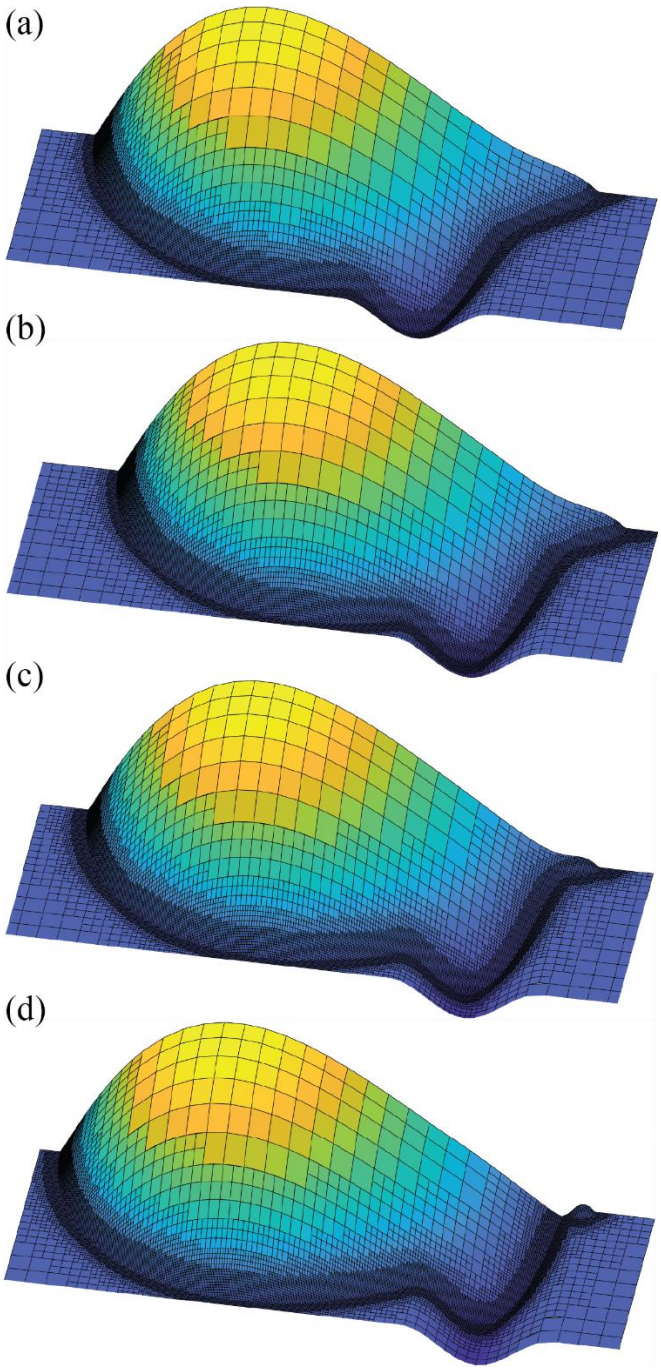

Figure 6.2: Curvature formation at the receding contact line for $\text{Å} = 0.1$ at times: (a) 4.55, (b) 4.76, (c) 4.98, (d) 5.29

Shortly afterwards of tail formation, residual pearl deposition occurs as shown in figure 6.2(d). We believe this process is significantly affected by slope of the topography. To show that we plot lateral propagation of droplet for these three cases where location of the advancing contact line is same, $L_x = 4.59$ to be precise, for all (Figure 6.3).

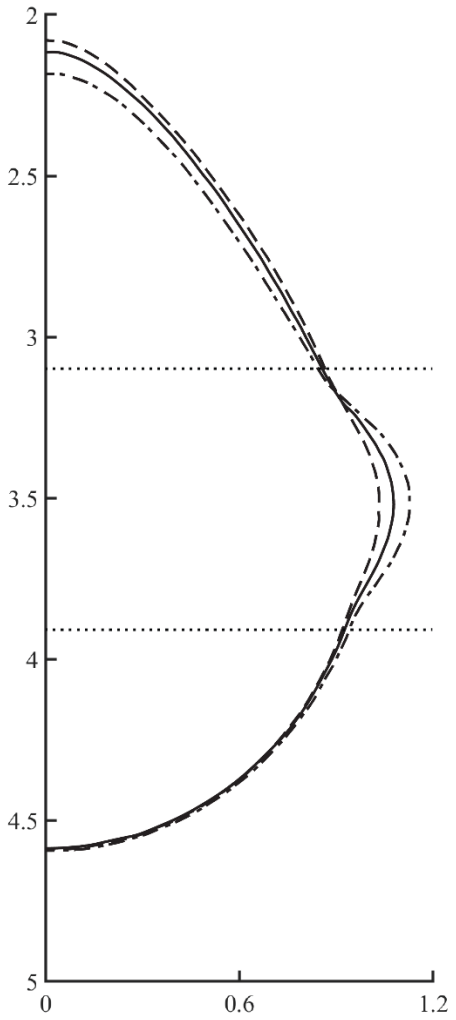

Figure 6.3: Propagation of lateral contact line from *x-y* plane for $(- \cdot -)$: $\text{Å} = 0.1$, $(-)$: $\text{Å} = 0.075$, $(- -)$: $\text{Å} = 0.05$, $(\cdots)$: Single sinusoidal cell

As expected, lateral propagation of contact line to groove increases as amplitude of the cell increases and we observe sharper curvatures. So, one should expect that the volume of small residual droplets increases directly proportional with this amplitude. However, that's not always true. For three different cases, we estimate the non-dimensional volume of these residual droplets ($\mathcal{V}_r$) and tabulate them in Table 6.1.

Table 6.1: Residual droplet volumes for various amplitudes

Å	$\mathcal{V}_r$
0.05	3.0118e-04
0.075	3.8101e-04
0.1	2.5236e-04

From Å $= 0.05$ to Å $= 0.075$, $\mathcal{V}_r$ increases proportionally. But in the steepest case, residual droplet gets smaller. Again, we believe this is result of the lateral affects and thus slope of the cell. Receding contact line is disturbed in all cases and it is forced to form a corner. Until a critical Å, we observe moderate curvatures at the receding contact line and residual droplet volume increases proportionally. However, amplitudes higher than critical Å enforce curvature into a sharper form and leads to a smaller residual droplet. To show that we plot the receding contact line of three cases for same advancing contact line location (see Figure 6.4).

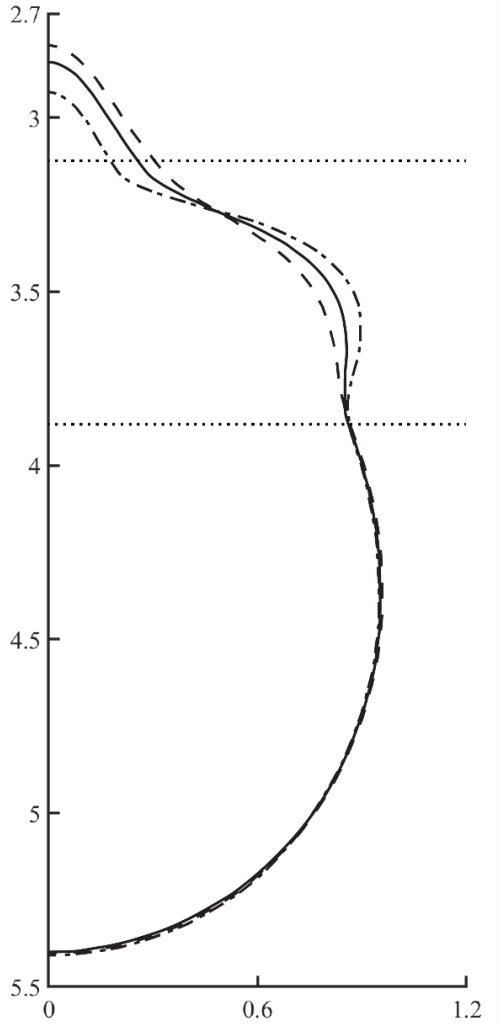

Figure 6.4: Aerial view (*x-y* plane) of curvature formation for $(- \cdot -)$: Å $= 0.1$, $(-)$: Å $= 0.075$, $(- -)$: Å $= 0.05$. $(\cdots)$: Single sinusoidal cell

Higher topography slopes provoke negative curvature formation at the receding contact line. As a result, we obtain sharper curvature in Å $= 0.1$ compared to smaller amplitudes. Outcomes from Figure 6.3 and Figure 6.4 lead us to a following

conclusion. Residual droplet pins and gets trapped for high slope cells. During this process, lateral contact line motion cambers the advancing contact line whilst caves the receding contact line of main droplet. These motions impel tail of main droplet to form a corner that later deposit a pearling to substrate. For small and medium amplitude slopes, in our problem $Å = 0.05$ and $Å = 0.075$, this enforcement is mild such that we get direct proportion of residual droplet deposition. But for high amplitudes, curvature forms rapidly and leaves relatively small pearling.

Now that we know effect of the slope from single cell, we analyze same problem with double and triple cells with $Å = 0.05$ to examine the effect of cell frequency. We choose the smallest slope to find out whether cell frequency can provoke droplet deposition or any other formation. Results are given in figure 6.5 below.

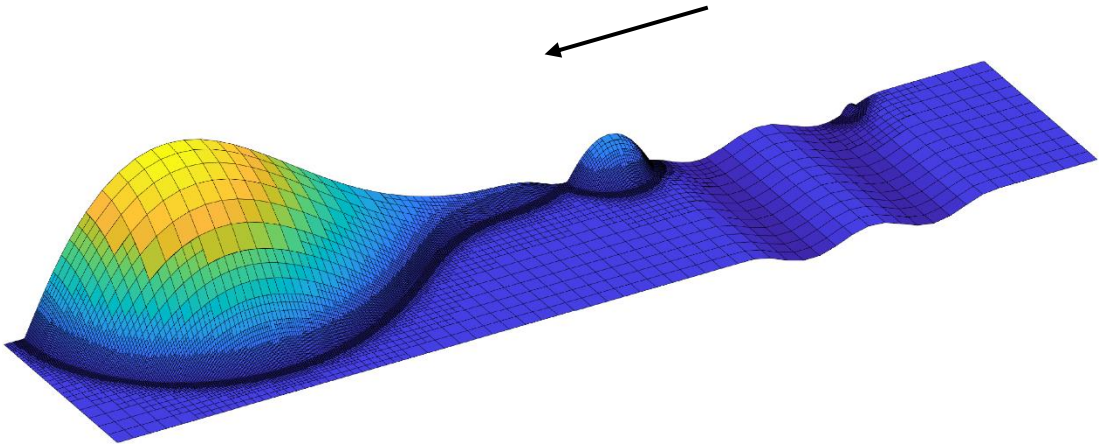

Figure 6.5: Droplet sliding over double sinusoidal cell with $Å = 0.05$ and $\lambda = 0.75$

In double cell, both big and small residual droplets form and has a non-dimensional volume of 1.6436e-04 and 0.0190, respectively. In this case, we examine different physics where contact angle hysteresis is drastically affected by the second cell. After droplet passes over first cell and deposits a residual pearl, it continues to slide over second groove and similar to single cell, curvature formation begins. However, this time receding contact line motion is retarded by upslope of the first cell. Before it deposits another residual droplet to second cell, receding contact line depins from the cell and rapidly slides downslope to merge with the formed curvature. By this way, second residual droplet formation onto next cell is prevented. But due to this additional

motion, we observe relatively big pearl after main droplet is completely freed from surface roughness. Upslope of the second cell has a role in this occurrence. Retention forces at the receding contact line increases due to pinning at the second cells upslope which retards its motion. Also, rivulet like formation occurs due to elongation of the main droplet as it slides away from the cells. Combination of these two effects eventually breaks the receding contact line and deposits a residual droplet to surface. Similar behavior is also observed in two-dimensional studies of Ceyhan [32] and Kumar [26]. Hereby, increment of cell frequency from single to double definitely changes the droplet formation even though overall contact line motion indicates similar behaviors. Main difference is the instantaneous pinning of receding contact line at the first cell which later depins from the surface and merges with the curvature that later assists droplet deposition by increasing the retention force at the second cell. Finally, we increase cell number for the last time. Results of triple cells are given in figure 6.6.

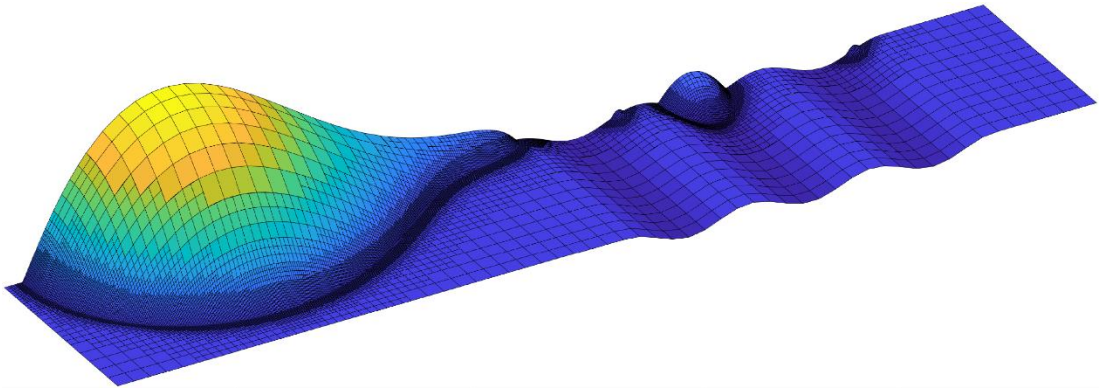

Figure 6.6: Droplet sliding over triple sinusoidal cell with $\text{Å} = 0.05$ and $\lambda = 0.75$

For the first time, we trap a droplet with a volume of 0.0149 at the second (middle) cell for specified Å. Other two residual droplet volumes are 1.2644e-04 and 8.2955e-04 respectively. In this final case, we mostly observe same physics with single and double cells. But occurrence of these physics and third residual droplet formation differs from the previous ones. Also notice that volume of first residual droplet is smaller than it is in double cell. Droplet is long enough to slide over all three cells at once. Thus, different curvature regimes are observed at each cell. So, this could be the reason for lesser volume in this case. We separate the sliding motion of the droplet in 3 parts as (i), (ii) and (iii) representing the location of receding contact line at each cell

to clarify this complex process. (i) Droplet already depins from the third cell by the time first residual deposits to surface. During this time, there exists several curvature structures for each individual cells (see Figure 6.7).

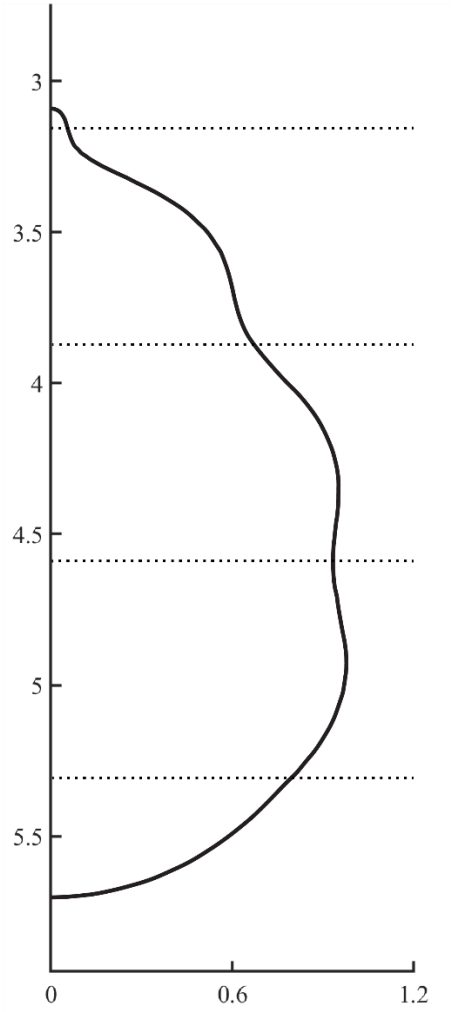

Figure 6.7: Aerial view of curvature formation for triple sinusoidal function with $\text{Å} = 0.05$ and $\lambda = 0.75$

(ii) Receding contact line shows exact behavior as it is in double cell case where it pins to upslope of first groove and then unites with the curvature at the second groove. However, this time there exist additional curvature formation at the third cell, that we don't have in double cell case, significantly assists retention forces emerging from upslope. This is because, curvature decreases the gravitational effect that pulls the residual droplet toward main droplet while coalescence of tail and residual droplet increases retention force alongside with upslope. With combination of these effects, receding contact line separates from the main droplet and pins to the second cell. We

believe this process is actually similar to double cell case where residual droplet forms due to both upslope and curvature that emerges from elongating tail. However, this process is not fast enough to trap the droplet inside the groove, mainly, droplet is sliding over a flat substrate rather than a rough one. Here, third cell accelerates this negative curvature formation and thus we can trap the residual droplet inside the groove. (iii) Third residual droplet is the most unique one out of all these formations. When a pearling or residual droplet forms, receding contact line breaks at a single point either caused by curvature, slope of the surface roughness or both. But formation of the third droplet occurs differently. While residual droplet begins to come in sight, a bridge like rivulet forms between main droplet and nascent residual droplet. As residual droplet pulls with retention force, sliding main droplet also pulls this bridge. Then, eventually it breaks and forms this tiny residual droplet.

In conclusion, we examine the effect of slope and frequency of cell effect on the formation of droplets. We provide an explanation to these incidents by analyzing single, double and triple sinusoidal cells for various slopes. We show that lateral contact line motion is responsible from the residual droplet formation and it is susceptible to slope of the topography. We find that to trap and pin a droplet, frequent and steep topographies must be used to maximize the trapped volume.

6.2 Trapping Droplets on Sinusoidal Substrates

In this section, we use the knowledge from §6.1 to define our rough surface. We use sinusoidal function throughout the domain to maximize droplet entrapment. For various Å, we examine the trapped droplets. Droplet properties are same with §6.1 which are $Bo = 1.1$, $f_0 = 0.0025$, $\theta_e = 30°$ and $\alpha = 90°$ where amplitudes are $\text{Å} = 0.025$, $\text{Å} = 0.05$ and $\text{Å} = 0.075$ and frequency is $\lambda = 0.75$. Results for three different amplitudes are represented in figure 6.8.

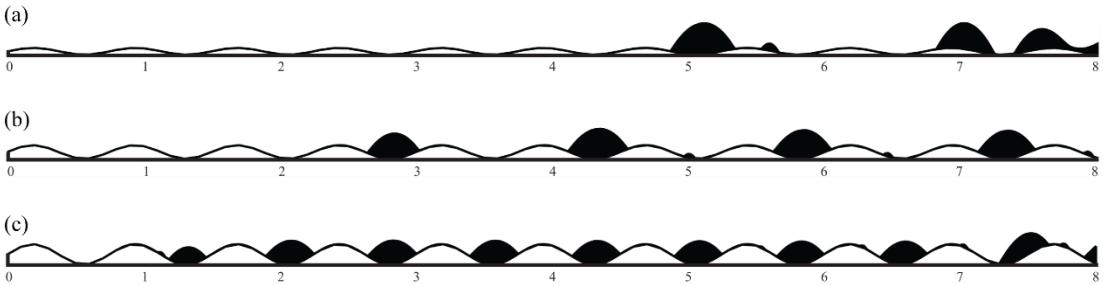

Figure 6.8: Entrapment of droplets for (a): $\text{Å} = 0.025$, (b): $\text{Å} = 0.05$, (c): $\text{Å} = 0.075$ for same frequency $\lambda = 0.75$

With given parameters, $\text{Å} = 0.075$ cell traps droplets at each groove while cell with $\text{Å} = 0.05$ traps droplets once in every two grooves. As we stated before in §6.1, for increasing amplitudes we trap more droplets. Also, we observe the same physics for $\text{Å} = 0.05$ as we predict in §6.1 for triple cells. It traps droplet in between three cells through whole domain. In $\text{Å} = 0.075$, droplet exhibits stick-slip motion and the effect of retention forces increases as main droplet leaves residuals to each cell. We also detect tiny residual droplets after each entrapment similar to part (iii) of triple cell in §6.1. Both advancing and receding contact line exhibits complex curvature formation that assists entrapment. We cannot trap droplets until the end of our domain for $\text{Å} = 0.025$. This is expected since it is nearly flat substrate compared to outer configurations. The total trapped volumes ($\mathcal{V}_t$) are tabulated in table 6.2 for each Å.

Table 6.2: Total volume of trapped droplets

Å	$\mathcal{V}_t$	% of main droplet
0.025	0.0418	2.6
0.05	0.0606	3.7862
0.075	0.0745	4.6325

In table 6.2, we exclude tiny volumes that are smaller than %0.2 of main droplet. Results show that cell with the highest slope has the highest total trapped volume and it decreases as Å gets smaller. Because $\text{Å} = 0.025$ is the smallest in $\mathcal{V}_t$ and cannot properly trap even small droplets, we exclude this slope from this point on. We prepare table 6.3 to demonstrate each trapped droplets volume for remaining Å at given cell

number. In total we examine 9 cells from $1 \leq L_x \leq 8$ and $0 \leq L_y \leq 1.2$. Notice that we don't include first cell between $0 \leq L_x \leq 1$ because droplet initialized there.

Table 6.3: Trapped droplet volumes at each cell for various Å

#Cell	$\mathcal{V}_t$ for Å $= 0.05$	% Of main droplet	$\mathcal{V}_t$ for Å $= 0.075$	% of main droplet
1	-	-	0.0038	0.2363
2	-	-	0.0092	0.5721
3	0.0109	0.6778	0.0094	0.5845
4	-	-	0.0092	0.5721
5	0.0177	1.1006	0.0089	0.5534
6	-	-	0.0087	0.541
7	0.0156	0.97	0.0084	0.5223
8	-	-	0.0082	0.51
9	0.0140	0.8705	0.0080	0.4975

Both topographies show similar trapping characteristics in the sense of $\mathcal{V}_t$ increase and decrease rate. First trapped droplet is small where following droplet is bigger than the first one. From this point on, trapped droplet volume decreases gradually and continuously. It is because gravitational force that pulls the tail toward main droplet decreases as residual droplets trap in between each groove. Lastly, we give figure 6.9 to present final state of the domain with trapped residuals for Å $= 0.075$.

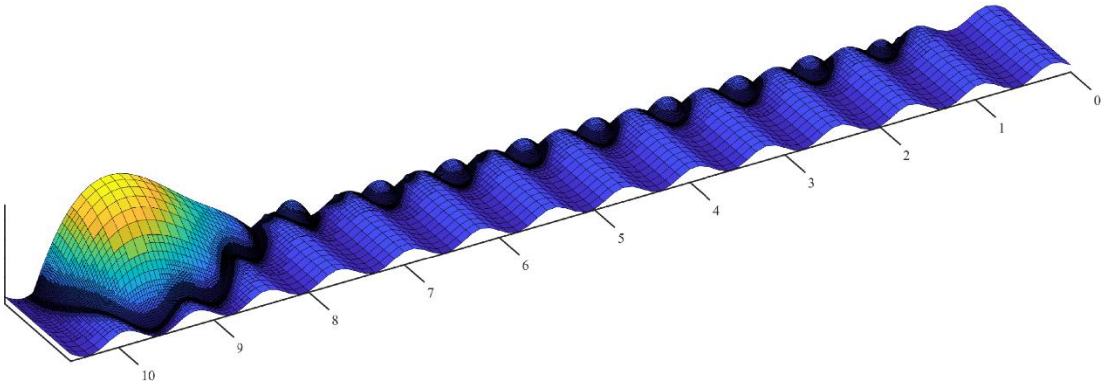

Figure 6.9: Detailed view of Å $= 0.075$ and $\lambda = 0.75$ domain in figure 6.8(c)

Until now, we get physics that agrees with our previous findings in §6.1 where we change the topography slopes. Now, we adjust the cell frequency by changing the λ in equation (2.1). We set it to 1.125 for $\text{Å} = 0.075$ and analyze the possible changes (see Figure 6.10).

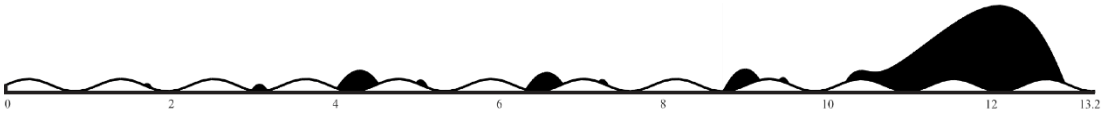

Figure 6.10: *x-z* plane view of sliding droplet over sinusoidal cell with same amplitude, $\text{Å} = 0.075$, as in Figure 6.8(c) but with higher frequency $\lambda = 0.125$

Here, distance between two peaks of sinusoidal topography increased which results decrease in droplet entrapment. We expect to trap lesser volumes in total because even though amplitude is same with Figure 6.9, higher distance between two peaks results in slower curvature formation. Interestingly, we obtain periodic entrapment similar to $\text{Å} = 0.05$ with $\lambda = 0.75$. We remark that for higher λ, total number of cells for same length decreases. So, for $\text{Å} = 0.05$ and $\lambda = 0.75$, we have 8 cells in between $0 \leq L_x \leq 8$. For $\text{Å} = 0.075$ and $\lambda = 1.125$, we have 6 cells. Comparison between all four cases is presented in Figure 6.11.

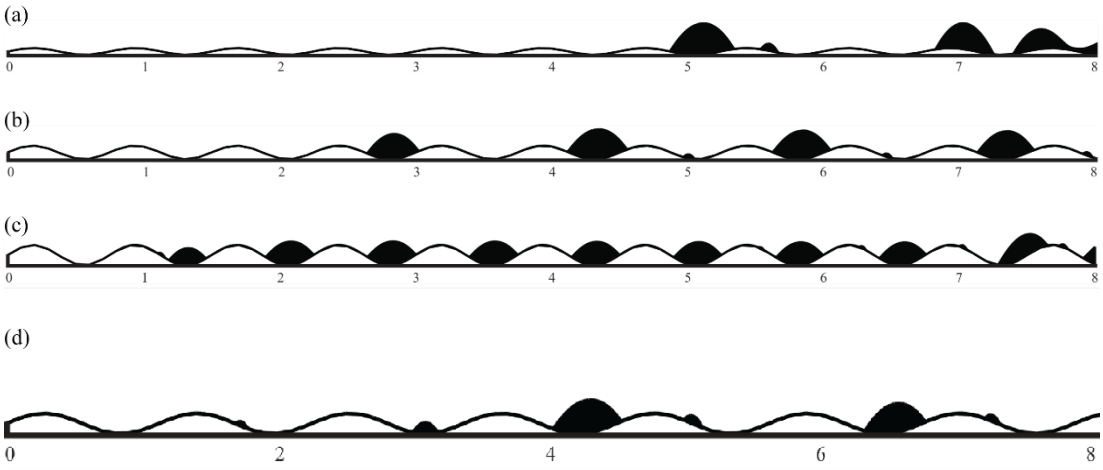

Figure 6.11: Entrapment of droplets for (a): $\text{Å} = 0.025$, (b): $\text{Å} = 0.05$, (c): $\text{Å} = 0.075$ for same frequency $\lambda = 0.75$, (d): $\text{Å} = 0.05$ and $\lambda = 1.25$

In total, we trap %3.4577 of main droplets volume at 8 grooves for given case which is close but higher than cell with $\text{Å} = 0.05$ and $\lambda = 0.75$. This demonstrates that we can find similar behaviors for higher slopes by changing the cell frequency. However, even though we find better entrapment compared to smaller slope, we trap %1.175 less compared to same slope ($\text{Å} = 0.075$) with high frequency wave ($\lambda = 0.75$). These results are again matching with our previous examinations for single, double and triple cell section. In conclusion we require high slope and frequent topography to trap higher volumes.

Table 6.4: Trapped volumes comparison between lower slope high frequency and high slope low frequency cells

#Cell	$\mathcal{V}_t$ for $\text{Å} = 0.05$ $\lambda = 0.75$	% of main droplet	$\mathcal{V}_t$ for $\text{Å} = 0.075$ $\lambda = 0.125$	% of main droplet
1	-	-	-	-
2	-	-	-	-
3	0.0109	0.6778	0.0241	1.6082
4	-	-	-	-
5	0.0177	1.1006	0.0166	1.0322
6	-	-	-	-
7	0.0156	0.97	0.0149	0.9265
8	-	-	-	-

Chapter 7

Conclusion

Manipulation of droplet motion such as delaying and entrapment is beneficial for many industrial applications. These features depend on contact angle hysteresis which is susceptible to surface roughness. There are numerous amounts of studies in the literature based on this topic. But entrapment of a droplet has received little attention. Motivated by this we study on three-dimensional slender droplets with lubrication approximation on rough surface. Surface roughness is implemented as a continuous sinusoidal function. We implement our own finite element method-based solver to investigate this problem. To get accurate results within a feasible computation time, we also implement an adaptive mesh refiner with quadtree data structure and embed it into our FEM solver. We validate our solver with three benchmark studies from literature. First one is Tanner's law [73] where we investigate the maximum droplet height change with respect to time for spreading droplet on a flat and horizontal substrate. Second is the relation between capillary and Bond number from Podgorski's experimental study [49]. For sliding droplet on a flat substrate, we gradually increase inclination angle and investigate the change of capillary number. We compare our results with other two numerical study of Kumar [54] and Ahmed [61]. We find similar physics with both theoretical and experimental studies. Finally, we examine the change of cube of advancing contact line with capillary number which we find linear relation between θ_A^3 and Ca. Our results are compatible with Cox-Voinow Law [52,75].

We begin to our main problem by examining the factors that affect droplet deposition. To show that we first study on a single sinusoidal groove with various amplitudes/slopes. We observe that entrapment of droplet increases for higher amplitudes. This is because lateral contact line of a sliding droplet on a higher slope propagates more to grooves which later recedes and pulls the tail of main droplet. This

motion expedites the negative curvature formation that later leads to a residual pearl. For double cell, we examine pearl deposition after receding contact line leaves the cell. Even though we observe similar physics, second cell affects the curvature formation that leads to a pearl later. At the upslope of first cell, receding contact line instantaneously pins and negative curvature formation begins at the second cell. However, tail depins from the first cell and merges with the curvature which increases the retention forces at the second cell. As advancing contact line continues to proceed, tail of the droplet elongates due to increased retention forces and later deposits a big pearl to outside of the cells. This is caused by combined influence of curvature and upslope of second cell. Triple case is the most complex one and we explain it in three separate parts (i), (ii) and (iii) representing the location of receding contact line at corresponding cell. (i) We observe similar results with singular case. But droplet is long enough to cover all three cells that reveals complex curvature formations at each individual cell. (ii) Again, we also observe similar physics with double case, however, this time droplet has a part on third cell with a curvature that significantly assists pearl deposition. This is because coalescence of tail and nascent residual pearl already increases the retention forces and with this additional curvature profile from the third cell, receding contact line is forced to separate from the main droplet and pins to second cell. (iii) We observe another residual pearl in third cell. But formation of this one is different from the rest. This pearl occurs during the pinning process on second cell. Whilst main droplet pulls nascent residual pearl towards itself, retention force emerges from this residual droplet also pulls itself to cell. From this force balance, residual droplet forms and pins to downslope of third cell.

Finally, we proceed to our original problem which is a continuous sinusoidal surface. We analyze three different amplitudes for same frequency and find out that the steepest cell traps the highest volume of residual pearls at every cell whilst middling cell traps residuals periodically. To see the effect of cell frequency, we use high slope and less frequent surface configuration. We show that for same high slope, we trap less residual droplet in less frequent cell configuration. These two results are matching with our previous findings that lead us to following conclusion. To trap a droplet on a surface, we require high slope and small frequency/high frequent cell. We believe that our study contributes to understanding of droplet entrapment and would motivate other theoretical and experimental studies.

References

[1] Parker AR, Lawrence CR. Water capture by a desert beetle. Nature 2001; 414: 33-34. doi.org:10.1038/35102108

[2] Noorgard T, Dacke M. Fog-basking behaviour and water collection efficiency in Namib Desert Darkling beetles. Frontiers in Zoology 2010; 7: 23. doi.org:10.1186/1742-9994-7-23

[3] Park J, Lim H, Kim W, Ko JS. Design and fabrication of a superhydrophobic glass surface with micro-network of nanopillars. Journal of Colloid and Interface Science 2011; 360: 272-279. doi.org:10.1016/j.jcis.2011.04.047

[4] Fürstner R, Barthlott W, Neinhuis C, Walzel P. Wetting and Self-Cleaning Properties of Artificial Superhydrophobic Surfaces. Langmuir 2005; 21(3): 956-961. doi.org:10.1021/la0401011

[5] Liu M, Wang J, He M, Wang L, Li F, Jiang L, Song Y. Inkjet Printing Controllable Footprint Lines by Regulating the Dynamic Wettability of Coalescing Ink Droplets. ACS Applied Materials & Interfaces 2014; 6(16): 13344-13348. doi.org:10.1021/am5042548

[6] Thompson AB, Tipton CR, Juel A, Hazel AL, Downling M. Sequential deposition of overlapping droplets to form a liquid line. Journal of Fluid Mechanics 2014; 761: 261-281. doi.org:10.1017/jfm.2014.621

[7] Anand S, Paxon AT, Dhiman R, Smith JD, Varanasi KK. Enhanced Condensation on Lubricant-Impregnated Nanotextured Surfaces. ACS Nano 2012; 6(11): 10122-10129. doi.org:10.1021/nn303867y

[8] Milijkovic N, Wang EN. Condensation heat transfer on superhydrophobic surfaces. MRS Bulletin 2013; 38(5): 397-406. doi.org:10.1557/mrs.2013.103

[9] Gao X, Yan X, Yao X, Xu L, Zhang K, Yang B, Jiang L. The Dry-Style Antifogging Properties of Mosquito Compound Eyes and Artificial Analogues Prepared by Soft Lithography. Advanced Materials 2007; 19(17): 2213-2217. doi.org:10.1002/adma.200601946

[10] Lv J, Song Y, Jiang L, Wang J. Bio-Inspired Strategies for Anti-Icing. ACS Nano 2014; 8(4): 3152-3169. doi.org:doi.org/10.1021/nn406522n

[11] Extrand CW. Origins of wetting. Langmuir 2016; 32(31): 7697-7706. doi.org:10.1021/acs.langmuir.6b01935

[12] Hauksbee F. VIII. An experiment made at Gresham-College, shewing that the seemingly spontaneous ascention of water in small tubes open at both ends is the same in vacuo as in the open air. Royal Society 1706; 25: 305. doi.org:10.1098/rstl.1706.0008

[13] Young T. III. An essay on the cohesion of fluids. Royal Society 1805; 95. doi.org:10.1098/rstl.1805.0005

[14] Gennes PG. Wetting: statics and dynamics. Review of modern physics 1985; 57: 827. doi.org:10.1103/RevModPhys.57.827

[15] Furmidge CGL. Studies at phase interfaces. I. The sliding of liquid drops on solid surfaces and a theory for spray retention. Journal of Colloid Science 1962; 17(4): 309-324. doi.org:10.1016/0095-8522(62)90011-9

[16] Bikerman JJ. Sliding of drops from surfaces of different roughnesses. Journal of Colloid Science 1950; 5(4): 349-359. doi.org: 10.1016/0095-8522(50)90059-6

[17] Eral HB, Mannetje DJCM, Oh JM. Contact angle hysteresis: a review of fundamentals and applications. Colloid and Polymer Science 2013; 291: 247-260. doi.org:10.1007/s00396-012-2796-6

[18] Oron A, Davis H, Bankoff SG. Long-scale evolution of thin liquid films. Reviews of Modern Physics 1997; 69: 931. doi.org:10.1103/RevModPhys.69.931

[19] Huh C, Scriven LE. Hydrodynamic model of steady movement of a solid/liquid/fluid contact line. Journal of Colloid and Interface Science 1971; 35(1): 85-101. doi.org:10.1016/0021-9797(71)90188-3

[20] Hocking LM. Sliding and Spreading of Thin Two-Dimensional Drops. The Quarterly Journal of Mechanics and Applied Mathematics 1981; 34(1): 37-55. doi.org:10.1093/qjmam/34.1.37

[21] Ruckenstein E, Dunn CS. Slip velocity during wetting of solids. Journal of Colloid and Interface Science 1977; 59(1): 135-138. doi.org:10.1016/0021-9797(77)90347-2

[22] Peschka D. Variational approach to dynamic contact angles for thin films. Physics of Fluids 2018; 30: 8. doi.org:10.1063/1.5040985

[23] Benilov ES, Benilov MS. A thin drop sliding down an inclined plate. Journal of Fluid Mechanics 2015; 773: 75-102. doi.org:10.1017/jfm.2015.226

[24] Savva N, Kalliadasis S. Droplet motion on inclined heterogeneous substrates. Journal of Fluid Mechanics 2013; 725: 462-491. doi.org:10.1017/jfm.2013.201

[25] Schwartz LW, Eley RR. Simulation of Droplet Motion on Low-Energy and Heterogeneous Surfaces. Journal of Colloid and Interface Science 1998; 202(1): 173-188. doi.org:10.1006/jcis.1998.5448

[26] Park J, Kumar S. Droplet Sliding on an Inclined Substrate with a Topographical Defect. Langmuir 2017; 33(29): 7352-7363. doi.org:10.1021/acs.langmuir.7b01716

[27] Mayo LC, McCue SW, Moroney TJ, Forster WA, Kempthrone DM, Belward JA, Turner W. Simulating droplet motion on virtual leaf surfaces. Royal Society 2015; 2: 5. doi.org:10.1098/rsos.140528

[28] Yin H, Sibley DN, Thiele U, Archer AJ. Films, layers, and droplets: The effect of near-wall fluid structure on spreading dynamics. Physical Review E 2017; 95: 2. doi.org:10.1103/PhysRevE.95.023104

[29] Espin L, Kumar S. Sagging of Evaporating Droplets of Colloidal Suspensions on Inclined Substrates. Langmuir 2014; 30(40): 11966-11974. doi.org:10.1021/la503229z

[30] Thiele U, Snoeijer JH, Trinschek S, John K. Equilibrium Contact Angle and Adsorption Layer Properties with Surfactants. Langmuir 2018: 34(24): 7210-7221. doi.org:10.1021/acs.langmuir.8b00513

[31] Sibley DN, Nold A, Savva N, Kalliadasis S. A comparison of slip, disjoining pressure, and interface formation models for contact line motion through asymptotic analysis of thin two-dimensional droplet spreading. Journal of Engineering Mathematics 2015; 94: 19-41. doi.org:10.1007/s10665-014-9702-9

[32] Ceyhan U, Tiktaş A, Özdoğan M. Pinning and depinning of Wenzel-state droplets around inclined steps. Colloid and Interface Science Communications 2020; 35: 100238. doi.org:10.1016/j.colcom.2020.100238

[33] Thiele U, Knobloch E. On the depinning of a driven drop on a heterogeneous substrate. New Journal of Physics 2016; 8: 313. doi.org:10.1088/1367-2630/8/12/313

[34] Kalinin YV, Berejnov V, Thorne RE. Contact Line Pinning by Microfabricated Patterns: Effects of Microscale Topography. Langmuir 2009; 25(9): 5391-5397. doi.org:10.1021/la804095y

[35] Arscott S. Dynamic Chemically Driven Dewetting, Spreading, and Self-Running of Sessile Droplets on Crystalline Silicon. Langmuir 2016; 32(48): 12611-12622. doi.org:10.1021/acs.langmuir.6b03287

[36] Chagas GR, Celestini F, Raufaste C, Gaucher A, Prim D, Amigoni S, Guittard F, Darmanin T. Experimental Characterization of Droplet Adhesion: The Ejection Test Method (ETM) Applied to Surfaces with Various Hydrophobicity. The Journal of Physical Chemistry A 2018; 122(43): 8693-8700. doi.org:10.1021/acs.jpca.8b08037

[37] Zhang Y, Fuentes CA, Koekoekx R, Clasen C, Vuure AWV, Coninck JD, Seveno D. Spreading Dynamics of Molten Polymer Drops on Glass Substrates. Langmuir 2017; 33(34): 8447-8454. doi.org:10.1021/acs.langmuir.7b01500

[38] Hou P, Steinhart M. Immobilization of Water Drops on Hydrophobic Surfaces by Contact Line Pinning at Nonlithographically Generated Polymer Microfiber Rings. Advanced Materials Interfaces 2018; 5(24): 1801191. doi.org:10.1002/admi.201801191

[39] Ha JW, Park IJ, Lee SB. Hydrophobicity and Sliding Behavior of Liquid Droplets on the Fluorinated Latex Films. Macromolecules 2005; 38(3): 736-744. doi.org:10.1021/ma0488764

[40] Wang H. From Contact Line Structures to Wetting Dynamics. Langmuir 2019; 35(32): 10233-10245. doi.org:10.1021/acs.langmuir.9b00294

[41] Neyrand V, Bergheau JM, Benayoun S, Valette S. Numerical simulation of wetting on a chemically textured surface with a large intrinsic contact angle ratio by the Lattice Boltzmann Method. Experimental and Computational Multiphase Flow 2022; 4: 165-174. doi.org:10.1007/s42757-020-0091-1

[42] Law KY. Contact Angle Hysteresis on Smooth/Flat and Rough Surfaces. Interpretation, Mechanism, and Origin. Accounts of Materials Research 2022; 3(1): 1-7. doi.org:10.1021/accountsmr.1c00051

[43] Thiele U, Knobloch E. Front and back instability of a liquid film on a slightly inclined plate. Physics of Fluids 2003; 15: 892. doi.org:10.1063/1.1545443

[44] Thiele U, Neuffer K, Bestehorn M, Pomeau Y, Velarde MG. Sliding drops on an inclined plane. Colloids and Surfaces A: Physicochemical and Engineering Aspects 2002; 206(1-3): 87-104. doi.org:10.1016/S0927-7757(02)00082-1

[45] Pismen LM, Pomeau Y. Mobility and interactions of weakly nonwetting droplets. Physics of Fluids 2004; 16: 2604. doi.org:10.1063/1.1758911

[46] Mahadevan L, Pomeau Y. Rolling droplets. Physics of Fluids 1999; 11: 2449. doi.org:10.1063/1.870107

[47] Thiele U. Depinning of three-dimensional drops from wettability defects. Europhysics Letters Association 2009; 86(2): 24006. doi.org:10.1209/0295-5075/86/24006

[48] Snoeijer JH, Rio E, Grand NL, Limat L. Self-similar flow and contact line geometry at the rear of cornered drops. Physics of Fluids 2005; 17(7): 2101. doi.org:10.1063/1.1946607

[49] Podgorski T, Flesselles JM, Limat L. Corners, Cusps, and Pearls in Running Drops. Physical Review Letters 2001; 87(3): 6102. doi.org:10.1103/PhysRevLett.87.036102

[50] Snoeijer JH, Grand NL, Limat L, Stone HA, Eggers J. Cornered drops and rivulets. Physics of Fluids 2007; 19(4): 2104. doi.org:10.1063/1.2722767

[51] Winkels KG, Peters IR, Evangelista F, Riepen M, Daerr A, Limat L, Snoeijer JH. Receding contact lines: From sliding drops to immersion lithography. The European Physical Journal Special Topics 2011; 192: 195-205. doi.org:10.1140/epjst/e2011-01374-6

[52] Cox RG. The dynamics of the spreading of liquids on a solid surface. Part 1. Viscous flow. Journal of Fluid Mechanics 1986; 168: 169-194. doi.org:10.1017/S0022112086000332

[53] Schwartz LW, Roux D, White JJC. On the shapes of droplets that are sliding on a vertical wall. Physica D: Nonlinear Phenomena 2005; 209(1-4): 236-244. doi.org:10.1016/j.physd.2005.07.001

[54] Espin L, Kumar S. Droplet wetting transitions on inclined substrates in the presence of external shear and substrate permeability. Physical Review Fluids 2016; 2(1): 4004. doi.org:10.1103/PhysRevFluids.2.014004

[55] Wu Y, Kuzina M, Wang F, Reischl M, Selzer M, Nestler B, Levkin PA. Equilibrium droplet shapes on chemically patterned surfaces: theoretical calculation, phase-field simulation, and experiments. Journal of Colloid and Interface Science 2022; 606(2): 1077-1086. doi.org:10.1016/j.jcis.2021.08.029

[56] Derjaguin B. A theory of capillary condensation in the pores of sorbents and of other capillary phenomena taking into account the disjoining action of polymolecular liquid films. Progress in Surface Science 1992; 40(1-4): 46-61. doi.org:10.1016/0079-6816(92)90032-D

[57] Hamaker HC. The London—van der Waals attraction between spherical particles. Physica 1937; 4(10): 1058-1072. doi.org:10.1016/S0031-8914(37)80203-7

[58] Extrand CW, Moon SI. When Sessile Drops Are No Longer Small: Transitions from Spherical to Fully Flattened. Langmuir 2010; 26(14): 11815-11822. doi.org:10.1021/la1005133

[59] Bathe KJ. Finite element procedures; 1996.

[60] Diez JA, Kondic L. Contact Line Instabilities of Thin Liquid Films. Physical Review Letters 2001; 86: 632. doi.org:10.1103/PhysRevLett.86.632

[61] Ahmed G, Sellier M, Jermy M, Taylor M. Modeling the effects of contact angle hysteresis on the sliding of droplets down inclined surfaces. European Journal of Mechanics - B/Fluids 2014; 48: 218-230. doi.org:10.1016/j.euromechflu.2014.06.003

[62] Koh YY, Lee YC, Gaskell PH, Jimack PK, Thompson HM. Droplet migration: Quantitative comparisons with experiment. The European Physical Journal Special Topics 2009; 166: 117-120. doi.org:10.1140/epjst/e2009-00890-2

[63] Almgren AS, Bell JB, Colella P, Howell LH, Welcome ML. A Conservative Adaptive Projection Method for the Variable Density Incompressible Navier–Stokes Equations. Journal of Computational Physics 1998; 142(1): 1-46. doi.org:10.1006/jcph.1998.5890

[64] Li Z, Song P. An Adaptive Mesh Refinement Strategy for Immersed Boundary/Interface Methods. Communications in Computational Physics 2015; 12(2): 515-527. doi.org:10.4208/cicp.070211.150811s

[65] Popinet S. Gerris: a tree-based adaptive solver for the incompressible Euler equations in complex geometries. Journal of Computational Physics 2003; 190(2): 572-600. doi.org:10.1016/S0021-9991(03)00298-5

[66] Popinet S. An accurate adaptive solver for surface-tension-driven interfacial flows. Journal of Computational Physics 2009; 228(16): 5838-5866. doi.org:10.1016/j.jcp.2009.04.042

[67] Popinet S. A quadtree-adaptive multigrid solver for the Serre–Green–Naghdi equations. Journal of Computational Physics 2015; 302(1): 336-358. doi.org:10.1016/j.jcp.2015.09.009

[68] Theodorakakos A, Bergeles G. Simulation of sharp gas–liquid interface using VOF method and adaptive grid local refinement around the interface. Numerical Methods in Fluids 2004; 45(4): 421-439. doi.org:10.1002/fld.706

[69] Cerveny J, Dobrev V, Kolev T. Nonconforming Mesh Refinement for High-Order Finite Elements. SIAM Journal on Scientific Computing 2019; 41(4): C367-C392. doi.org:10.1137/18M1193992

[70] Carstensen S, Hu J. Hanging Nodes in The Unifying Theory of a Posteriori Finite Element Error Control. Journal of Computational Mathematics 2009; 27(2-3): 215-236.

[71] Fries TP, Byfut A, Alizada A, Cheng KW, Schröder A. Hanging nodes and XFEM. Numerical Methods in Engineering 2010; 86(4-5): 404-430. doi.org:10.1002/nme.3024

[72] Babuska I, Strouboulis T, Mathur A, Upadhyay CS. Pollution-error in the of the finite-element method and the local quality of a-posteriori error estimators. Finite Elements in Analysis and Design 1994; 17(4): 273-321. doi.org:10.1016/0168-874X(94)90003-5

[73] Tanner LH. The spreading of silicone oil drops on horizontal surfaces. Journal of Physics D: Applied Physics 1979; 12(9): 1473-1484. doi.org:10.1088/0022-3727/12/9/009

[74] Grand NL, Daerr A, Limat L. Shape and motion of drops sliding down an inclined plane. Journal of Fluid Mechanics 2005; 541: 293315. doi:10.1017/S0022112005006105

[75] Voinov OV. Hydrodynamics of wetting. Fluid Dynamics 1976; 11: 714-721. doi.org:10.1007/BF01012963

[76] Oliver JF, Mason SG. Microspreading Studies on Rough Surfaces by Scanning Electron Microscopy. Journal of Colloid and Interface Science 1977; 60(3): 480-487. doi.org:10.1016/0021-9797(77)90312-5

[77] Yong KW, Ganesan PB, Kazi MSN, Ramesh S, Badruddin IA, Mubarak NM. Sliding behavior of droplet on a hydrophobic surface with hydrophilic cavities: A simulation study. Physics of Fluids 2018; 30(12): 2006. doi.org:10.1063/1.5063857

[78] Liang W, Tietze S. Pearls in running drops on an inclined glass substrate excited by Lamb waves. Scientific Reports 2017; 7: 14164. doi.org:10.1038/s41598-017-14662-9

[79] Cox RG. The spreading of a liquid on a rough solid surface. Journal of Fluid Mechanics 1983; 131: 1-26. doi.org:10.1017/S0022112083001214

Appendices

Appendix A

Non-dimensional Film Evolution Equation

We use given scales in section 2.2 to non-dimensionalize evolution equation. Velocity and pressure related parameters, u_s and Π_s are found by rearranging the film evolution equation. After the alterations, film evolution equation is given below.

$$\frac{3\mu\, u_s}{\gamma\, \varepsilon^3}\frac{\partial f}{\partial t} + \frac{\partial}{\partial x}\left[-f^3\left(\frac{\rho g\, x_s^2\, \cos\alpha}{\gamma}\frac{\partial(f+h)}{\partial x} - \frac{\partial^3(f+h)}{\partial x^3}\right)\right]$$

$$+\frac{\partial}{\partial x}\left[-f^3\left(-\frac{\partial^2(f+h)}{\partial y^2}\frac{\partial}{\partial x} - \frac{\Pi_s\, x_s}{\varepsilon\, \gamma}\frac{\partial \Pi}{\partial x} - \frac{\rho\, g\, x_s^2\, \sin\alpha}{\gamma}\frac{1}{\varepsilon}\right)\right]$$

$$+\frac{\partial}{\partial y}\left[-f^3\left(\frac{\rho g\, y_s^2\, \cos\alpha}{\gamma}\frac{\partial(f+h)}{\partial y} - \frac{\partial^3(f+h)}{\partial y^3}\right)\right]$$

$$+\frac{\partial}{\partial y}\left[-f^3\left(-\frac{\partial^2(f+h)}{\partial x^2}\frac{\partial}{\partial y} - \frac{\Pi_s\, y_s}{\varepsilon\, \gamma}\frac{\partial \Pi}{\partial y}\right)\right] = 0 \qquad \text{(A.1)}$$

Equalizing the accompanied constants to one while taking $x_s = y_s = R\sin\theta_e$ yields to following scales.

$$u_s = \frac{\varepsilon^3\gamma}{3\mu} \qquad \text{(A.2)}$$

$$\Pi_s = \frac{\gamma\ \varepsilon}{R \sin\theta_e} \tag{A.3}$$

$$t_s = \frac{R \sin\theta_e\ 3\mu}{\gamma\ \varepsilon^3} \tag{A.4}$$

$$Bo = \frac{\rho\ g\ (R \sin\theta_e)^2}{\gamma} \tag{A.5}$$

Appendix B

Weak Formulation of Droplet Thickness

We weaken the equation (3.1) with the same process as we do to equation (3.2).

$$\int_{\Omega} \frac{\partial f}{\partial t}\overline{f}\, d\Omega + \int_{\Omega} \frac{\partial}{\partial x}\left(-Bo\cos\alpha\, f^3 \frac{\partial f}{\partial x}\right)\overline{f}\, d\Omega$$

$$+ \int_{\Omega} \frac{\partial}{\partial x}\left(-Bo\cos\alpha\, f^3 \frac{\partial h}{\partial x}\right)\overline{f}\, d\Omega + \int_{\Omega} \frac{\partial}{\partial x}\left(f^3 \frac{\partial \mathrm{P}}{\partial x}\right)\overline{f}\, d\Omega$$

$$+ \int_{\Omega} \frac{\partial}{\partial y}\left(-Bo\cos\alpha\, f^3 \frac{\partial f}{\partial y}\right)\overline{f}\, d\Omega$$

$$+ \int_{\Omega} \frac{\partial}{\partial y}\left(-Bo\cos\alpha\, f^3 \frac{\partial h}{\partial y}\right)\overline{f}\, d\Omega + \int_{\Omega} \frac{\partial}{\partial y}\left(f^3 \frac{\partial \mathrm{P}}{\partial y}\right)\overline{f}\, d\Omega$$

$$\int_{\Omega} \frac{\partial}{\partial x}\left(f^3 \frac{Bo}{\varepsilon}\sin\alpha\right)\overline{f}\, d\Omega = 0 \qquad \text{(B.1)}$$

$$\int_{\Omega} \frac{\partial f}{\partial t}\overline{f}\, d\Omega + \int_{\Omega} \frac{\partial}{\partial x}\left(-Bo\cos\alpha\, f^3 \frac{\partial f}{\partial x}\,\overline{f}\right) d\Omega$$

$$-\int_{\Omega} \left(-Bo\cos\alpha\, f^3 \frac{\partial f}{\partial x}\right)\frac{\partial \overline{f}}{\partial x} d\Omega$$

$$+\int_{\Omega} \frac{\partial}{\partial x}\left(-Bo\cos\alpha\, f^3 \frac{\partial h}{\partial x}\,\overline{f}\right) d\Omega$$

$$-\int_{\Omega} \left(-Bo\cos\alpha\, f^3 \frac{\partial h}{\partial x}\right)\frac{\partial \overline{f}}{\partial x} d\Omega + \int_{\Omega} \frac{\partial}{\partial x}\left(f^3 \frac{\partial \mathrm{P}}{\partial x}\overline{f}\right) d\Omega$$

$$-\int_{\Omega} f^3 \frac{\partial \mathrm{P}}{\partial x}\frac{\partial \overline{f}}{\partial x} d\Omega + \int_{\Omega} \frac{\partial}{\partial y}\left(-Bo\cos\alpha\, f^3 \frac{\partial f}{\partial y}\,\overline{f}\right) d\Omega$$

$$-\int_{\Omega} \left(-Bo\cos\alpha\, f^3 \frac{\partial f}{\partial y}\right)\frac{\partial \overline{f}}{\partial y} d\Omega$$

$$+\int_{\Omega} \frac{\partial}{\partial y}\left(-Bo\cos\alpha\, f^3 \frac{\partial h}{\partial y}\,\overline{f}\right) d\Omega$$

$$-\int_{\Omega} \left(-Bo\cos\alpha\, f^3 \frac{\partial h}{\partial y}\right)\frac{\partial \overline{f}}{\partial y} d\Omega + \int_{\Omega} \frac{\partial}{\partial y}\left(f^3 \frac{\partial \mathrm{P}}{\partial y}\overline{f}\right) d\Omega$$

$$-\int_{\Omega} f^3 \frac{\partial \mathrm{P}}{\partial y}\frac{\partial \overline{f}}{\partial y} d\Omega + \int_{\Omega} \frac{\partial}{\partial x}\left(f^3 \frac{Bo}{\varepsilon}\sin\alpha\;\overline{f}\right) d\Omega$$

$$-\int_{\Omega} f^3 \frac{Bo}{\varepsilon} \sin\alpha \frac{\partial \overline{f}}{\partial x} d\Omega = 0 \qquad \text{(B.2)}$$

Unknown terms are modified to weaken the differentiability requirement using the fact that the test functions are chosen to be zero at any Dirichlet boundary condition ($|_{\Gamma} = 0$). Then, we end up with the weak formulation of equation (3.1) as below.

$$\int_{\Omega} \frac{\partial f}{\partial t} \overline{f}\, d\Omega + \int_{\Omega} \left(Bo \cos\alpha\, f^3 \frac{\partial f}{\partial x} \right) \frac{\partial \overline{f}}{\partial x} d\Omega$$

$$+ \int_{\Omega} \left(Bo \cos\alpha\, f^3 \frac{\partial h}{\partial x} \right) \frac{\partial \overline{f}}{\partial x} d\Omega - \int_{\Omega} f^3 \frac{\partial \mathrm{P}}{\partial x} \frac{\partial \overline{f}}{\partial x} d\Omega$$

$$+ \int_{\Omega} \left(Bo \cos\alpha\, f^3 \frac{\partial f}{\partial y} \right) \frac{\partial \overline{f}}{\partial y} d\Omega + \int_{\Omega} \left(Bo \cos\alpha\, f^3 \frac{\partial h}{\partial y} \right) \frac{\partial \overline{f}}{\partial y} d\Omega$$

$$- \int_{\Omega} f^3 \frac{\partial \mathrm{P}}{\partial y} \frac{\partial \overline{f}}{\partial y} d\Omega - \int_{\Omega} f^3 \frac{Bo}{\varepsilon} \sin\alpha \frac{\partial \overline{f}}{\partial x} d\Omega = 0 \qquad \text{(B.3)}$$

Curriculum Vitae

Name Surname : Mert Özdoğan

Education:

09/2013–06/2019	Izmir Katip Celebi University, Dept. of Mechanical Eng.
03/2016–08/2016	Jade University of Applied Science (Erasmus +)
07/2019–07/2022	Izmir Katip Celebi University, Graduate School of Natural and Applied Sciences, Dept. of Mechanical Eng.

Work Experience:

08/2016 – 09/2016	Petkim Petrochemical Company - Intern
07/2017 – 08/2017	Aero Wind Industry (ENERCON) - Intern

Publications:

1. Özdoğan M, Ceyhan U. On modeling Three-Dimensional Motion of Slender Droplets Over Substrates Using Finite Element Method with Adaptive Mesh Refinement. 6th International Students Science Congress 2022.
2. Ceyhan U, Özdoğan M, Tiktaş A. Pinning and depinning of Wenzel-state droplets around inclined steps. Colloid and Interface Science Communications 2020.